SUPERDARN PARAMETER ESTIMATION OPTIMIZATION AND
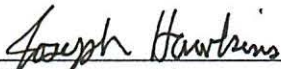
IMPLEMENTATION OF NEW TECHNIQUES

By

Ramin Jafari

RECOMMENDED:

Dr. Joseph Hawkins

Dr. Vikas Sonwalkar

Dr. Denise Thorsen

Dr. William Bristow, Advisory Committee Chair

Dr. Charles Mayer, Chair, Department of Electrical and
Computer Engineering

APPROVED:

Dr. Doug Goering
Dean, College of Engineering and Mines

Dr. John Eichelberger
Dean of the Graduate School

8/23/17

Date

SUPERDARN PARAMETER ESTIMATION OPTIMIZATION AND
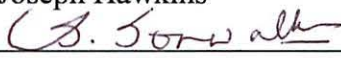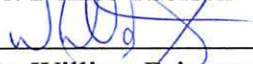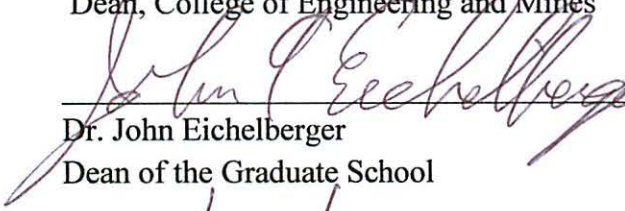
IMPLEMENTATION OF NEW TECHNIQUES

A

THESIS

Presented to the Faculty

of the University of Alaska Fairbanks

in Partial Fulfillment of the Requirements

for the Degree of

MASTER OF SCIENCE

By

Ramin Jafari, B.S.

Fairbanks, Alaska

August 2013

Abstract

The Super Dual Auroral Radar Network (SuperDARN) is an international radar network to study the ionosphere and upper atmosphere. The primary target of SuperDARN is field-aligned plasma irregularities in the E- and F-region of the ionosphere. To quantify the characteristics of these irregularities, the radar measures power, Doppler velocity, and spectral width from auto-correlation functions of the received samples. Since the target of interest is overspread, the derived parameters suffer from errors related to cross-range interference. In this thesis, we propose two scenarios to address this problem. First, we implement new approaches to avoid the cross-range interference, and second, we develop new optimization techniques that are more robust and less sensitive in dealing with this interference. New methods include filtering techniques, spectral analysis, and use of inverse techniques. The filtering methods (mismatched and adaptive) offer improvement in both suppressing the side lobes associated with pulse compression techniques and optimal estimation of the main lobe signal-to-noise ratio. Spectral analysis, extracts multiple Doppler velocities in the range while the current time-domain analysis is only capable of measuring one. Instead of dealing with ambiguities, inverse theory applied to SuperDARN received samples can potentially remove the associated cross-range interference, which results in more detailed and accurate information in obtaining the structure and dynamics of the irregularities. More accurate and detailed empirical models resulting from new optimization methods give more information that can be mapped over the current in-progress theoretical models, which finally results in better understanding the physics of the ionosphere.

Table of Contents

viii

List of Figures

xviii

List of Tables

Acknowledgements

To My Family:

Mom

Dad

Roozbeh

Ramak

Ramin

Chapter 1   Introduction

1.1 Motivation and Organization

The Super Dual Auroral Radar Network (SuperDARN) is one of the tools among ionosondes, GPS satellites, sounding rockets and incoherent-scatter radars used to study the upper atmosphere and the ionosphere. SuperDARN calculates complex auto-correlation functions from received signals scattered off the field-aligned plasma irregularities. The auto-correlation function (ACF) lag profile is used to derive power, Doppler velocity, and spectral width, which can be used to characterize the ionospheric plasma. However, the ACF measurements suffer from ambiguities and missing information due to the nature of the target, the transmitted pulse sequence, and the signal-processing algorithm on the receiver side. In this thesis, the main objective is to evaluate new techniques to optimize the current algorithm and improve the overall performance of the radar and measurements in terms of accuracy, details, and reliability.

The thesis is organized as follows: The first chapter gives a brief history of the radars. Radar principles, the ionosphere, and the types of the radars to study the upper atmosphere are presented, and SuperDARN is introduced. After a brief description of SuperDARN including the location of the radars, specifications and target of interest, the research objectives of the network are listed. The theory to calculate the complex auto-correlation function from received raw voltage samples is described and the related ambiguities that lead to missing and bad information are discussed.

Following the introductory sections, the second chapter is dedicated to the FitACF algorithm; the algorithm that converts raw ACFs to the fitted ACFs to obtain the fitted power, Doppler velocity and spectral width. Each step toward evaluating the final parameters is followed by an example that provides step-by-step guidance toward better

2

understanding of the algorithm. The topics discussed in chapters one and two provide the necessary information and background for the next chapters. Chapters three to five include new techniques to address the ambiguities and optimize the current algorithm. The third chapter discusses pulse compression techniques, including different types of pulse compression method on the transmit side and the new techniques that can be applied on the receiver side to deal with ambiguities the received pulse sequence carries with itself. The standard matched filtering, new approaches (mismatched and adaptive filtering) are studied, and their performance is evaluated.

The fourth chapter discusses the spectral analysis. The current algorithm (FitACF) employs time domain analysis to derive the parameters. Frequency domain analysis (Lomb Periodogram) described in this chapter is another approach to calculate the same parameters. Simulated case studies and experimental data using both approaches to measure Doppler velocity are compared and the existing trade-offs are studied.

Chapter five presents the use of inverse techniques to remove ambiguities associated with the characteristics of the target and correlation time of the transmitted pulse sequence. The forward problem, inverse method, illposedness and the related regularization techniques are explained. Furthermore, use of inverse techniques to remove range ambiguities for two different cases is discussed. Finally, conclusions, suggestions, and future work are presented in chapter six.

1.2 Brief History of the RADAR

RADAR is an acronym for RAdio Detection And Ranging. By the simplest definition, radar is a device consisting of a transceiver that generates and receives electromagnetic waves to detect objects. Although the radar principles are analogous to those used by flying bats, which generate and detect ultrasonic waves to find insects and avoid obstacles, it was not until 1886 when Heinrich Hertz began his experiments on the electromagnetic theory as formulated by Maxwell that the idea of radar came into being.

Hertz conducted his research by measuring velocity and length of the electromagnetic waves produced in the lab. In addition, he demonstrated that different materials reflect and refract electromagnetic waves. Later, other experiments were conducted, but the flagship of the time was Marconi's demonstration of trans-Atlantic communication. Here is part of the speech he delivered before the Institute of Radio Engineers [1]:

> As was first shown by Hertz, electric waves can be completely reflected by conducting bodies. In some of my tests, I have noticed the effects of reflection and detection of these waves by metallic objects miles away. It seems to me that it should be possible to design apparatus by means of which a ship could radiate or project a divergent beam of these rays in any desired direction, which rays, if coming across a metallic object, such as another steamer or ship, would be reflected back to a receiver screened from the local transmitter on the sending ship, and thereby, immediately reveal the presence and bearing of the other ship in fog or thick weather.

Although radars have a broad variety of civilian, scientific, and military applications in air-traffic control, tracking, surveillance, remote sensing, safety and navigation, it was not until World War II that the increased need for military dominance provided the motivation for radar development. Britain, the United States, Germany, Japan and France made contributions to the development of radars at this stage. After World War II, the pace of radar development slowed. Since that time, emergence of new technologies, rapid developments of electronics and advances in computing have made radars more sophisticated. High power amplifiers, improved receiver sensitivity, hardware developments, and use of Microwave as an operating band made the post-World War radars far more advanced than their predecessors. In the 21 century, the miniaturization and improved performance of RF devices along with new methods of signal processing and real-time computing using FPGAs (Field Programmable Gate Arrays) have made radars more accurate and functional, power efficient, reduced cost and

4

weight, which made the multi-billion dollar industry more advanced and commercially competitive.

Radar is a technique for detecting remote objects by transmitting electromagnetic energy and identifying target's characteristics based on the echoes returned. For example, the distance between the radar and a target determines the time it takes the electromagnetic wave to travel to the target and return to the radar. The angular location of a target determines the azimuth from which the echoes are received. The velocity of a target (moving targets) determines the Doppler shifted frequency of the received signal. A variety of parameters can be measured by radar depending on the application and the nature of the target, but the most important ones are range, velocity and received power.

1.2.1 Received Power

One of the basic signal parameters, the received power, is determined by Equation (1.1), which is known as the radar equation:

$$P_r = \frac{P_t G_t \sigma A_e}{(4\pi R^2)^2}. \qquad (1.1)$$

In this equation the radiated power (P_t) from the transmitter and the antenna with gain (G_t) will be reflected from the target with cross section (σ). The received power (P_r) from the target depends on the effective area (A_e) of the receiver antenna. The denominator represents the path loss of the transmitted power during the travel from the radar to the target and returning to the receiver.

1.2.2 Range

Range (R) can be determined by measuring the time (Δt) it takes for the radar signal with speed of light (c) to propagate to the target and back. Range is given is equation (1.2):

$$R = \frac{c\Delta t}{2}. \tag{1.2}$$

1.2.3 Doppler Shift

For a moving target with a velocity, v_r, the scattered signal collected by the receiving antenna will have a frequency shift, f_d, compared to the transmitted frequency, f_t. The shift in frequency resulting from the velocity of the moving target is known as Doppler shift. The target moving toward the radar results in a positive shift in transmitted frequency while the negative shift suggests the target is moving away from the radar. The velocity of the target is given in (1.3):

$$v_r = \frac{c \cdot f_d}{2 f_t}. \tag{1.3}$$

1.3 Ionosphere

Among other experiments, the first trans-Atlantic communication received by Guglielmo Marconi in 1901 provided clear evidence that in the upper atmosphere there is a region (subsequently called the ionosphere) where the gases are lightly ionized, thus providing a reflecting layer for an electromagnetic wave at the appropriate frequency [2]. The refractive index, n, of a medium of electron density, N, for a transmitted radio frequency, f, is approximately given by [2]:

$$n = (1 - \frac{e^2 N}{4\pi^2 \epsilon_0 m_e f^2})^{\frac{1}{2}}, \tag{1.4}$$

where e and m_e are the electron charge and the rest mass respectively, ϵ_0 denotes permittivity of free space. Substantial reflection of the signal may be expected as n approaches zero. The HF signal travels upward until it reaches an altitude where it equals the plasma frequency [2]:

$$N = 0.0124 \cdot f_p^{-2}, \tag{1.5}$$

then is reflected. In equation (1.5), f_p is referred to as plasma frequency. If the peak plasma frequency of the ionosphere is less than the signal frequency, the signal passes through without reflection, thus the plasma frequency at the peak of an ionized region is also referred to as the critical penetration frequency. The ionosphere is divided into a number of layers or regions: the D region (below 90 km); the E region (90-160 km); and the F region (above 160 km) which are shown Figure 1.1.
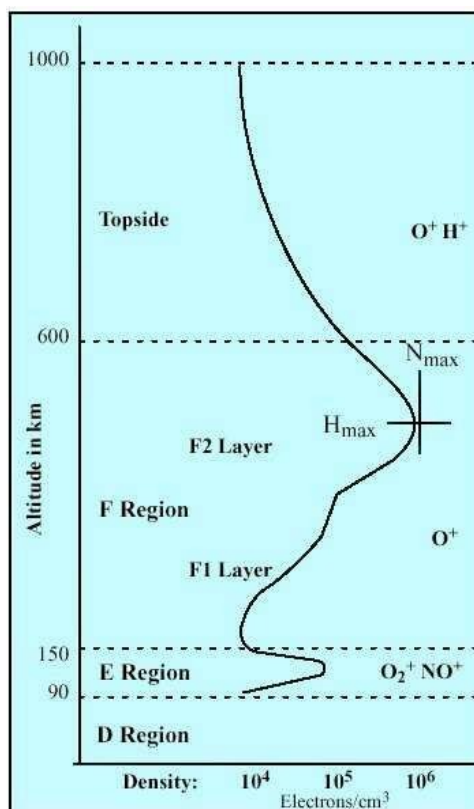
Figure 1.1: Ionospheric layers [NOAA/SEC].

There are a variety of tools to study the ionosphere such as, ionosondes, radars, GPS signals, and rockets, etc. In sections 1.4 and 1.5 coherent and incoherent-scatter radars, as the most important instruments to study the ionosphere are presented.

1.4 Incoherent-Scatter radar

In incoherent-scatter methodology, the scattered signal from a very large number of electrons and ions in random thermal motion in the ionosphere, will be composed of a frequency spectrum near the transmitted frequency resulting from the Doppler effect. If the complete spectrum of the scattered signal is measured with adequate signal-to-noise ratio, it is possible to determine parameters such as, electron density, electron temperature, ion temperature, ion mass, plasma drift velocity, ion-neutral collision frequency, electric currents and part of the spectrum of suprathermal electrons [3]. The received signal power is determined by the product of the number of electrons within the scattering volume and the scattering cross section of an individual electron. Large antennas, high-power transmitters, and low-noise receivers are essentials for these radars to achieve the signal-to-noise ratio for a target with a very small individual size (cross section of 10^{-28} m^2 for an electron) which is hundreds of kilometers away from the radar. There are a number of incoherent scatter radars to study the upper atmosphere (see Table 1.1).

Table 1.1: List of incoherent-scatter radars.

Radar Station	Radar Location	Operated
Jicamarca	Peru	Cornell University
Arecibo	Puerto Rico	SRI International
Millstone Hill	USA	Massachusetts Institute of Technology
Sondrestrom	Greenland	SRI International
Kharkov	Ukraine	Institute of the Ionosphere
Irkutsk	Russia	Institute of Solar-Terrestrial Physics
MU	Japan	Kyoto University
EISCAT- Tromso	Norway	The EISCAT Associates
EISCAT- Kiruna	Sweden	The EISCAT Associates
EISCAT- Svalbard	Svalbard	The EISCAT Associates
RISR	CANDA	SRI International
PFISR	USA	SRI International

1.5 Coherent-Scatter radar

Nonthermal fluctuations of the plasma lead to irregularities with some spatial and temporal coherence, which can produce a much larger scattering cross section than incoherent fluctuations. These irregularities, aligned with the Earth's magnetic field, result in a much larger scattering cross section perpendicular to the field than for any other direction. Scatter from these irregularities has some temporal coherence, which allows the use of coherent integration by radars observing the backscatter. Radars used to study these phenomena are called coherent-scatter radars [3]. The first extensive use of coherent-scatter radars to study the ionospheric convection at polar latitudes took place in the 1970s and 1980s with the development of the Scandinavian Twin Auroral Radar Experiment [4].

SuperDARN as a coherent-scatter radar measures power, spectral width and the drift velocity of the ionospheric irregularities. The velocity measurement of different radars of the network are combined and mapped over empirical models to produce convection maps. These maps show the movement of the bulk irregularities in the E- and F-region of the plasma.

1.6 SuperDARN Overview

SuperDARN is an international collaboration of about a dozen of countries with more than 30 radars in operation. The first radar was built in 1983 in Goose Bay, Labrador. A schematic of the first SuperDARN radar hardware is shown in Figure 1.2.
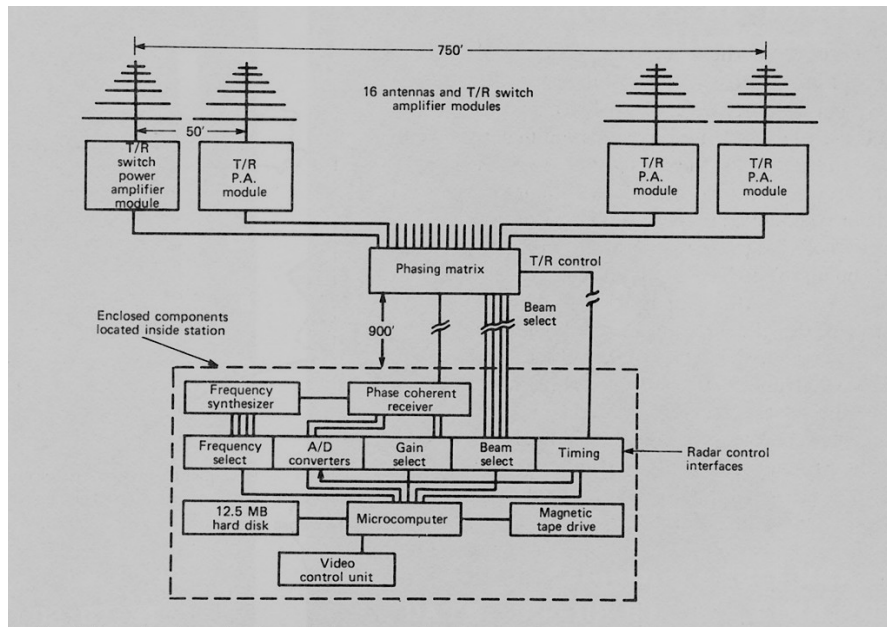
Figure 1.2: Hardware schematic of Goose Bay radar 1983. [Ray Greenwald]

SuperDARN uses pulsed-Doppler radars, each consisting of a main array and a secondary array operating in the HF (8-20 MHz) band. In the main array, there are 16 log-periodic antennas while the secondary array consists of 4 antennas. Each of the 16 main-array antennas is connected to a 600 W peak-power transmitter, which produces a combined total transmit power of 9600 W. The radar transmits up to 16 beam directions, measuring the parameters as a function of range along each beam. Figure 1.3 illustrates the geographic fan plot of McMurdo radar with 16 beams. The locations of the SuperDARN radars are shown in Table 1.2.
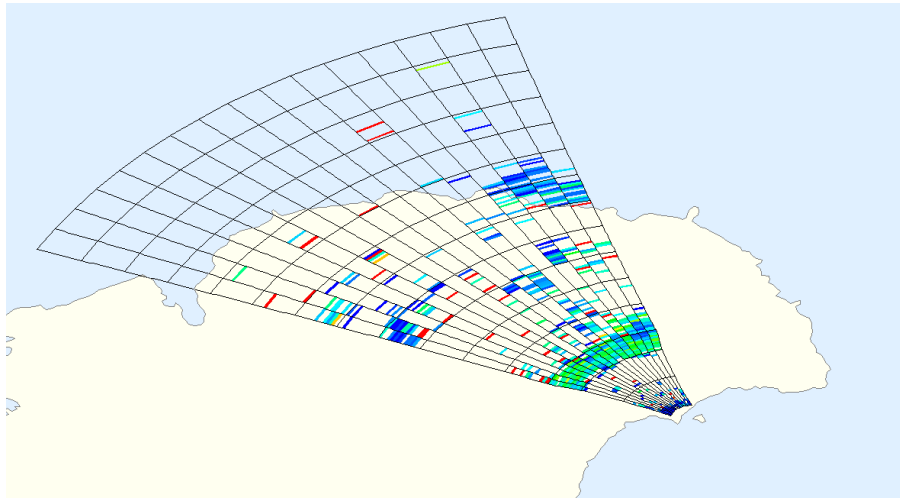
Figure 1.3: Geographic fan plot of the spectral width for McMurdo radar.

Table 1.2: List of SuperDARN radars in northern and southern hemispheres.

	Radar Station	Radar Location	Operated
Northern Hemisphere	Goose Bay	Canada	Johns Hopkins University Applied Physics Laboratory
	Kapuskasing	Canada	Johns Hopkins University Applied Physics Laboratory
	Saskatoon	Canada	University of Saskatchewan
	Prince George	Canada	University of Saskatchewan
	Kodiak	USA	University of Alaska Fairbanks
	Pykkvybaer	Iceland	University of Leicester
	Hankasalmi	Finland	University of Leicester
	King Salmon	USA	National Institute of Information and Communications Technology
	Wallops Island	USA	Johns Hopkins University Applied Physics Laboratory
	BlackStone	USA	Virginia Polytechnic Institute and State University
	Hokkaido	Japan	Nagoya University
	Inuvik	Canada	University of Saskatchewan
	Rankin Inlet	Canada	University of Saskatchewan
	Fort Hayes West	USA	Virginia Polytechnic Institute and State University
	Fort Hayes East	USA	Virginia Polytechnic Institute and State University
	Adak Island	USA	University of Alaska Fairbanks
Southern Hemisphere	South Pole	South Pole	University of Alaska Fairbanks
	Sanae	Antarctica	University of KwaZulu-Natal
	Syowa South	Antarctica	National Institute of Polar Research
	Syowa East	Antarctica	National Institute of Polar Research
	Tiger	Tasmania	La Trobe University
	Unwin	New Zealand	La Trobe University
	Falkland Islands	Falkland Islands	University of Leicester
	McMurdo	Iceland	University of Alaska Fairbanks

In Figure 1.4 radar field of view in the northern and souther hemisphere are illustratred. These fields of view overlap, therby providing the capability to combine the meausred line-of-sight velocities in the overlapped regions to produce vector velocities.
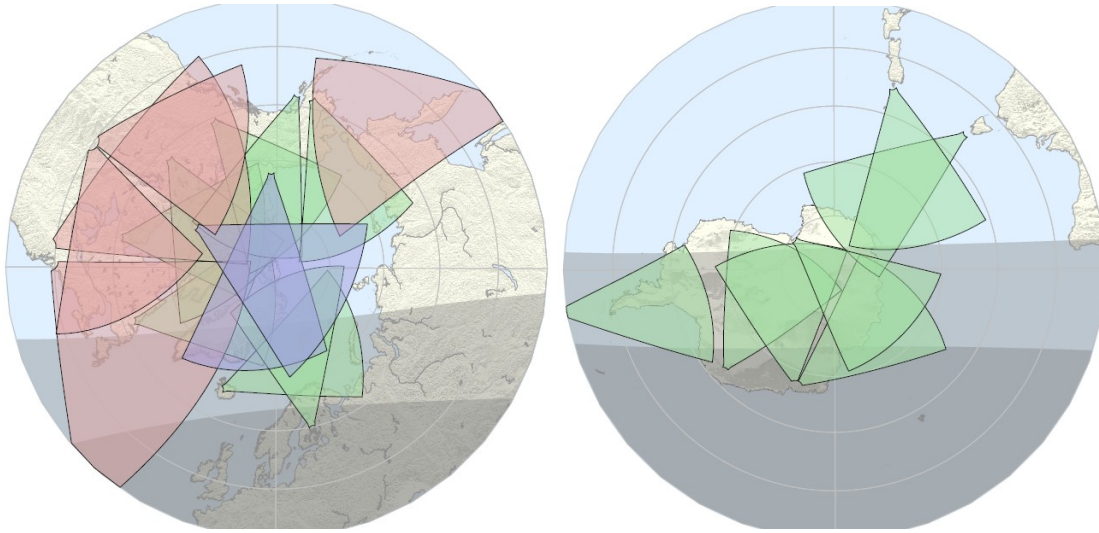
Figure 1.4: SuperDARN radars field of view in the northern (top) and the southern hemisphere (bottom). [Johns Hopkins Applied Physics Laboratory, 2010].

Mapping multiple vector velocities allows creation of plots like the one in Figure 1.5 that shows the movement of plasma in F region of ionosphere. The origin of a plasma irregularities detected by SuperDARN radars is depicted by the dots and the tails point is in the direction that the bulk velocity is moving [5].
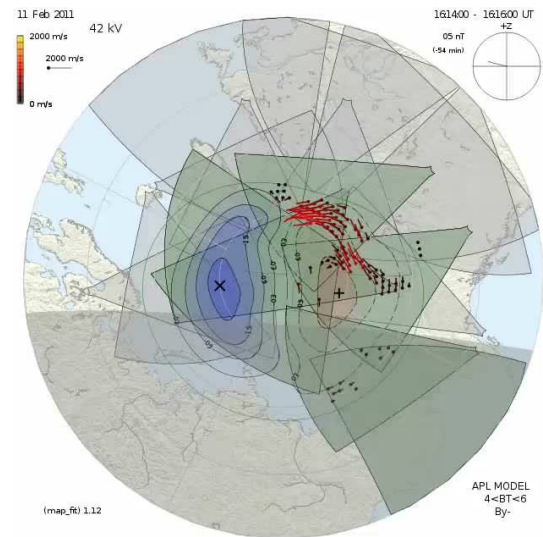
Figure 1.5: SuperDARN ionospheric plasma convection map [Johns Hopkins Applied Physics Laboratory 2010]. This map is constructed from mapping multiple vector velocities showing the bulk movement of the plasma.

SuperDARN has application in multiple areas such as, magnetosphere/ionosphere coupling, ionosphere/atmosphere coupling, plasma processes in the ionosphere and radio wave propagation. The main research objectives are listed below [6]:

- Structure of global convection-to provide a global-scale view of the configuration of plasma convection in the high-latitude ionosphere.

- Dynamics of global convection-to provide a global-scale view of the dynamics of plasma convection in the high-latitude ionosphere. (Previous studies of high-latitude convection had largely been statistical and time-averaged).

- MHD waves-to measure the energy influx from MHD waves on a larger spatial scale than previously possible.

- Substorms-to test various theories of polar cap expansion and contraction under changing IMF conditions and observe the large-scale response of the nightside convection pattern to substorms.

- Gravity waves-high-latitude plasma structures and ionospheric irregularities.

- Meteor echoes-to study neutral winds.

1.7 SuperDARN Pulse Sequence and Auto-correlation Function

The radar transmits a multi-pulse sequence [7] of unequally spaced pulses. Use of multi-pulse sequences (typically eight pulses) allows for discrimination of returns from different pulses at different ranges. The radar pulse sequence and the corresponding lags are shown in Figure 1.6.
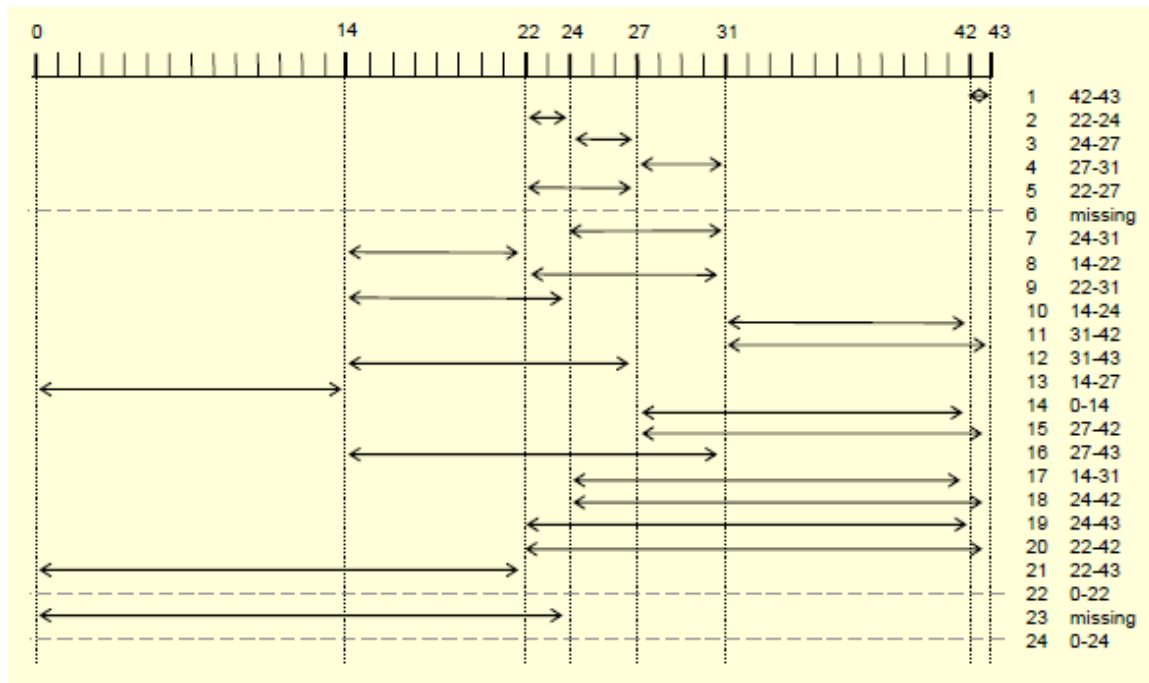
Figure 1.6: The SuperDARN pulse sequence with 8 pulses. The spacing between pulses are multiples of a fundamental lag, allowing calculation of 22 lags. The current pulse sequence has two missing lags at 6τ and 24τ.

After the transmission of each pulse, the received signal from ionospheric irregularities is down converted to baseband frequency in the receiver and sampled at a sampling rate equal to pulse length. The Auto-Correlation Function (ACF) of the signal is

calculated from these recorded samples and is used to calculate power, Doppler velocity and spectral width for each range gate. Figure 1.7 shows the pulses within the pulse sequence and the corresponding samples.
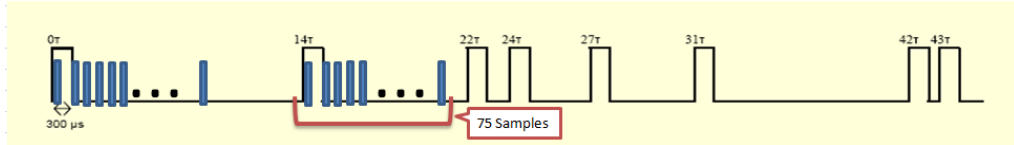
Figure 1.7: The SuperDARN pulse sequence with 75 samples illustrated in blue for each pulse.

Calculation of the ACF for each lag in each range is given in equations (1.6) to (1.12). The transmitted signal is represented as:

$$T(t) = A \sin(wt + \Phi_0), \qquad (1.6)$$

where A corresponds to the envelope of the transmitted waveform (pulse), w the carrier frequency, Φ_0 a constant phase angle and t represents time. The corresponding received signal is given by:

$$R(t) = B \sin\big((w + w_d)t + \Phi_1\big), \qquad (1.7)$$

where B denotes envelope of the received signal, w_d the Doppler shift resulting from a moving target and Φ_1 a random phase.

The received signal is digitized at the HF and numerically down converted to obtain the baseband signal. This is accomplished by multiplying the sampled received signal by the sine (in-phase) and cosine (quadrature) of the carrier frequency. The following equation shows derivation of the in-phase part of the received signal:

$$R_i(t) = B \sin\big((w + w_d)t + \Phi_1\big) \cdot \sin(wt),$$

$$R_i(t) = \frac{1}{2}B\cos\big((w + w_d - w)t + \Phi_1\big) - \frac{1}{2}B\cos\big((w + w_d + w)t + \Phi_1\big).$$

The second term of the previous equation is removed by passing the signal through a low pass filter. The output of the filter is the in-phase part of the signal, which is given in equation (1.8):

$$R_i(t) = \frac{1}{2}B\cos(w_d t + \Phi_1). \tag{1.8}$$

The quadrature component of the received signal is determined in a similar manner. Thereby, the total complex received signal equals:

$$R(t) = R_i(t) + iR_q(t) = \frac{1}{2}B\cos(w_d t + \Phi_1) + i\frac{1}{2}B\sin(w_d t + \Phi_1) = \frac{1}{2}Be^{i(w_d t + \Phi_1)}. \tag{1.9}$$

The autocorrelation function is defined as:

$$ACF(\tau) = <R(t)\overline{R(t + \tau)}>, \tag{1.10}$$

where τ is the lag time, overbar corresponds to complex conjugate of the signal, and $<>$ denotes the ensemble average. Hence:

$$ACF(\tau) = \int_{-\infty}^{\infty} R(t)\overline{R(t + \tau)}\,dt. \tag{1.11}$$

The temporal resolution often used by SuperDARN for each beam scan is about 3 seconds. In each scan, around 25 pulse sequences are transmitted and an average of 25 ACFs corresponding to the number of pulse sequences are calculated. The total scan time is one minute for 16 beams in normal mode of operation. The autocorrelation function of the received signal (equation (1.9)) is obtained in equation (1.12), where r denotes range bin and τ represents lag:

$$ACF(r, \tau) = B(r)e^{i(w_d(r)t + \Phi_1(r))} \cdot B(r)e^{-i(w_d(r)t + w_d(r)\tau + \Phi_1(r))} =$$

$$B(r) \cdot B(r)e^{-i(w_d(r)\tau)}. \tag{1.12}$$

17

The resulting ACFs are saved on the radar hardware and used by the radar-processing unit to derive power, Doppler velocity, and spectral width. The number of lags in the ACF profile depends on the number of pulses in the pulse sequence. Lag resolution depends on the fundamental spacing, i.e. the spacing between the two pulses in the sequence that determine lag one. For instance, for each range in Figure 1.6 up to 24 lags with lag spacing of 1500 μs can be calculated.

1.8 Bad Lags

There are times in each pulse sequence that the receiver samples the signal even though the radar is transmitting a pulse. The samples and the corresponding lags that fall in this category are marked as bad lag resulting from receiving while the transmitter is ON (TX-RX Overlap). Figure 1.8 shows the transmitter and the receiver overlap time.
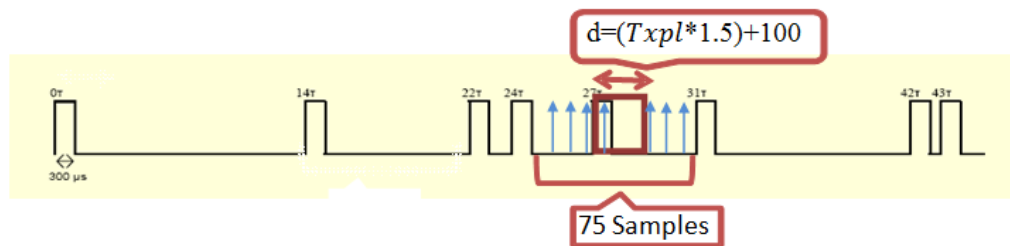
Figure 1.8: Bad lags resulting from transmit and receive signal overlap. Samples received within time window of d are marked as bad samples (Txpl: Pulse length) and the lags using these samples as bad lag consequently.

In addition, received echoes from a desired range coinciding with echoes received from other ranges, result in cross-range interference (CRI). In other words, simultaneous returns from different pulses and different ranges in the sequence results in CRI. These

bad samples and the corresponding lags are marked in the FitACF bad-lag determination algorithm (which is described in Chapter 2). Figure 1.9 shows how the received signals at different time intervals are contaminated with different ranges. The first plot from top shows three pulses to be transmitted and three ranges the pulses scatter off. The following plots in Figure 1.9 show scattered signal from ranges A, B and C for each pulse as if they were transmitted and received separately. Finally, the bottom plot shows the summation of these three plots, pulse returns add with each other and results in ambiguity known as CRI.
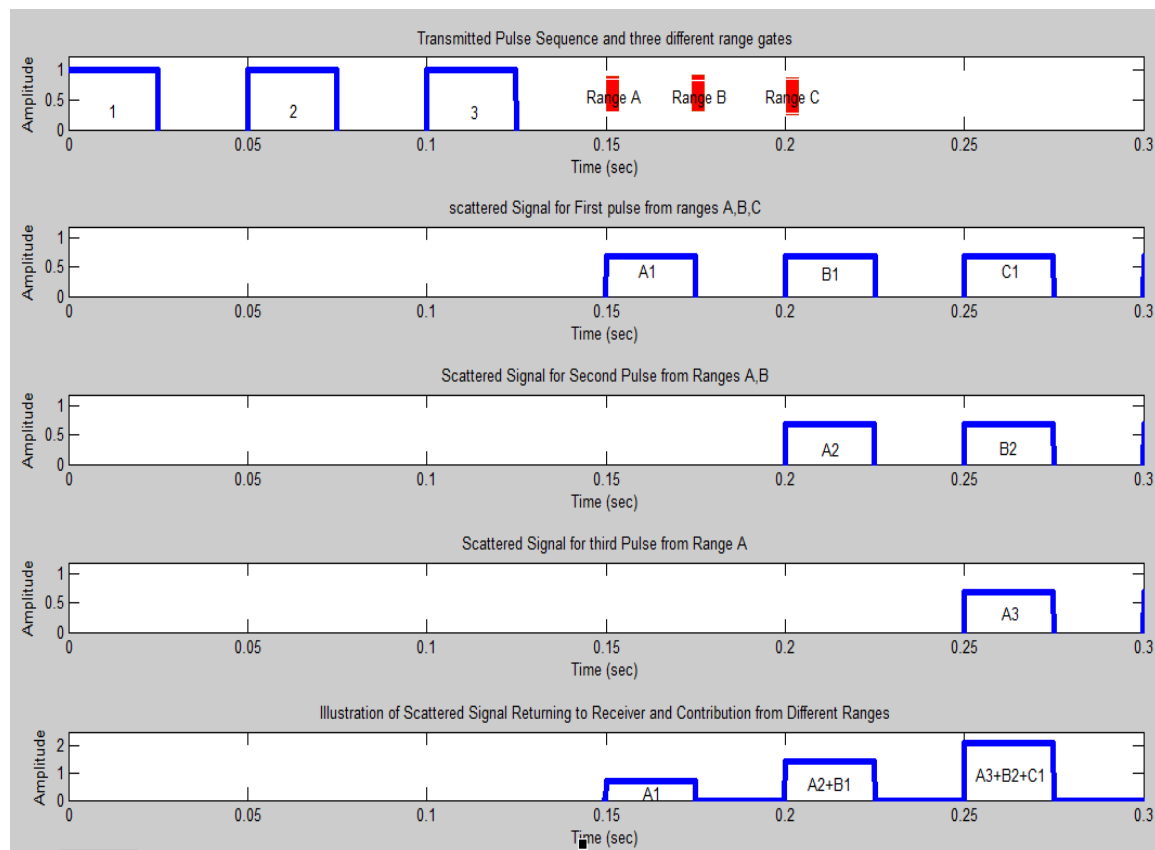
Figure 1.9: Illustration of cross-range interference. The first plot shows three pulses (1,2,3) and three range gates (A,B,C). The next three plots show as if these pulses were transmitted and received individually by the radar. In the bottom plot, summing three previous plots result in cross-range noise.

Chapter 2   FitACF Algorithm Analysis

The SuperDARN saves autocorrelation functions calculated from received in-phase and quadtature samples for further processing. This auto-correlation function is called a "raw ACF" and is used by the SuperDARN algorithm (FitACF) to calculate signal power, Doppler velocity, and spectral width. The FitACF algorithm consists of a number of subroutines. The raw ACFs are passed to these subroutines in the algorithm and final outputs are called the fitted ACF parameters. Major subroutines are shown in the flow chart in Figure 2.1. Each block of the flow chart describes what parameters are calculated in each step along with subroutines used for this purpose.

20
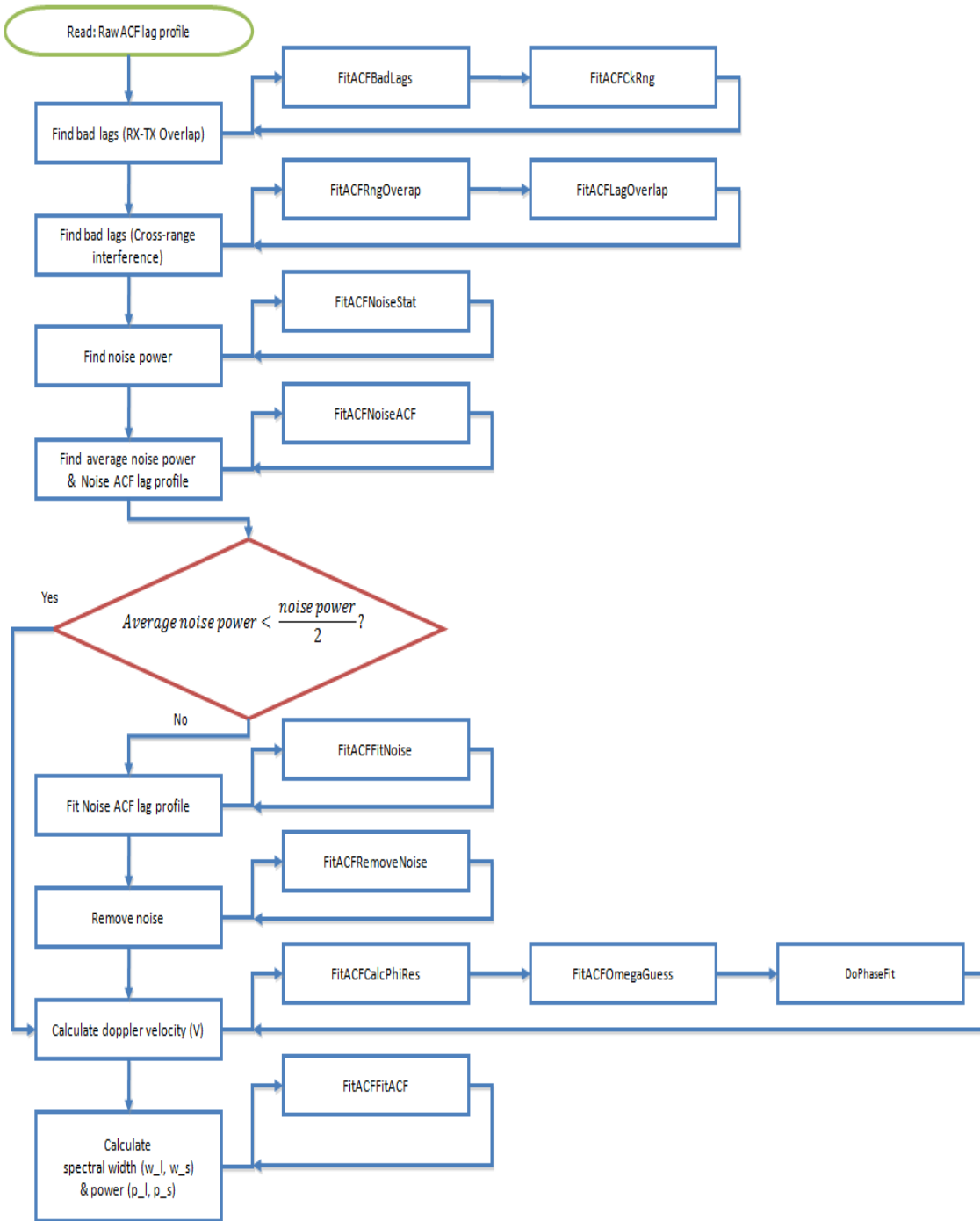
Figure 2.1: Flowchart of the FitACF algorithm, showing the main subroutines. These subroutines calculate power, Doppler velocity, and spectral width from ACF of the received.

The FitACF algorithm is explained by means of an example to provide a better understanding of the algorithm and subroutines. Particularly, the values and thresholds calculated for the example should be helpful. In this example, the radar (McMurdo) has 16 scan beams. Each beam is sampled into 75 range gates with 45 km range resolution, corresponding to 300 μs sampling time. This results in total range scan of 3555 km. The pulse spacing and the number of pulses within the pulse sequence determine the resolution and number of lags in the ACF lag profile, which are 1500 μs and 23 lags for this example.

2.1 TX-RX Overlap Bad Lag Calculation (FitACFBadlags and FitACFCkRng)

In flowchart in Figure 2.1, the first two subroutines in the main routine are FitACFBadlags and FitACFCkRng. These two subroutines calculate and mark bad samples resulting from TX-RX overlap. This is accomplished by finding the samples that fall inside the window of length d $(d = 1.5(pulse\ length) + 100)$. These samples are marked as bad samples and if any of them are used to calculate the ACF for a particular lag, the corresponding lag will be marked bad as well. Figure 2.2 shows that for range 12, beam 15, McMurdo radar, out of 23 calculated lags in the ACF lag profile, 5 of them are marked as bad lags.
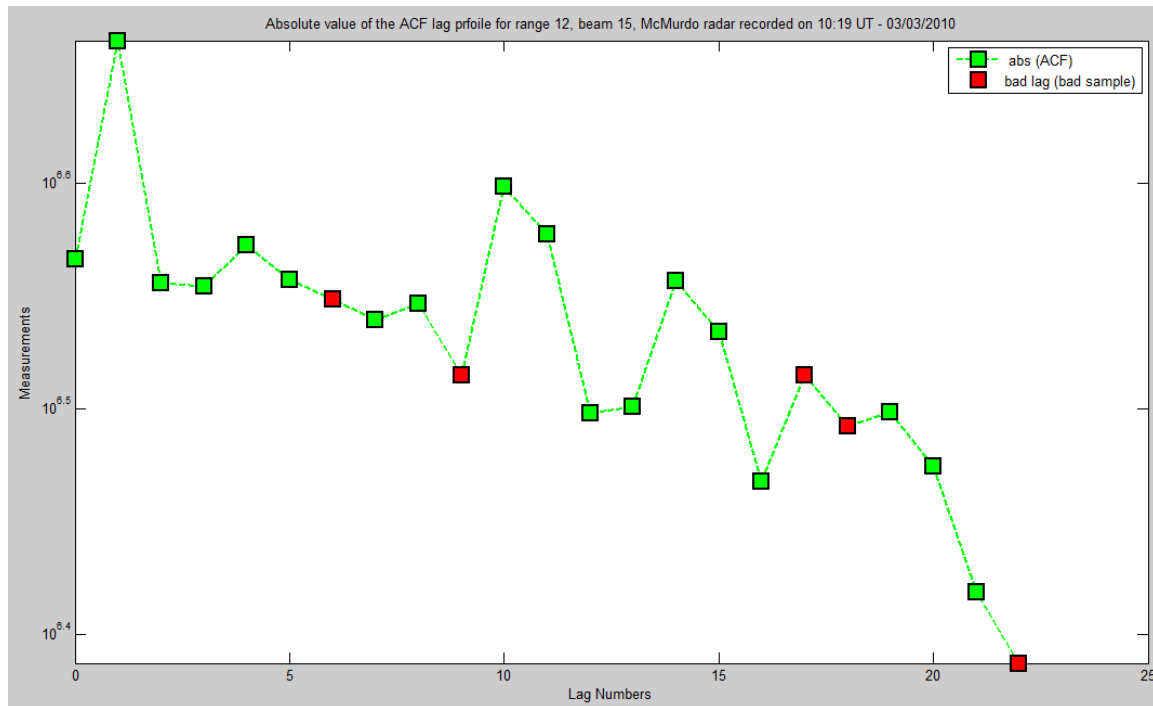
Figure 2.2: Bad lags resulting from overlapping received samples with transmitted pulses (TX-RX overlap) for range 12, beam 15, McMurdo radar.

2.2 Cross-range Interference Bad Lag Calculation (FitACFRngOverLap and FitACFLagOverLap)

FitACFRngOverLap and FitACFLagOverLap subroutines in the flowchart in Figure 2.1 analyze the lag profiles to determine bad lags resulting from cross-range interference. In Figure 2.4 all the samples (0:70) that correspond to the first transmitted pulse (0τ) are free from contamination by the other pulse returns. For subsequent pulses, the algorithm checks for interfering ranges from all the previous pulses in the sequence. This is done by comparing the received power of the corresponding pulse in the current range with the received power of 0τ in all the interfering ranges. If the received power of the contaminating range is significant compared to the power in the current range then the lag is marked as bad resulting from CRI. The threshold for power comparison in the code equals $0.3\ Nave$, where $Nave$ is the number of times the pulse sequence was transmitted in the beam. Figure 2.3 shows the flowchart of the procedure for finding CRI bad lags.
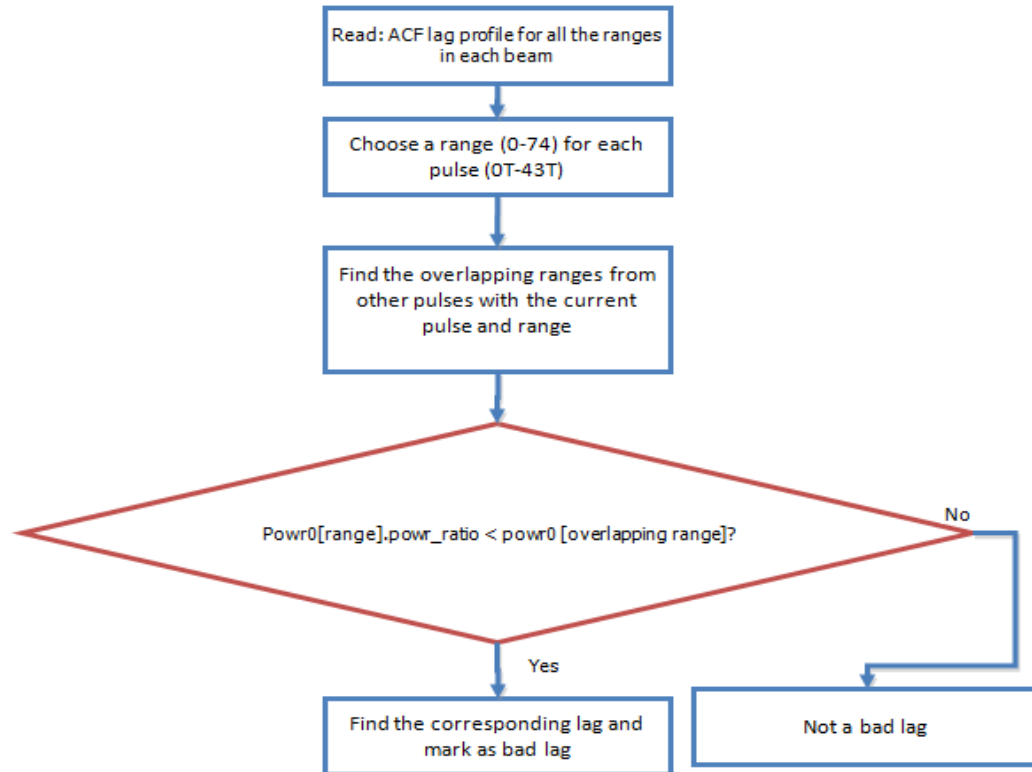
Figure 2.3: Flowchart of FitACFBadLags routine, showing bad lag determination procedure.

Figure 2.4 illustrates the potential ranges that can lead to a bad lag (75 samples are recorded for each transmitted pulse). There are eight plots that correspond to the number of pulses in the pulse sequence. Each plot shows where the sampling time begins for each pulse in terms of sample number. Where the sample numbers in the horizontal axis of each plot have the same value for different pulses is where the overlapping ranges occur. For the first pulse (0τ) up to sample 70, all the samples are free from cross-range interference, but for instance, sample number 150 can be a potential range for interference, because it is an overlapping range for pulses 22τ, 24τ and 27τ.
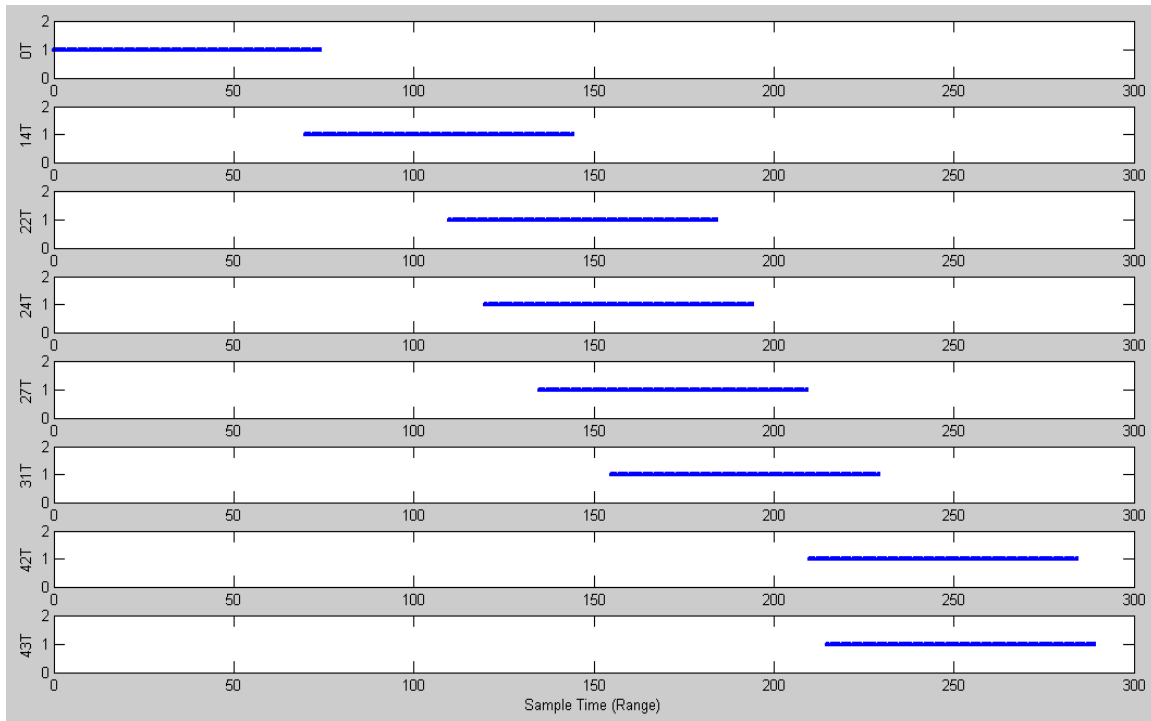
Figure 2.4: Potential interfering ranges for each pulse in the SuperDARN pulse sequence with eight pulses. The blue line in each plot shows the corresponding sample times received for each pulse within the pulse sequence. Any coincident sample numbers can be a potential cross-range interference range.

In Figure 2.5, there are 7 bad lags out of 23 total ACF lag profile, in which two of them are marked as bad lags resulting from cross-range interference.
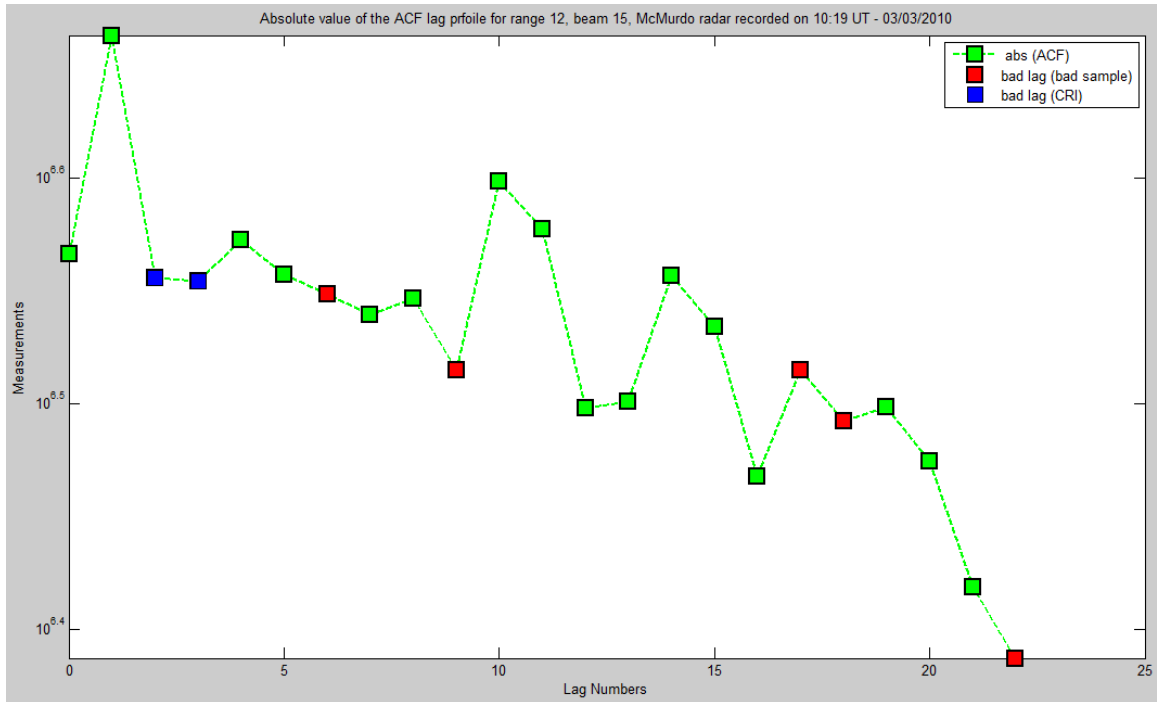
Figure 2.5: Bad lags resulting from overlapping received samples with the transmitted pulse (TX-RX overlap) and cross-range interference (CRI) for range 12, beam 15, McMurdo radar.

2.3 Noise Power Calculation (FitACFNoiseStat)

The next step in the FitACF algorithm main routine is minimum-power calculation. This is obtained by averaging the 10 lowest lag-zero powers in each beam and calling it *minpwr*. In the flowchart in Figure 2.8 if the real part of the lag zero is less than a defined threshold, the range is discarded from further processing. The threshold for this purpose is called *plim* (1.6 *minpwr*). Lag-zero power value for 75 range gates and *plim* are shown in Figure 2.6.
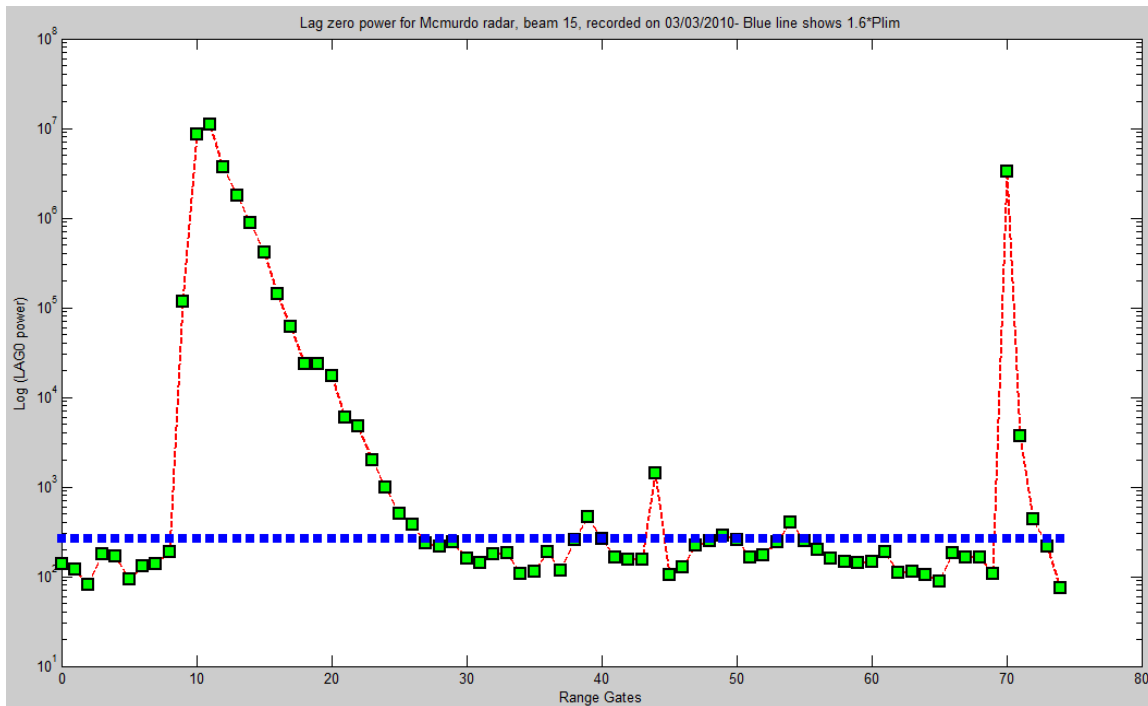
Figure 2.6: Illustration of the *plim* (blue) and lag-zero power (green) for 75 range gates in beam 15, McMurdo radar. In any range if the lag-zero power is below the threshold the lag profile in the range is discarded from further processing.

The flowchart (Figure 2.8) shows that each lag in the range should be between two thresholds: high limit ($lag\ zero\ power + fluct$) and low limit ($lag\ zero\ power - 2\ fluct$) to be considered for noise power estimation. The value of the *fluct* is determined by dividing the lag zero power by $Nave$.

For each range the code checks for real value of lag-zero power to determine if it is less than the *plim*. If so, it obtains the absolute value of the all the lags in that range, which are not a bad lags and between high and low limits. The selected lags are averaged over the lag profile for each range gate. Ultimately, all these averages are summed and averaged over the number of range gates in each beam to calculate the noise power.
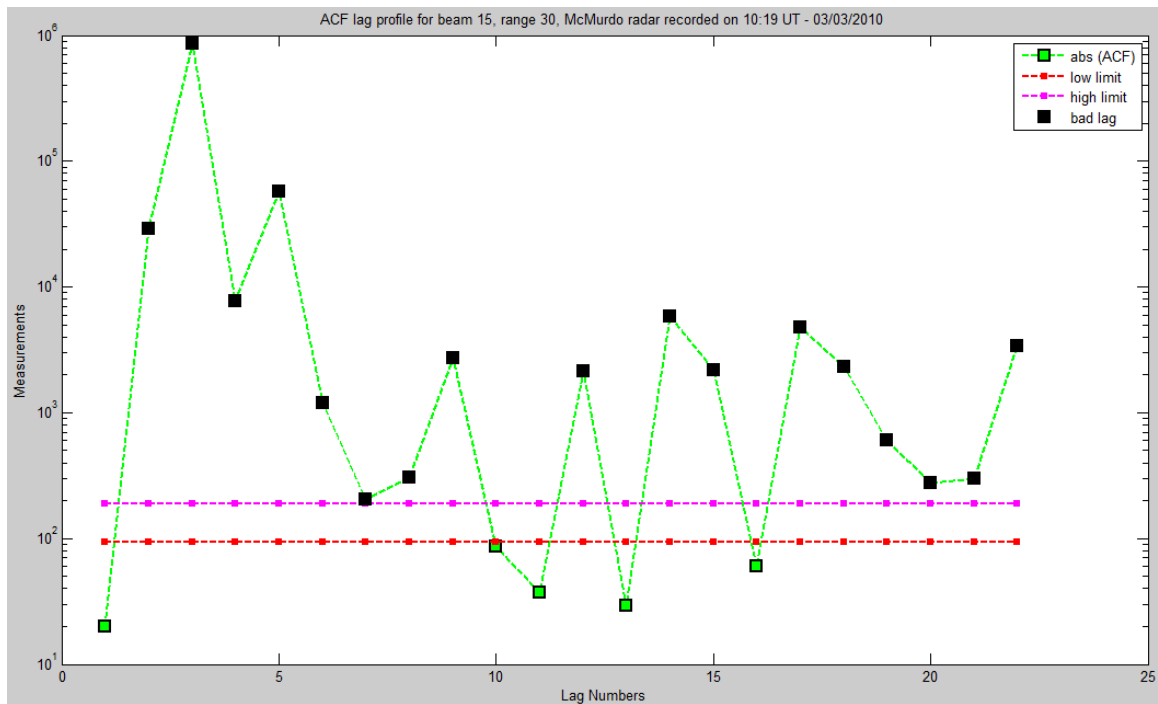
Figure 2.7: Illustration of the absolute value of ACF lag profile, bad lags, high and low limits for range 30, beam 15, McMurdo radar. Any good lags that falls between these two limits are passed to the next routine for noise power calculation.

Figure 2.7 shows that for range 30, beam 15, McMurdo radar, there are only 5 good lags in that range that can be taken into account for noise power calculation, but none of these lags are within high and low limits. Therefore, this range makes no contribution to noise power calculation.

28
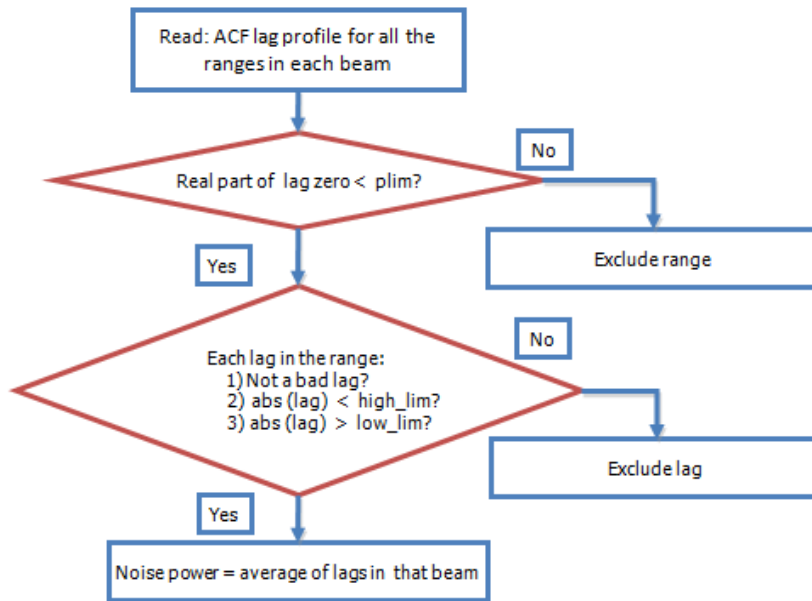
Figure 2.8: Flowchart of the FitACFNoiseStat routine, showing noise power calculation procedure.

2.4 Noise ACF Estimation (FitACFNoiseACF)

Next step in the FITACF algorithm is determination of the autocorrelation function for noise profile. The flow chart in Figure 2.8 shows how the noise ACF lag profile is calculated for each beam.
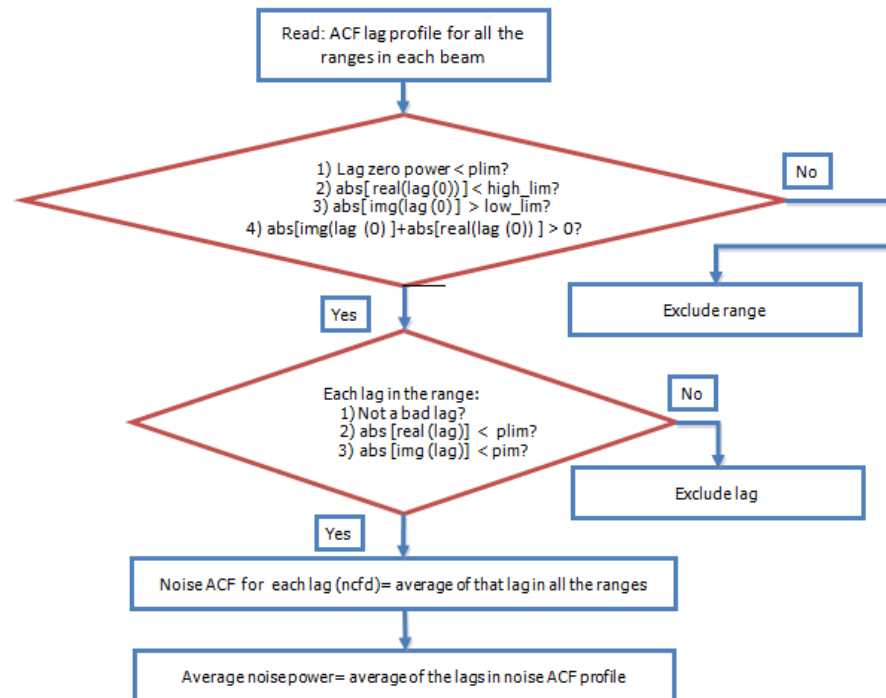
Figure 2.9: Flowchart for FitACFNoiseACF routine, showing noise ACF lag profile and average noise power calculation procedure.

In Figure 2.10, only lag numbers 0, 1, 10, 11, 13, 16 are not bad lags and less than the *plim*; hence, are passed to the next routine for further noise ACF calculations.
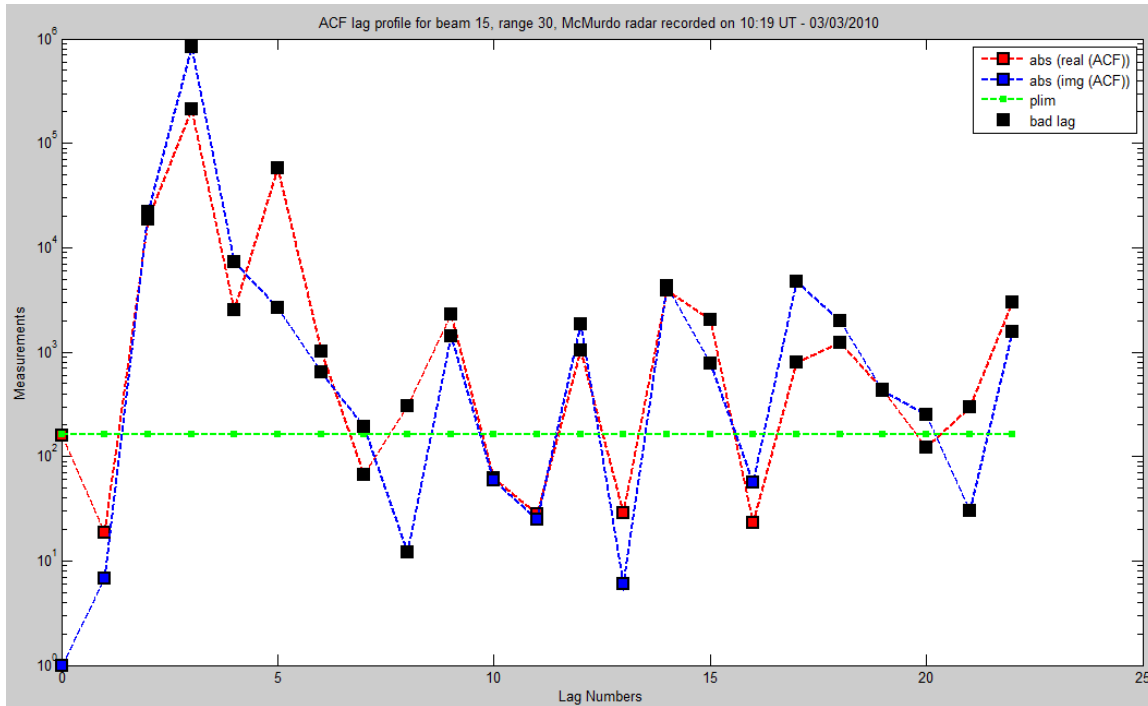
Figure 2.10: Illustration of the *plim* threshold and the absolute value of the real and imaginary parts of the ACF lag profile for range 30, beam 15, McMurdo radar. Any lags that is not bad and below the threshold, is passed to the next routine for noise ACF calculation.

Ultimately, the average of all values in the noise ACF lag profile is called the average noise power, which along with the noise power for 16 beams is illustrated in Figure 2.11. In the flowchart in Figure 2.1 after noise power, noise ACF lag profile, and average noise power calculations, the main routine compares these two values:

$$average\ noise\ power > \frac{noise\ power}{2} \tag{2.1}$$

If equation (2.1) is true, it means there is coherent noise to be removed. In this case, the noise ACF profile is passed to FitACFFitNoise routine for noise fitting process.
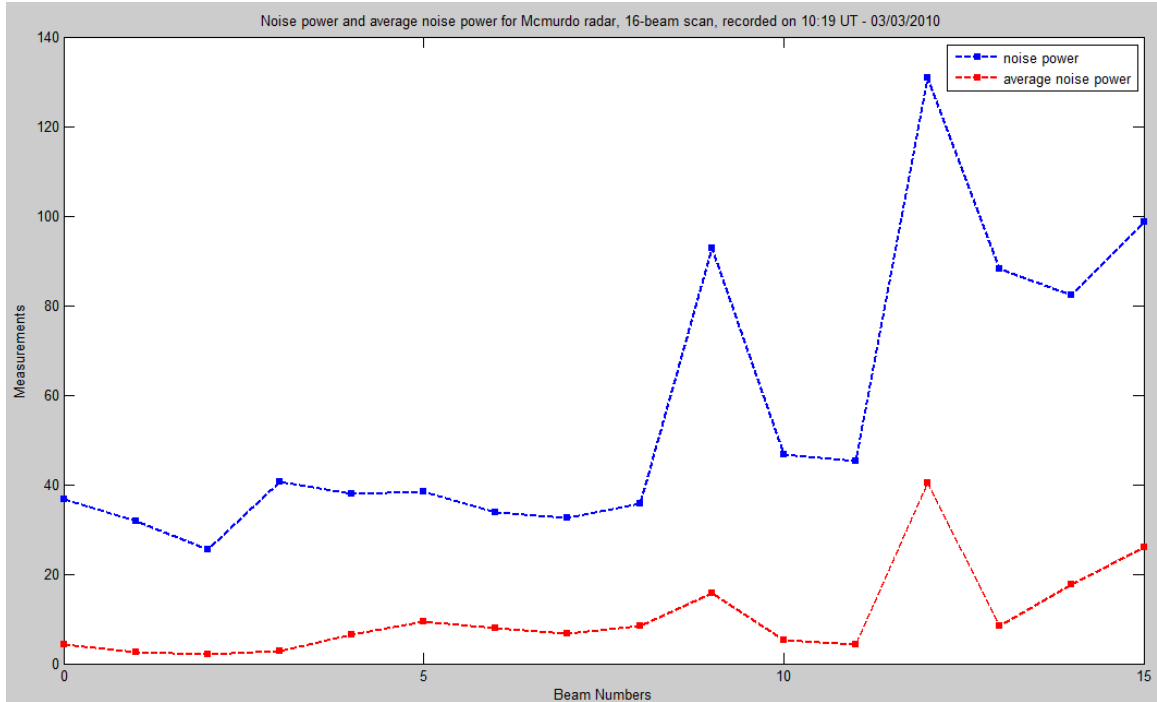
Figure 2.11: Illustration of the noise power and average noise power for 16 beams, McMurdo radar.

2.5 Noise ACF Fitting Process (FitACFFitNoise)

In this routine, the noise profile calculated in the FitACFNoiseACF routine is fitted using exponential (λ) and Gaussian (σ) non-linear fitting techniques by passing the noise ACF lag profile to the FitACFFitACF subroutine. After derivation of the key parameters for λ fit (p_λ, w_λ) and σ fit (p_σ, w_σ), where p corresponds to the fitted lag zero power and w the decaying factor, these values are used to obtain the real and imaginary parts of the fitted noise profile. Derivation of the complex autocorrelation function of the noise is shown in equations (2.2) and (2.3).

For lambda fit:

$$Noise\ ACF_\lambda(real, img) = [p_\lambda \mathrm{e}^{-w_\lambda t} \cdot \cos(vt), p_\lambda \mathrm{e}^{-w_\lambda t} \cdot \sin(vt)], \qquad (2.2)$$

and for Sigma fit:

$$Noise\ ACF_\sigma(real, img) = [p_\sigma e^{-(w_\sigma t)^2} \cdot \cos(vt), p_\sigma e^{-(w_\sigma t)^2} \cdot \sin(vt)], \qquad (2.3)$$

where v is the velocity in each range. Figure 2.12 shows the absolute value of the calculated noise ACF profile and the Gaussian and exponential fitted curves.
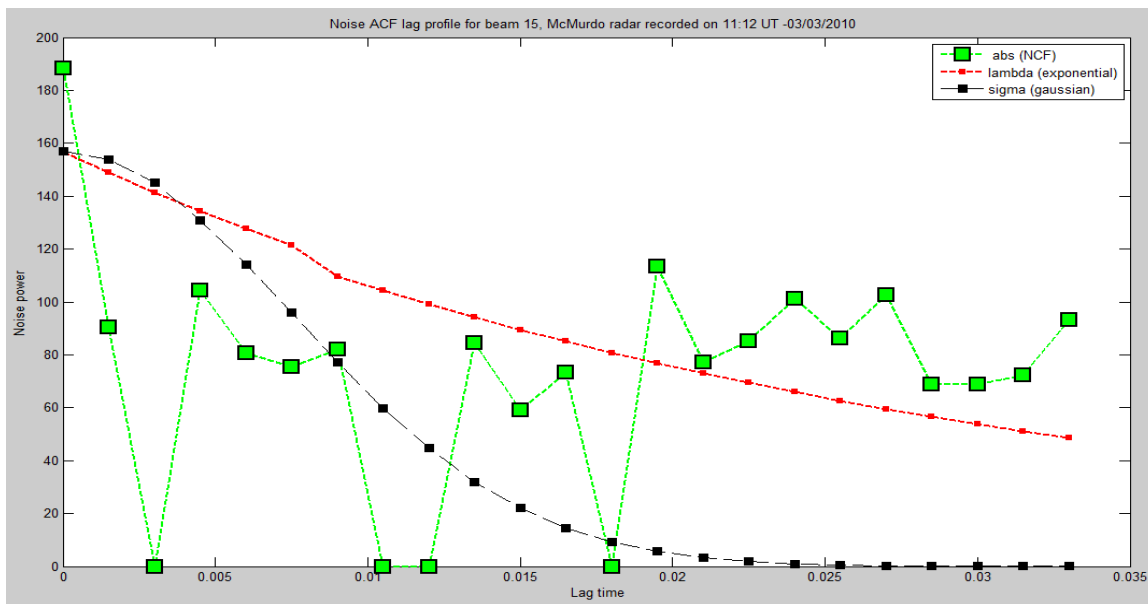
Figure 2.12: Illustration of the absolute value of the noise ACF lag profile and fitted curves using lambda and sigma fitting for beam 15, McMurdo radar.

The flow chart in Figure 2.13 explains the detailed noise ACF estimation and the fitting procedure.

```
Read: NCF lag profile
```

```
Fit noise profile (exponential)          Fit noise profile (gaussian)
```

```
Esitmate: w_l, w_l_error                 Esitmate: w_s, w_s_error
```

```
w_l_error < w_s_error?
```
No
Yes

```
Save NCF parameters for Gaussian
curve - Discard exponential
```

```
Save NCF parameters for exponential curve -
Discard gaussian
```

```
Calculate real and imaginary parts of NCF lag profile
```
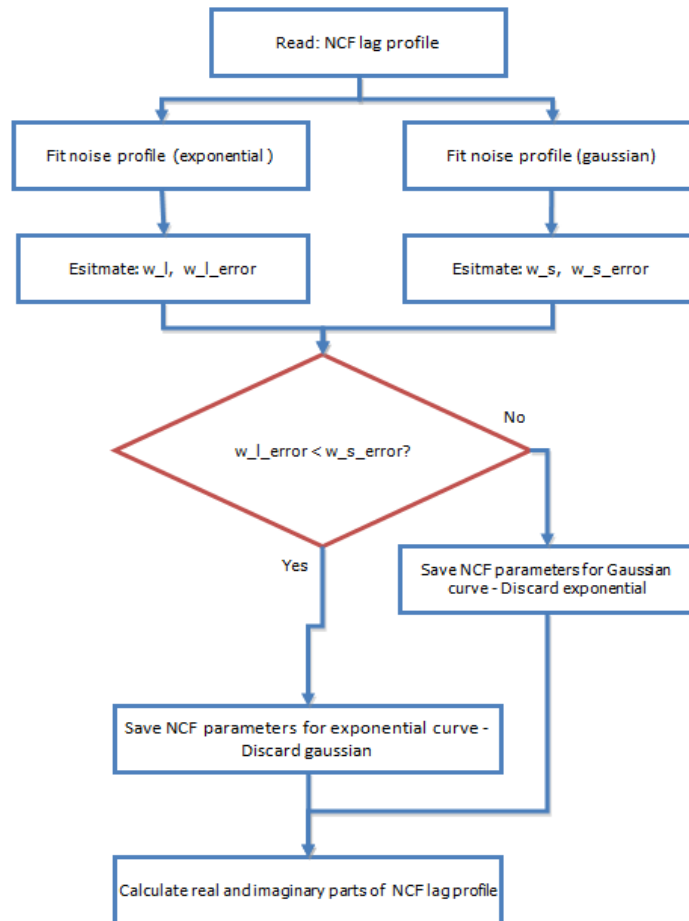
Figure 2.13: Flowchart of FitACFFitNoise routine, showing the procedure of fitting ACF of the noise profile.

2.6 Noise Removal (FitACFRemoveNoise)

The next step in the FitACF algorithm is removing noise from the lag profile. The code verifies if each range in the current beam is eligible for noise removal. This is done by comparing the lag zero power in each range with $plim,$ and if $pa > plim$ then the noise is removed from the ACF lag profile by subtracting the noise ACF from ACF profile in each lag (equation (2.4)).

$$ACF(real, img) = ACF(real, img) - Noise\ ACF(real, img). \qquad (2.4)$$

Figure 2.14 illustrated the result of removing noise from the ACF profile. Since the noise profile is much smaller than the ACF profile, the red plot (ACF profile after noise removal) is hardly distinguishable from the blue plot (ACF profile with noise).
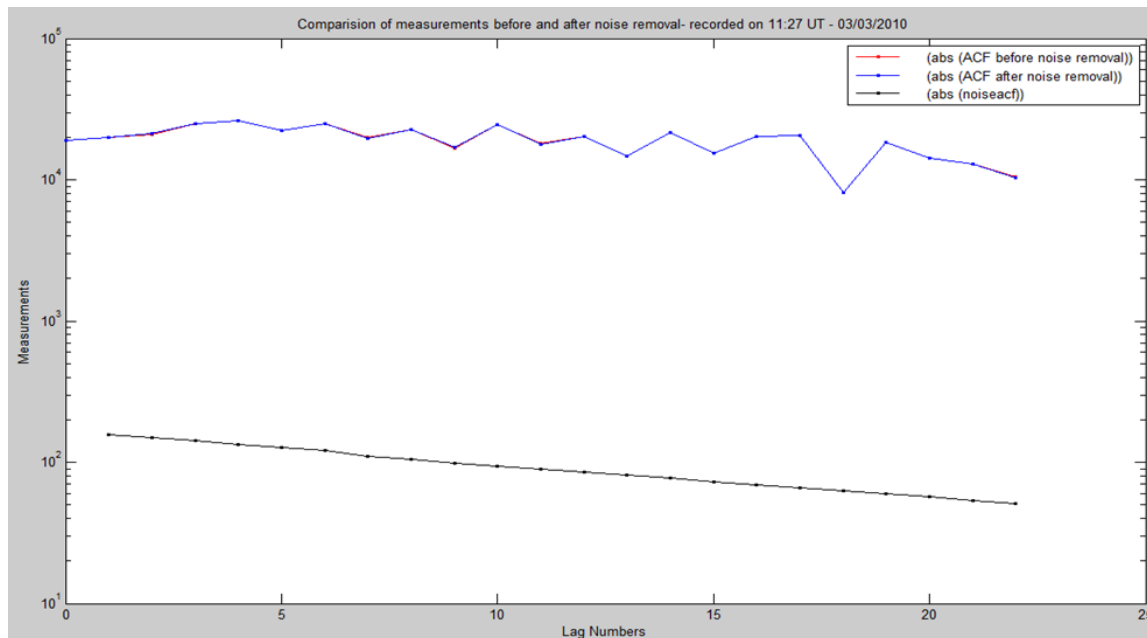
Figure 2.14: Absolute value of the ACF lag profile before (red) and after (blue) noise removal for range 12, beam 8, McMurdo radar. The noise profile values are much smaller compared to the ACF lag profile values.

2.7 ACF Phase Unwrap (FitACFCalcPhiRes and OmegaGuess)

The next step in the FitACF algorithm is phase fitting procedure to derive the Doppler frequency for each range. In this routine, the measured phase (ϕ) for each lag (τ) is obtained in equation (2.5):

$$\phi(\tau) = \tan^{-1}[\frac{img \ (ACF \ (\tau))}{real \ (ACF(\tau))}]. \tag{2.5}$$

The FitACF algorithm makes a preliminary estimation of the Doppler frequency by measuring the slope between each pair of successive good lags in the measured phase profile. The average of all the estimated slopes is the basis for Doppler frequency calculation, referred as *omega guess*. The *omega guess* value is used to add or subtract (positive or negative Doppler shift) multiples of 2π to the measured phase profile to unwrap the phase. Least squares linear fitting is applied to find the slope of the line for unwrapped phase profile. The measured slope is the Doppler frequency of the particular range. In Figure 2.15 range 12, beam 15, McMurodo radar, the measured phase has one 2π jump with negative frequency, thus the phase unwrap algorithm subtracts 2π, where the jump occurs to obtain the unwrapped phase profile.
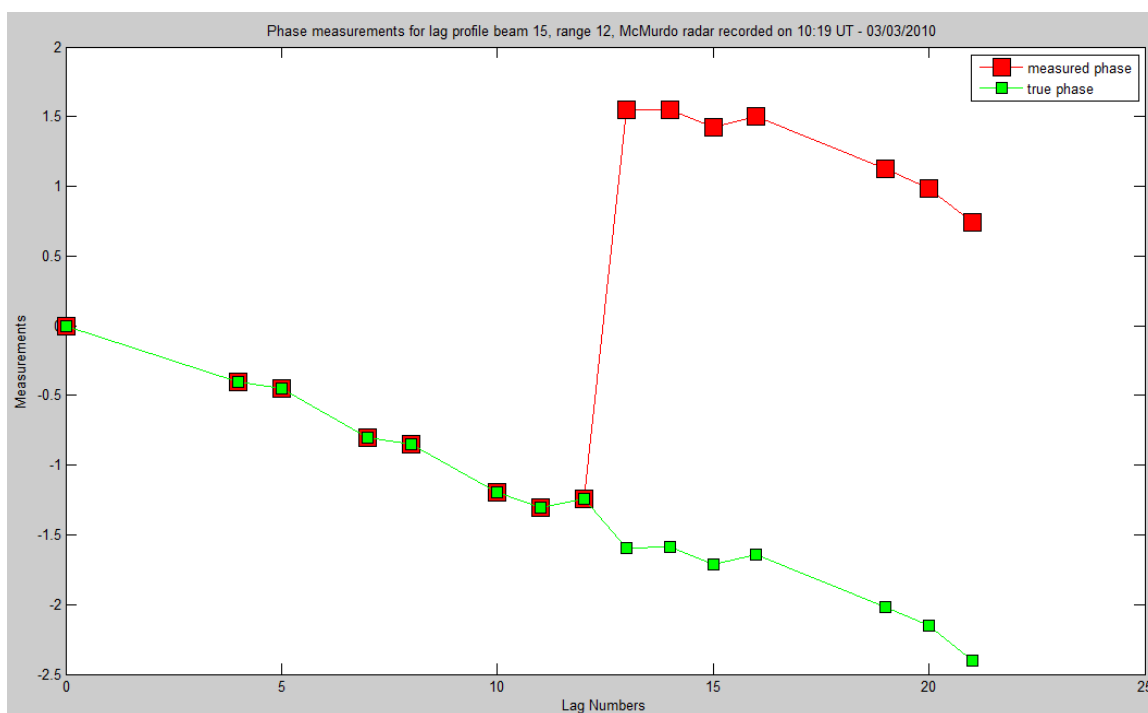
Figure 2.15: Illustration of the measured (red) and unwrapped (green) phase profile for range 12, beam 15, McMurdo radar.

2.8 Doppler Velocity Calculation (DoPhaseFit)

The next step in Doppler velocity measurement is phase fitting procedure on the unwrapped ACF phase profile in each range. Least squares linear fitting is considered for this purpose. Because the imaginary part of the lag-zero power is always zero, the vertical axis intercept of the fitted line is zero and only the slope of the line (f_d) needs to be calculated. This can be obtained even if there are only two points available for fitting, but the slope uncertainty is large in such a case. Equations (2.6) and (2.7) show the procedure to convert the calculated Doppler frequency to Doppler velocity. Where f_d corresponds to the slope of the fitted line to phase profile, C denotes speed of light in free space and $freq_{Tx}$ represents the frequency of the transmitted signal.

$$w = 2\pi f_d. \tag{2.6}$$

The Doppler velocity equals:

$$v = \frac{C \cdot W}{4\pi \cdot freq_{Tx}}. \tag{2.7}$$

Figure 2.16 illustrates the fitted line to the unwrapped phase profile for range 12, beam 15, McMurdo radar.
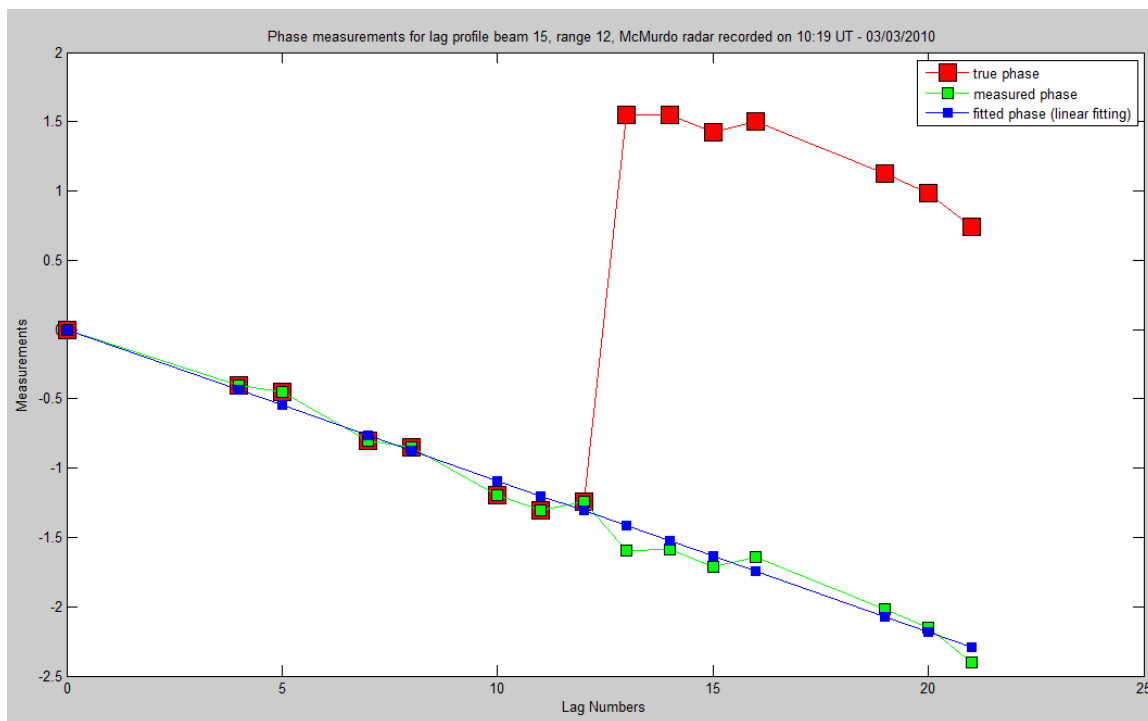
Figure 2.16: Measured and true phase profiles shown in red and green for range 12, beam 15, McMurdo radar. Slope of the fitted line to the true phase profile using linear least-squared fitting determines the Doppler frequency.

2.9 Fitted Power and Spectral Width Calculation (FitACFFitACF)

The ACF lag profile decorrelates over time in each range. The decorrelation rate in time domain corresponds to the spectral width in frequency domain. Non-linear fitting techniques are implemented on the power profile of the ACF to derive the fitted power and spectral width.

The theory assumes that the ACF should decay with lag either exponentially (referred to as Lambda fit) or as a Gaussian (referred to as Sigma fit). The FitACFFitACF subroutine calculates the λ and σ fitting parameters to derive the values of the fitted

power and spectral width in each range. The exponential and Gaussian Fitting equations are given by:

$$R_\lambda(t) = p_\lambda e^{-w_\lambda t}, \tag{2.8}$$

$$R_\sigma(t) = p_\sigma e^{-(w_\sigma t)^2}, \tag{2.9}$$

where the fitted power and spectral width using exponential fitting are denoted by p_λ and w_λ. p_σ and w_σ represent the fitted power and spectral width using Gaussian fitting. Finally, the converted spectral width values for the exponential and Gaussian fitting methods are determined using equations (2.10) and (2.11):

$$w_\lambda = \frac{2C \cdot w_\lambda}{4\pi \cdot freq_{Tx}}, \tag{2.10}$$

$$w_\sigma = \frac{4C \cdot w_\sigma \sqrt{\log(2)}}{4\pi \cdot freq_{Tx}}. \tag{2.11}$$

Figure 2.17 shows the fitted curves for an observed ACF power profile for range 12, beam 15, McMurod radar. The intercept of curves with vertical axis determines the fitted lag zero power.
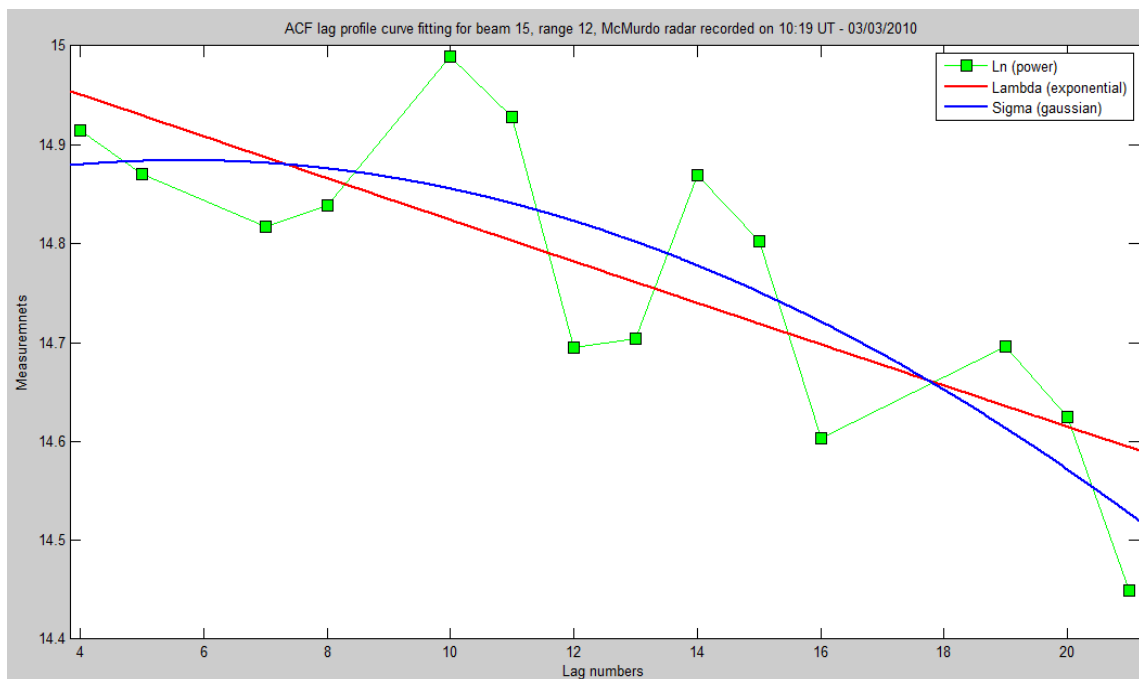
Figure 2.17: Exponential and Gaussian fitted curves to the ACF power profile for range 12, beam 15, McMurdo radar. Decaying parameters (w_λ , w_σ) determine the spectral width.

Chapter 3   Pulse Compression Techniques

Range resolution, the ability of the radar to resolve two targets, depends on the transmitted pulse; a short pulse corresponds to high range resolution. However, the signal to noise ratio for a given range depends on the total transmitted energy. Higher energy in the transmitted pulse increases the ability to reach further distances with higher signal-to-noise ratio. A short pulse with a high peak power is the desirable combination, but the cost of high-power transmitters is high, which motivates looking for other solutions. Pulse compression is a technique to provide the range resolution of a short pulse while transmitting the energy of a long pulse.

In this thesis, techniques for improving the performance of the pulse compression schemes used in SuperDARN were investigated. Specifically the filters used for decoding received pulses were examined. After describing a variety of compression techniques, this chapter presents simulations of mismatched filtering and the application of multiple techniques to SuperDARN observations.

The development of pulse compression first began in 1950s at M.I.T. Lincoln laboratories [8]. Investigations on the idea of "squeezing'' the pulse led to implementation of a filter to accomplish the goal, which was to increase the average power by 10 dB without losing the range resolution and increase in detection by 78 percent. The concept was implemented using a quadratic phase network with many radians of different phase shifts [8]. Figure 3.1 illustrates that the pulse compression (bottom plot) provides the range resolution of a short pulse (top plot) and energy of a long pulse (middle plot). Typical methods of pulse compression include coding of the phase and frequency depending on the application. This section gives an overview of the commonly used frequency and phase coding techniques.

42
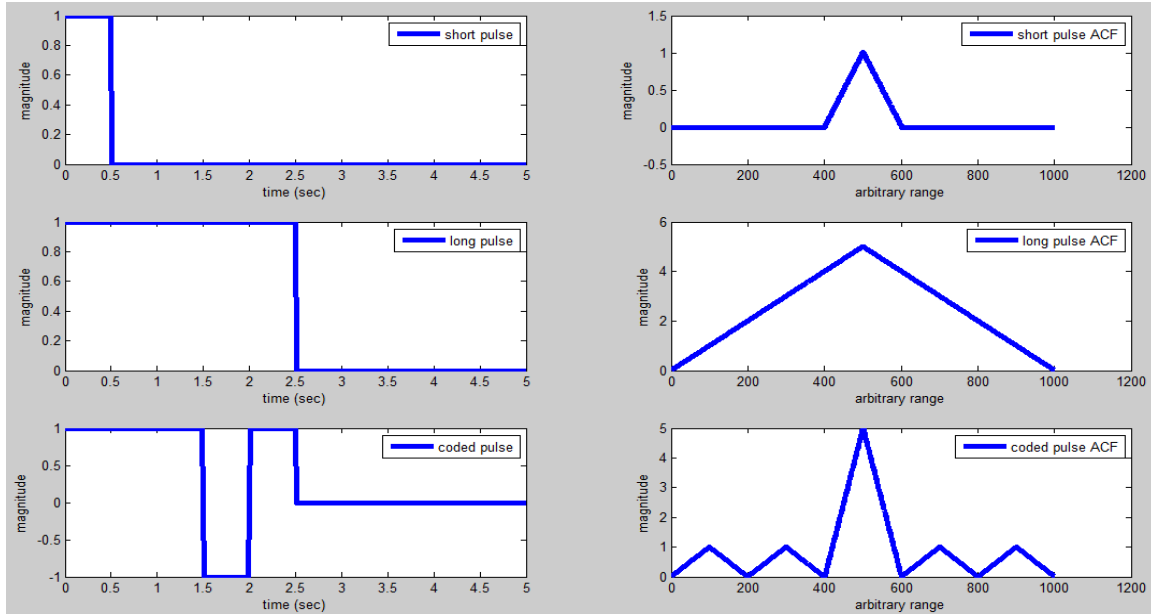
Figure 3.1: Comparison of matched filtering output for a short (top-left), long (middle-left) and compressed pulse (bottom-left). The bottom plot on the right shows matched filtering using pulse compression provides range resolution of a short pulse (top-right) and energy of a long pulse (middle-right).

3.1 Matched Filter

SuperDARN receivers implement matched filtering in their normal mode of operation. A matched filter is an optimal filter that maximizes signal-to-noise ratio of the received signal. Derivation of the matched filtering is given in the following equations [9]:

The output of an arbitrary filter $H(w)$ with returns from a point target is represented by:

$$y(t) = \int b e^{j\phi} X(w) e^{-jwt_d} H(w) e^{jwt}, \tag{3.2}$$

where $b e^{j\phi} X(w) e^{-jwt_d}$ is the radian frequency (w) spectrum of the return from a target at time delay t_d, for measured phase of ϕ and amplitude of b.

The output of the filter to white noise with Gaussian distribution and zero mean equals:

$$\overline{n^2\,(t)} = \frac{N_0}{2\pi}\int |H(w)|^2\,dw, \tag{3.3}$$

where, N_0 is the power spectral density of the noise and bar represents the expectation value. The signal-to-noise ratio at the output of the filter at time delay t_d equals:

$$SNR = \frac{|y(t_d)|^2}{\overline{n^2(t_d)}},$$

which can be expressed as:

$$SNR = \frac{b^2|\int X(w)H(w)dw|^2}{2\pi N_0 \int |H(w)|^2 dw}. \tag{3.4}$$

In order to reach the maximum value for SNR in equation (3.4), the numerator must be maximized. To satisfy this, Schwartz inequality given here:

$$|\int X(w)H(w)dw|^2 \le \int |X(w)|^2 dw \int |H(w)|^2 dw, \tag{3.5}$$

shows that for inequality to have its maximum value, the two sides should be equal. This results in:

$$H(w) = ax^*(w), \tag{3.6}$$

which in time domain equals the complex conjugate time reversed image of the transmitted signal. Thereby, resulting in optimal signal-to-noise ratio estimation.

The output of a matched filter is the convolution of the transmitted signal ($x(t)$) with time reversed conjugate of itself ($\overline{x(-t)}$) that corresponds to the receiver filter impulse response:

$$y(\tau) = \int_{-\infty}^{\infty} x(t)\overline{x(t-\tau)}dt. \tag{3.7}$$

Matched filtering along with pulse compression optimizes the signal-to-noise ratio. However, as shown in Figure 3.1 side lobes are present in the matched-filter output, which may be an undesirable property. To evaluate performance of the pulse compression techniques, two parameters are introduced here. Peak-to-side-lobe ratio and

integrated-side-lobe level given in equations (3.8) and (3.9) are the parameters that measure the ability of the filter to suppress the undesired side lobes:

$$PSL\ (Peak\_Sidelobe\_Level) = 10 \log \ \max \left(\frac{x_i^2}{x_0^2}\right), \qquad (3.8)$$

$$ISL\ (Integrated\_Sidelobe\_Level) = 10 \log \ \sum_{i=0}^{n}\left(\frac{x_i^2}{x_0^2}\right). \qquad (3.9)$$

In equations, (3.8) and (3.9), x_0 denotes the voltage of the main lobe and x_i represents the voltage of the *ith* sidelobe for total number of n sidelobes.

3.1.2 Ambiguity Function

The radar ambiguity function $(y(\tau, f_d))$ is a three-dimensional function showing the output of the matched filter when the received target of interest is subjected to Doppler frequency of f_d and time delay of τ. It shows how the output is distorted when it is Doppler shifted and delayed from the receiver it was matched to. $y(0,0)$ represents the output of the matched filter for no Doppler shift. The ideal ambiguity function is a spike at zero time delay and frequency and tends to be zero in other places. This does not result in interference with other targets when the target of interest is subjected to delay and Doppler shift. The radar ambiguity function for a pulse $(x(t))$ is defined in equation (3.10):

$$y(\tau, f_d) = \int_{-\infty}^{\infty} x(t)x^*(t-\tau)e^{j2\pi f_d t}dt \ . \qquad (3.10)$$

3.2 Frequency Coding (Stepped Frequency Waveform and Costas Code)

Frequency coding is a type of pulse compression in which a pulse of length T is divided into N subpulses, each of width τ. If the frequency is increased by Δf from one subpulse to the next in a linear fashion, it is considered SFW (Stepped Frequency Waveform). Table 3.1 shows the frequency assignment of the SFW for an arbitrary pulse length of 10 with 10 subpulses..

Table 3.1: Frequency assignment for SFW code of length 10. The frequency increases linearly from on sub pulse to the next.

	0	1	2	3	4	5	6	7	8	9
10										•
9									•	
8								•		
7							•			
6						•				
5					•					
4				•						
3			•							
2		•								
1	•									

Conversely, if the frequency changes from one pulse to the next in a quasi-random fashion, the scheme is called frequency hop coding. Table 3.2 shows the frequency assignment of a special set of frequency hop coding (Costas code) for an arbitrary pulse length of 10.

Table 3.2: Frequency assignment for Costas code of length 10. The frequency is assigned randomly from one sub pulse to the next.

	0	1	2	3	4	5	6	7	8	9
10						•				
9							•			
8				•						
7								•		
6									•	
5					•					
4			•							
3										•
2		•								
1	•									

In addition to the main lobe signal-to-noise ratio, side lobe suppression and time bandwidth performance, tolerance in Doppler shift is another important factor in comparing pulse compression techniques when dealing with moving targets. Figures 3.2 shows the plot of ambiguity function for Costas code. The cut of an ambiguity function at zero frequency represents the matched filter output when the target is stationary, however, for a non-stationary target the output of the filter does not preserve the same properties and is denoted Doppler distorted. This is considered a disadvantage when the radar deals with moving targets. Figures 3.3 shows a plot of the ambiguity function for SFW code. In Figure 3.2, the thumbtack shape of the ambiguity function in Costas frequency coding makes it advantageous compared to that of the SFW, since it is more Doppler tolerant.
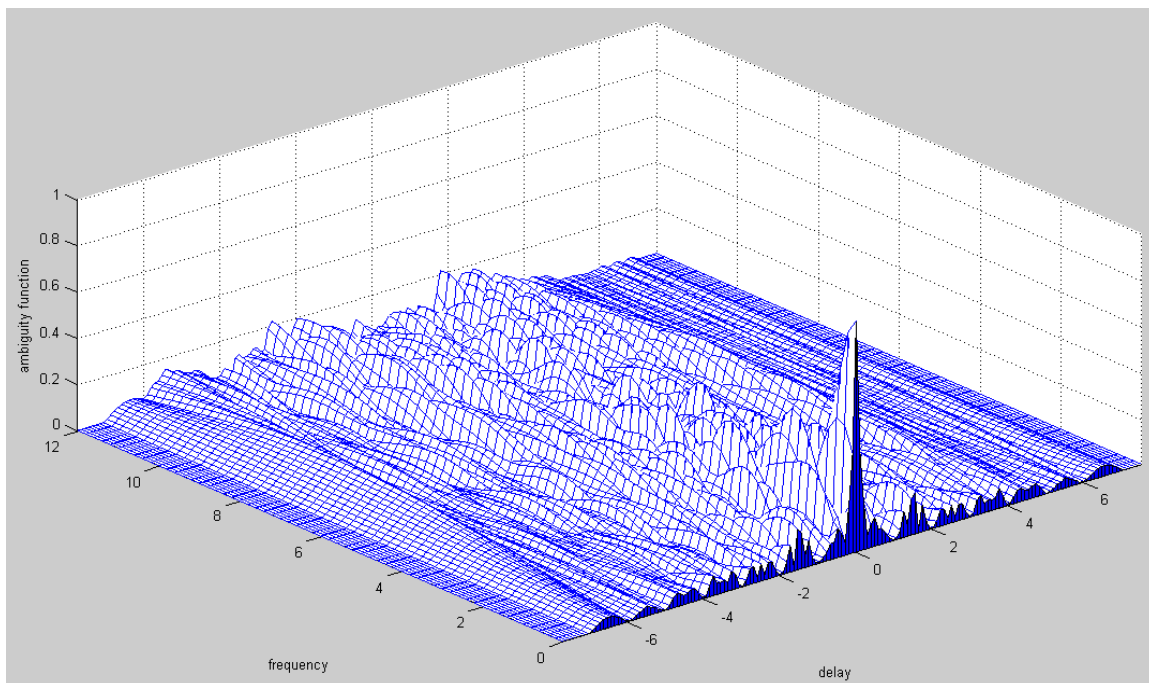
Figure 3.2: Ambiguity function of the Costas code of length 7 [4 7 1 6 5 2 3].
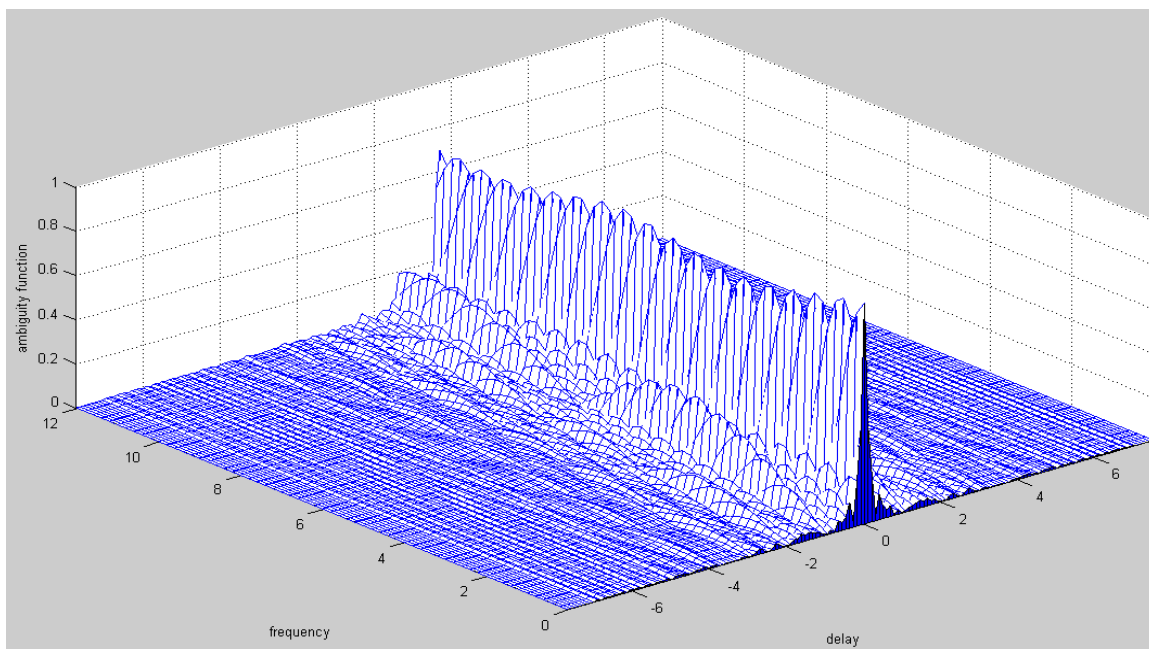
Figure 3.3: Ambiguity function of the SFW code of length 7 [1 2 3 4 5 6 7].

3.3 Phase Coding

Phase coding is another approach for pulse compression in which a pulse of length T is divided into N subpulses, each of width τ. The transmitter modulator changes the phase of the subpulses with the desired phase shift. If the waveform is binary phase coded, the phase changes 180˚ from one subpulse to another. In the case of polyphase-coded waveforms, the pulses will be composed of multiple phases with a fundamental phase jump of less than 180˚. The type of phase coding for the waveform depends on the application, but the general idea is to implement the codes that provide the highest signal-to-noise ratio for the main lobe and considerable suppression for side lobes. In this section, three different types of phase coding schemes including Barker coding, Golay coding and Frank codes are studied.

3.3.1 Barker Code

Barker code is an optimal binary phase-coded sequence with relatively low sidelobes and no signal-to-noise ratio loss for the main lobe. There are a number of known Barker codes with lengths from 2 to 13 that exhibit the same properties such as, optimum singal-to-noise ratio for the main lobe, symmetric autocorrelation with low side lobes. Figure 3.4 shows the Barker code of length 13; Positive amplitudes indicate 0 phase and negative indicates π radian difference.
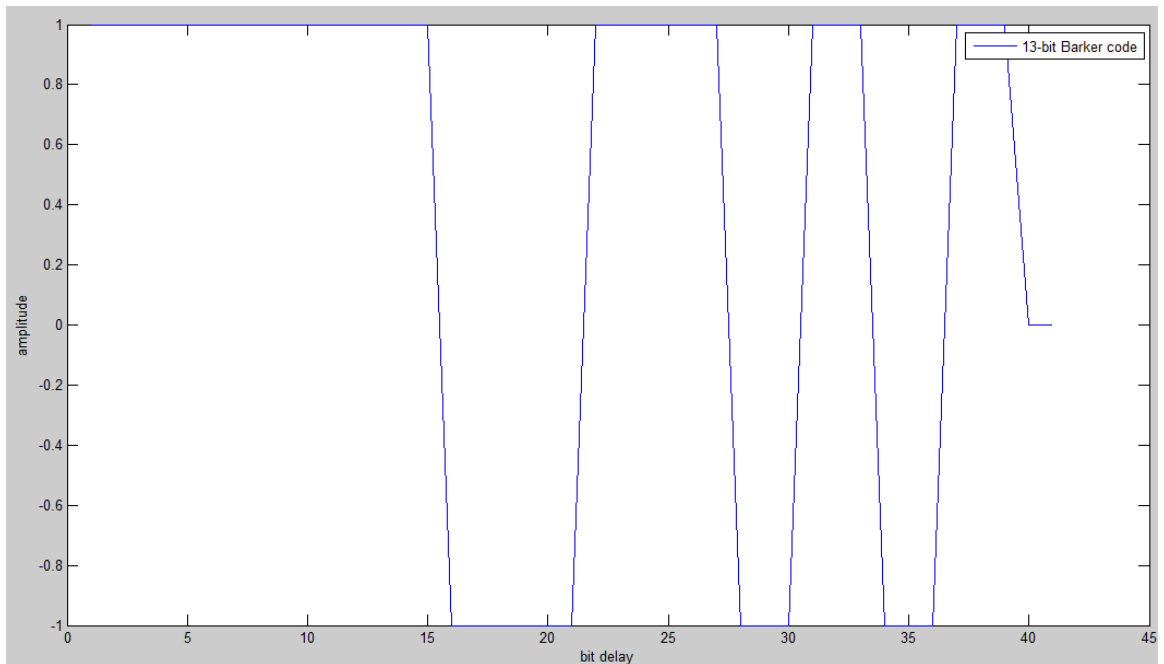
Figure 3.4: Standard 13-bit Barker code.

Figure 3.4 shows the 13-bit Barker coded waveform and the output of the matched filter is demonstrated in Figure 3.5. There are six equal time side-lobes to either side of the peak, each 22.3 dB below the peak that makes 13-bit Barker code an ideal phase coding scheme for many applications.
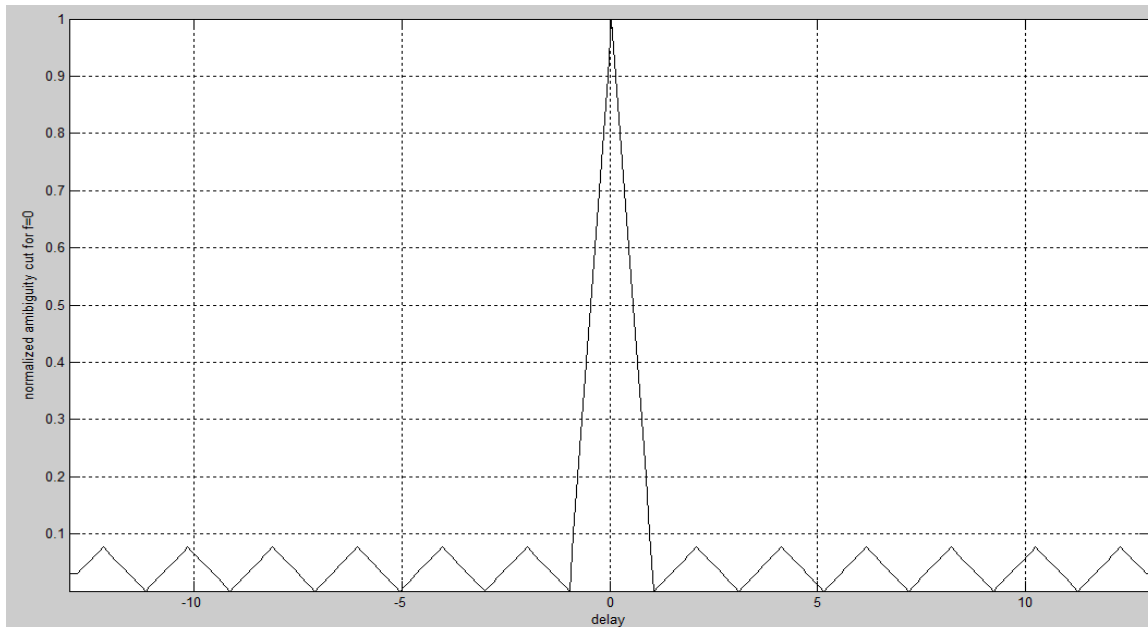
Figure 3.5: 13-bit Barker code normalized Auto correlation function.

Figure 3.6 represents the 13-bit Barker code ambiguity function. In this Figure, although relatively low side lobes compared to the main lobe is an advantage, Barker coding tends to be less Doppler tolerant when dealing with non-stationary targets.
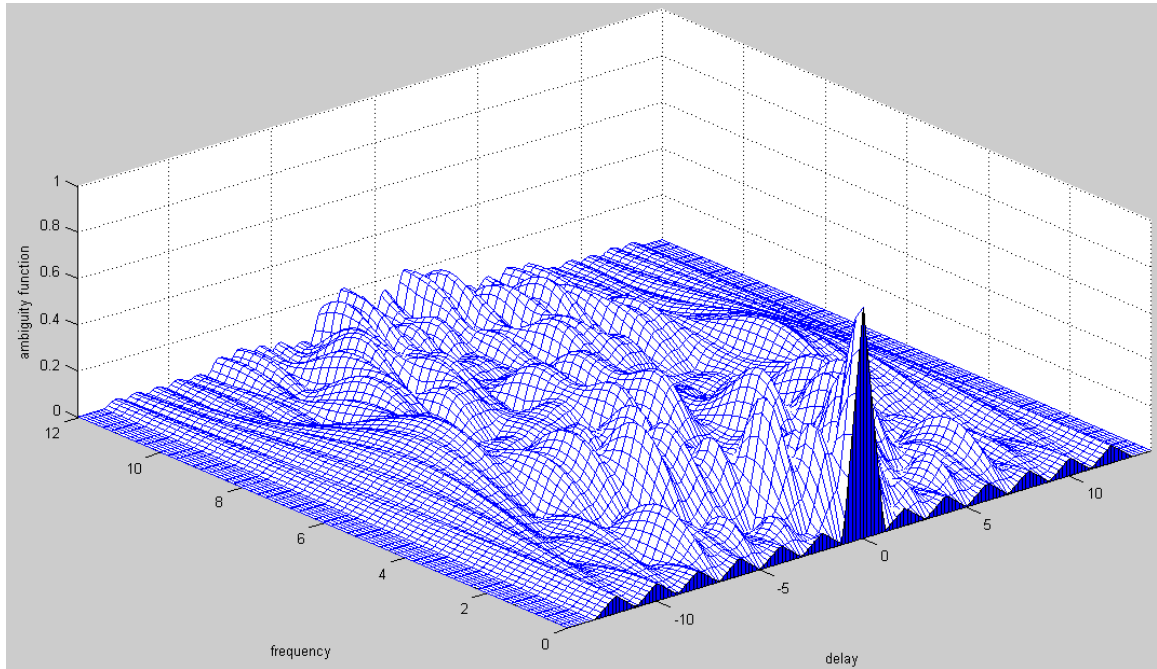
Figure 3.6: 13-bit Barker code ambiguity function.

3.3.2 Complementary Golay Code

Use of complementary Golay codes is another method to eliminate side lobes of the matched filter output. The Golay code consists of a pair of complementary sequences, in which the sum of the autocorrelation functions of the sequences is zero for all time shifts except zero. While the Golay code seems an ideal technique for pulse compression, the correlation time makes it impractical for radars such as SuperDARN. The correlation time of the target in the Golay coding must be larger than the time it takes to receive returns for both pulses. Otherwise, the pulse returns do not preserve their shapes and sum of the sidelobes do not cancel out each other. Figure 3.7 shows the pulse sequences of 16-bit Golay code.

52
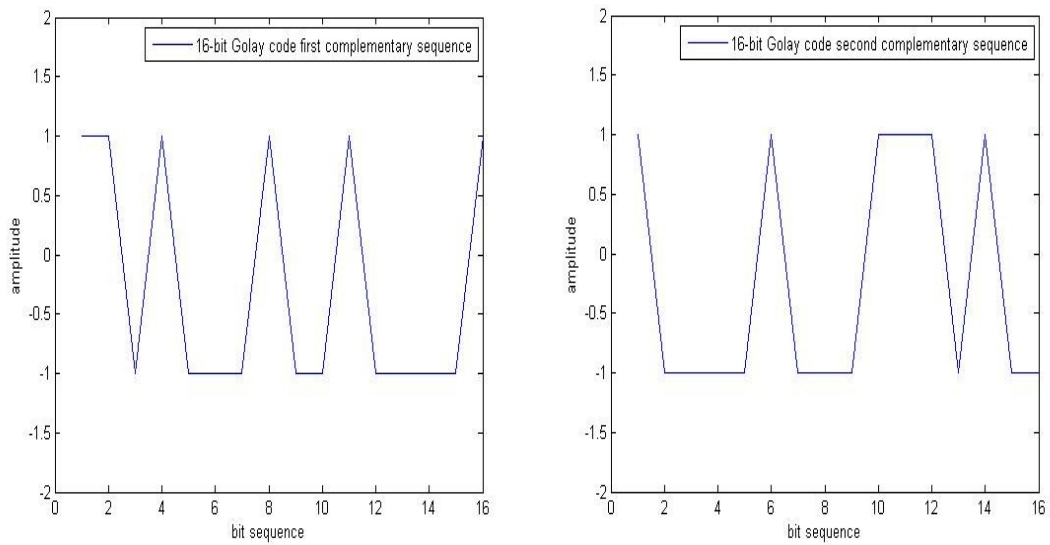
Figure 3.7: The complementary pulse sequences of 16-bit Golay code.

The output of the matched filter for the received Golay coded pulse sequences is shown in Figure 3.8. Except the mainlobe, the other lobes are symmetric to each other. Adding these two ACFs removes all the sidelobes as illustrated in Figure 3.9.
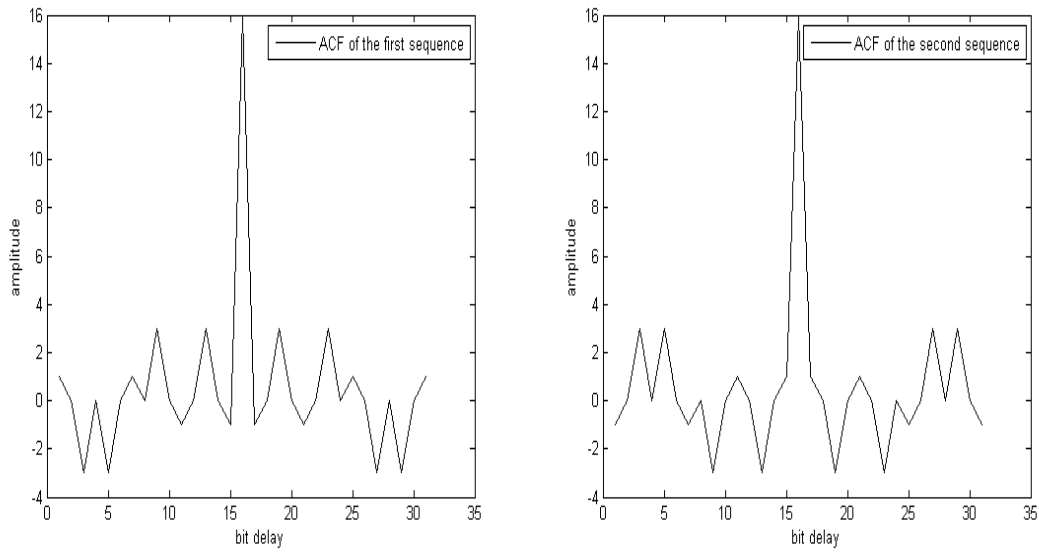
Figure 3.8: ACF of the complementary Golay code of length 16. ACF of the each pulse is this scheme have the same magnitude but symmetric
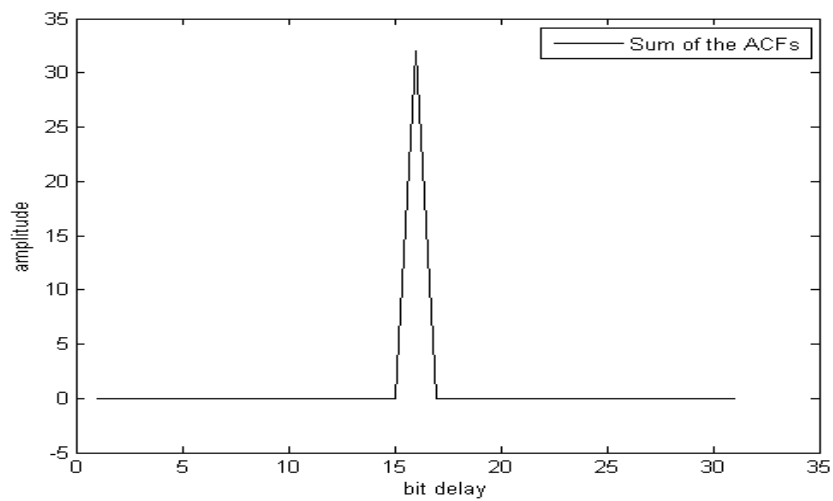
Figure 3.9: Sum of the ACFs of the Golay code. The symmetric sidelobes cancel out each other while the power in the main lobe increase.

3.3.3 Frank Code

Frank code is another type of polyphase coding where the phase of each subpulse equals [9]:

$$\phi_{n,k} = \frac{2\pi}{M} nk \qquad n, k = 0, \dots, (M-1). \tag{3.11}$$

In this equation, the phase is indexed over n (number of subpulses) for each value of k. Phase in each subpulse changes from one subpulse to another based on the fundamental phase offset. Another requirement for Frank code is that the length of the code should be square. The ambiguity function for a 16-bit Frank code ($F_{16=[1,1,1,1,1,j,-1,-j,1,-1,1,-1,1,-j,-1,j]}$) is shown in Figure 2.10 where the phase shift is 90˚. Although the thumbtack shape of the autocorrelation function with low side lobes makes the Frank code an ideal choice, for a moving target, it is not considered a practical coding scheme.
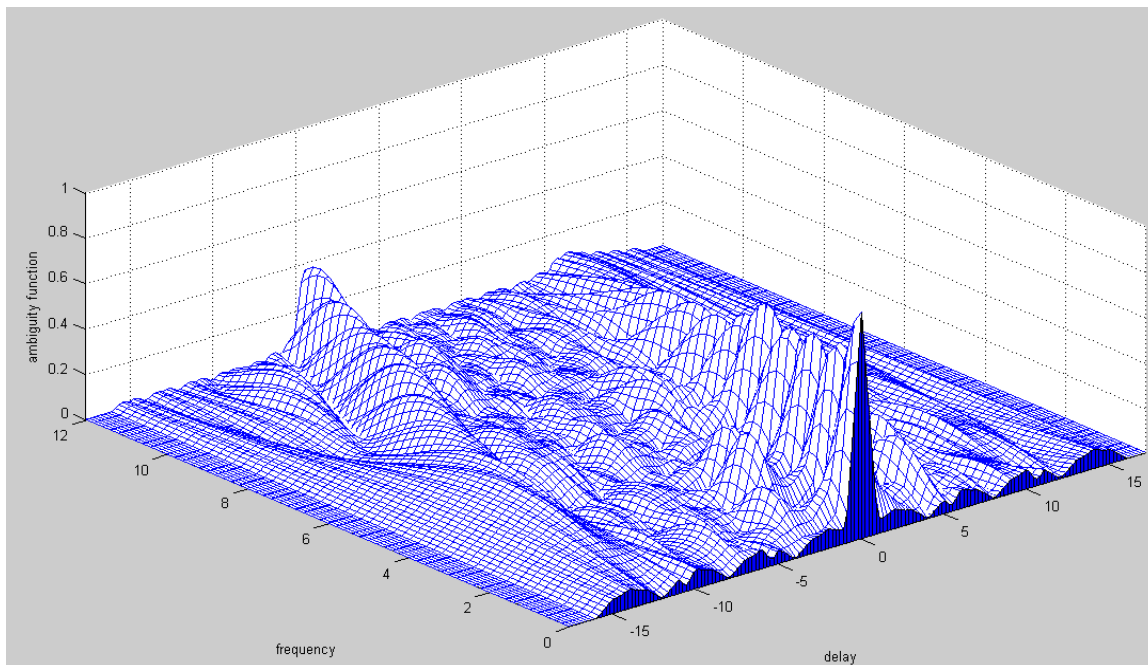
Figure 3.10: Ambiguity function of the Frank code of length 16.

3.4 Mismatched Filtering

As discussed in earlier sections, pulse compression provides range resolution of a short pulse and energy of a long pulse. However, matched filter processing of compressed pulses leads to generation side lobes. Matched filtering maximizes the SNR of the decoded signal without optimizing the side lobe levels. A new method of eliminating side lobes of the auto-correlation function is addressed in this section by means of mismatched filtering. Mismatched filter results in a side-lobe-free output of the filter by optimizing the filter coefficients. However, the cost of this optimization is an associated signal-to-noise ratio loss for the main lobe compared to that of the matched filter. The interesting property for this type of filtering is that the mismatched filter coefficients can be obtained for any phase-coded pulse as long as there is no frequency component with zero value in the frequency response of the phase-coded pulse. There are variety methods in the time and frequency domains for calculation of the mismatched filter coefficients. The method discussed here uses frequency domain estimation and is expressed in equations (3.12) to (3.16) [10]:

An encoded pulse ($\varepsilon(n)$) with length n can be written as:

$$\varepsilon(n) = p(n) * h_c(n), \tag{3.12}$$

Where $*$ denotes convolution, $p(n)$ is the elementary pulse and $h_c(n)$ denotes the impulse response of the encoding filter. The decoded pulse equals:

$$\lambda(n) = q(n) * h_d(n), \tag{3.13}$$

where $q(n)$ is time inverse of the $p(n)$, and $h_d(n)$ represents the impulse response of the decoding filter. Output of the filter is given equation (3.14):

$$w(n) = \varepsilon(n) * \lambda(n). \tag{3.14}$$

In frequency domain, we have:

$$w(f) = \varepsilon(f)\lambda(f) = p(f)h_c(f)q(f)h_d(f), \tag{3.15}$$

where (f), $q(f)$, $h_c(f)$ and $h_d(f)$ represent the Fourier transforms of $p(n), q(n)$, $h_c(n)$ and $h_d(n)$ respectively. Finally, for a side-lobe-free output, the desired decoding filter coefficients can be calculated by:

$$h_d(n) = \mathrm{F}^{-1}\left(\frac{1}{h_c(f)}\right). \tag{3.16}$$

Equation (3.16) shows that if the multiplication of Fourier transforms of the encoding and decoding filter impulse responses equal one, what we are left with is just the elementary pulses that do not contribute to the side lobes. An appropriate mismatched filter results in no side lobes, but depending on the length of the filter, the SNR of the main lobe is lower compared to the matched filter. Figure 3.11 shows the impulse response of the matched and mismatched filter for 13-bit Barker code. Both plots look similar except the coefficients in the mismatched filter have ripples around +1 and -1 amplitude, and the length of the filter is almost three times that of the matched filter.
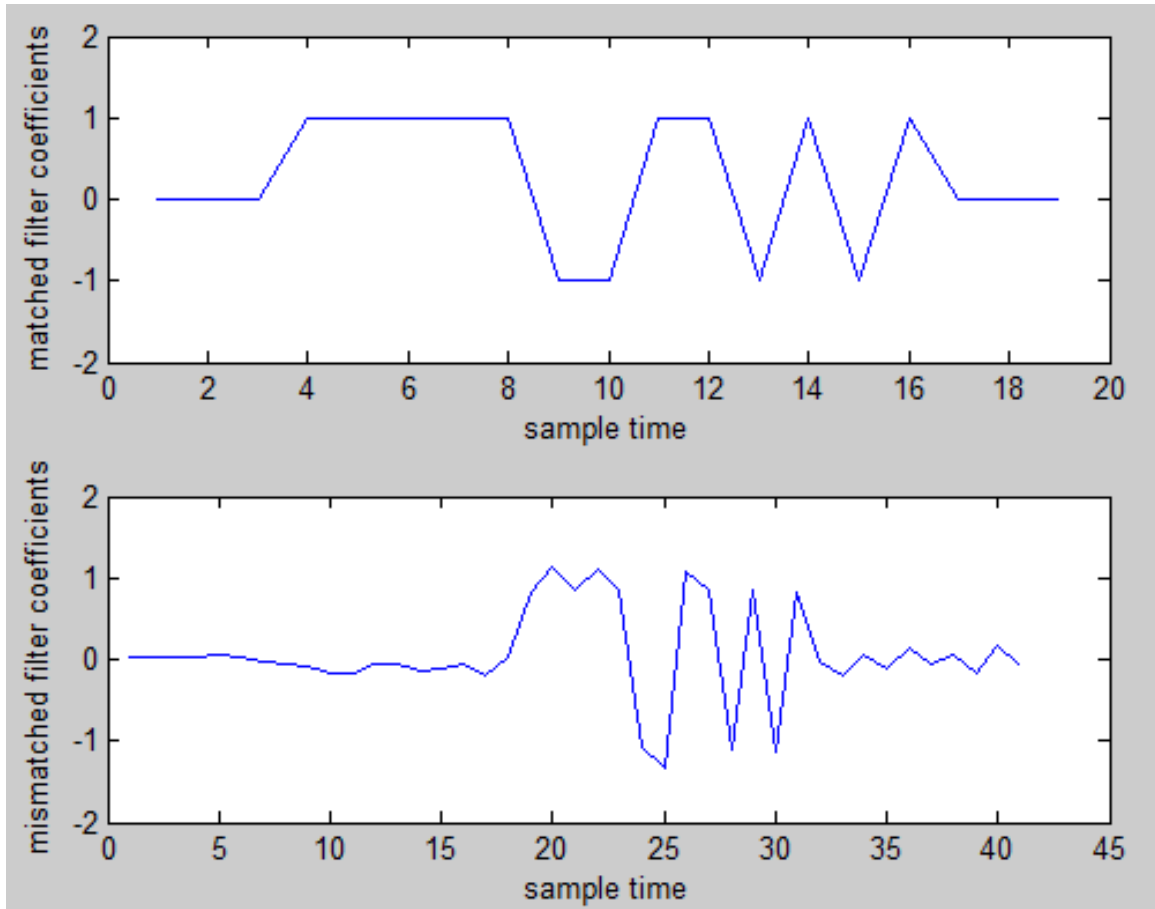
Figure 3.11: Top plot: Filter coefficients of the 13-bit Barker code matched filter. Bottom plot: Filter coefficients of the 13-bit Barker code mismatched filter.

Cross correlation of the 13-bit Barker code (encoding signal) and the mismatched filter is shown in Figure 3.12. For the 13-bit Barker code, the mismatched filter SNR loss of the main lobe is 5% compared to the matched filter output.

58
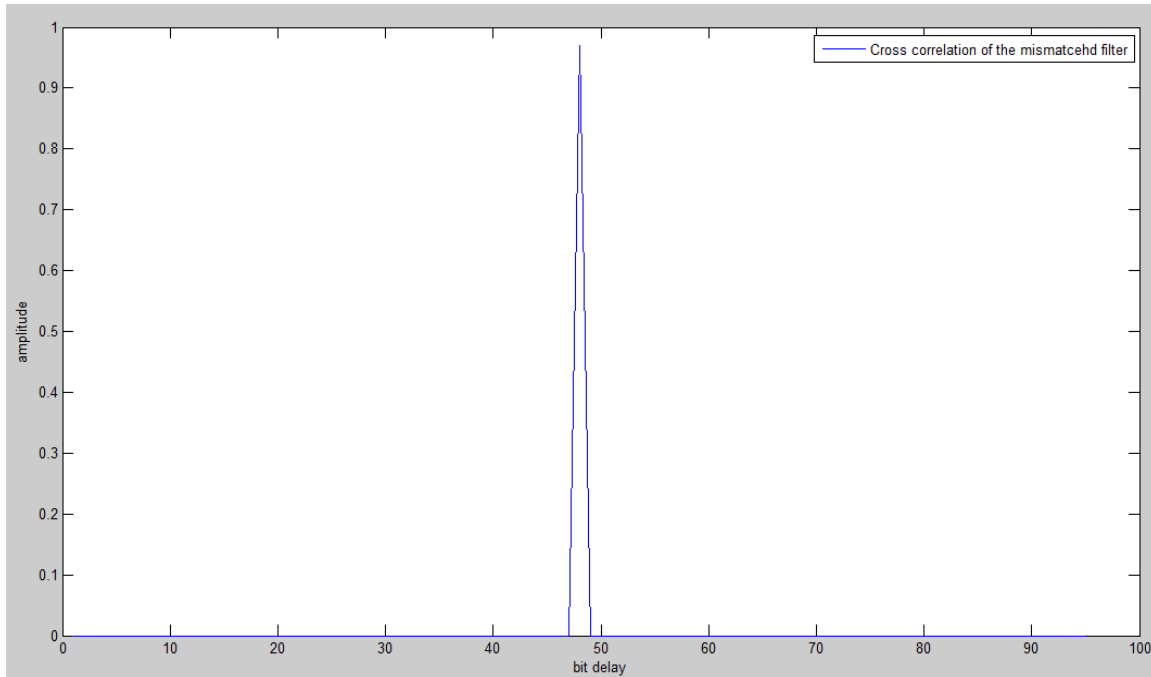
Figure 3.12: Cross-correlation of the mismatched filter and 13-bit Barker code.

In Figure 3.11, the length of the mismatched filter is approximately three times of that of the matched filter. More coefficients (longer filter) results in improved filtering in terms of both side lobe suppression and SNR performance of the main lobe. The following example illustrates performance of a mismatched filter compared to the matched filter.

The example result is shown in Figures 3.13 and 3.14, where two point targets with different cross sections were simulated. In Figure 3.14 two targets are set far from each other while in Figure 3.14 are placed next to each other to evaluate how each filtering method performs. The output of the matched filter in Figure 3.13 for a target with higher return power has larger side lobes. Hence, if placed close to the smaller target contaminates with the smaller target and affects the value of the received power. The green and red plots in Figure 3.14 illustrate performance of the matched and mismatched

filters. Even if the two targets are next to each other, the mismatched filter output has a very low side lobes, consequently does not affect the true value of the smaller target.
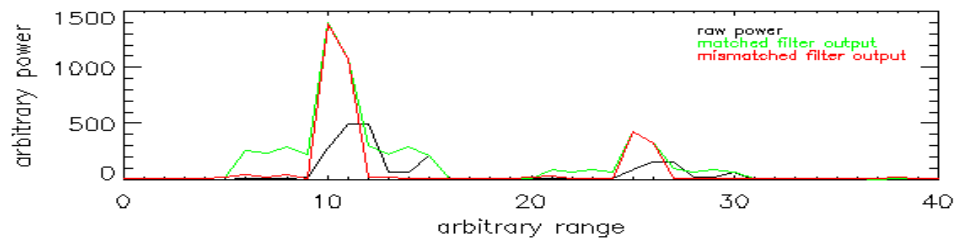
Figure 3.13: Performance of matched and mismatched filtering when two targets are placed far from each other. Matched filtering output (green) large side lobes are significantly suppressed in mismatched filtering (red).
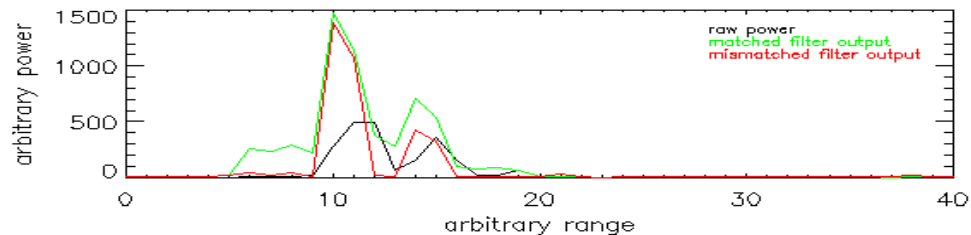
Figure 3.14: Performance of matched and mismatched filtering when two targets are placed next to each other. Side lobes of the matched filtering (green) output for high SNR target contaminate with the smaller target and affect the true value of the power, while the mismatched filtering (red) returns the same result in Figure 3.13.

Table 3.3 shows performance of both matched and mismatched filter outputs for a high SNR target. For a nominal loss of SNR in the main lobe, the mismatched filtering outperforms the matched filtering in terms of the side lobe removal. For this reason, mismatched filtering is considered as an alternative to the matched filtering when the side lobe suppression is priority.

60

Table 3.3: Performance of matched and mismatched filtering in terms of PSL, ISL and main lobe power loss.

	Matched filter	Mismatched filter
PSL (dB)	-13.459	-30.203
ISL (dB)	-5.7367	-26.12
Power loss (dB)	0	0.13

In order to validate the theory and simulated examples, an observation is presented to compare performance of each method in practice. Figure 3.15 shows the experimental results taken from Kodiak radar on 06/08/2011 at 16:00. Meteor echo returns follow the transmitted pulses within the sequence.
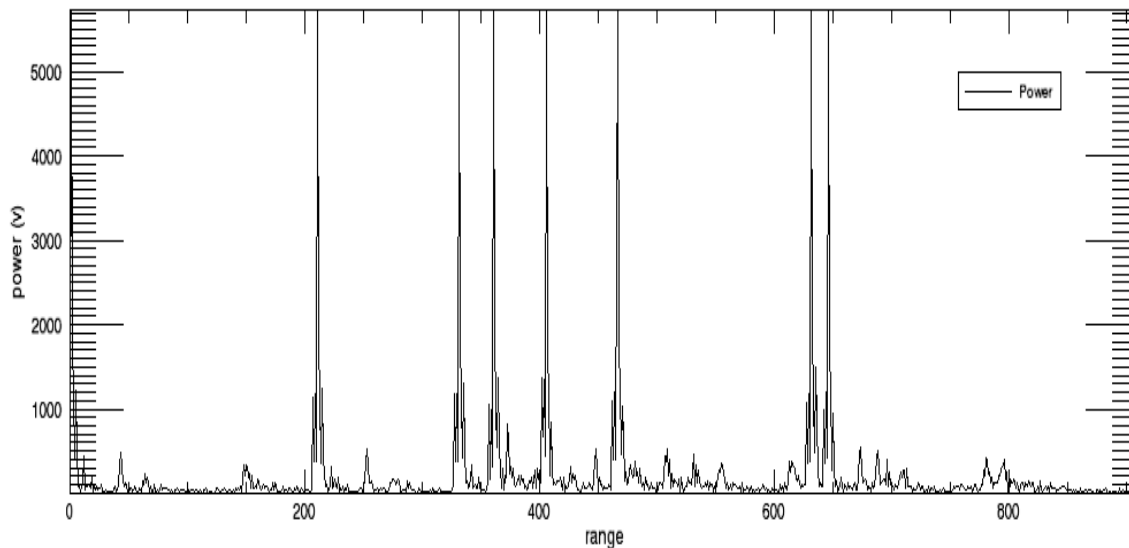
Figure 3.15: Received samples for Kodiak radar on 06/08/2011. The transmitted signal samples along with received samples from ionospheric irregularities, meter echo is where the spikes are located and repeat in the same range after each transmitted pulse.

Figure 3.16 illustrates the matched and mismatched filters output for ranges 220:320, the meteor is located at range 253. The green plot is the output of matched filter and the red corresponds to mismatched filter. For a nominal loss of signal-to-noise ratio, the mismatched filtering demonstrates superior performance in terms of both peak-to-side-lobe level and integrated-side-lobe level.
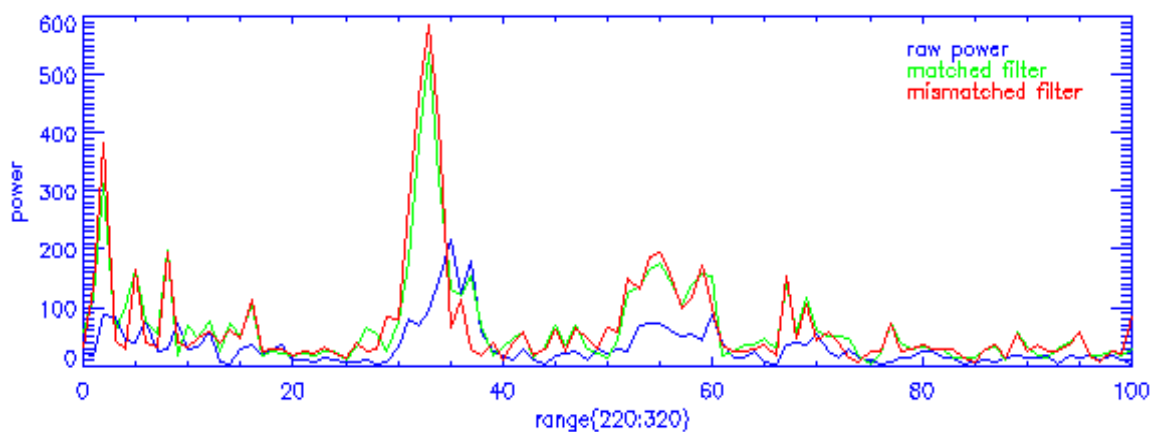
Figure 3.16: Meteor echo observation and performance of the matched and mismatched filtering for Kodiak radar on 06/08/2011. The blue plot shows the received raw power; green illustrates the output of matched filter and the red corresponds to the mismatched filter output.

3.5 Adaptive Filtering

The matched and mismatched filter impulse responses are calculated using replica of the transmitted signal. Despite the assumption that the returned signal from a point target is the attenuated replica of the transmitted signal, depending on the environment where the signal travels and factors such as, noise, Doppler shift, and interference, the received signal shape can be altered. Thereby, matched and mismatched filters response might not be ideal in practice in some cases. An alternative means, adaptive filtering, estimates filter coefficients using the received signal, not the transmitted one. In this approach, the filter coefficients change from one range to another according to the defined algorithm. For each range gate, the filter coefficients are calculated based on the

received samples and an estimate of noise power. A MMSE (Minimum Mean Squared Error) estimator is the approach to minimize the cost function and estimate the adaptive filter coefficients in an open-loop manner [11]. Calculating the optimum filter coefficients for each range gate in adaptive filtering allows for improved side lobe estimation and removal without the associated signal-to-noise-ratio loss of the main lobe.

In phase coding schemes in the discrete domain, for an n-bit coded transmit pulse $(S = Transpose([s(0)\ s(1)\ ...\ s(n-1)]\ ))$ the matched filter output for the desired range (r) is expressed in equation (3.17), where T corresponds to transpose and H denotes matrix Hermitian [11]:

$$y(r) = s_f^H A(r)^T s + s_f^H (additive\ noise).$$

(3.17)

In equation (3.17), A(r) equals:

$$A(r) = \begin{bmatrix} x(r) & x(r+1) & ... & x(r+n-1) \\ x(r-1) & x(r) & ... & x(r+n-2) \\ \vdots & \vdots & \ddots & \vdots \\ x(r-n+1) & x(r-n+2) & ... & x(r) \end{bmatrix},$$

and $x(r)$ is the impulse response of the range profile. For a solitary point target, all of the off-diagonal elements of $A(r)$ are zero. For an overspread target, $A(r)$ changes from an identity matrix to a matrix with non-zero values in off-diagonal elements. This changes the properties of the matrix such as, identity, sparsity depending on the length of the phase-coded waveform.

For a collection of n samples of the received signal and the processing window of $L\ (r = 0,1,2, ... , L - 1)$ the output is written as:

$$y(r) = s_f^H [A(r)^T s + (additive\ noise)].$$

(3.18)

In equation (3.18) the matched filter (S_f) is replaced with $w(r)$ and the filter coefficients are estimated using the range cells prior to a particular range cell as a priori information. The standard cost function is described as:

$$j(r) = E[|x(r) - w^H(r)y(r)|^2],$$

where $E[]$ denotes the expectation value and H indicates Hermitian. The cost function is minimized by differentiating with respect to $W(r)$ and setting the results to zero. For each range gate, the filter coefficients are obtained using equation (3.19):

$$w(r) = \rho(r)(c(r) + R(r))^{-1}s, \qquad (3.19)$$

where $R(r)$ is the noise covariance matrix, $\rho(r) = |x(r)|^2$ and $c(r)$ is given in (3.20):

$$c(r) = \sum_{m=-n+1}^{n-1} \rho(r+m)s_m s_m^H, \qquad (3.20)$$

where s_m is the transmit pulse-coded bits shifted by m samples and the remainder set to zero. The algorithm determines the filter coefficients for each range following steps 1 to 5 [11]:

1) Collect samples for the desired processing window (L) plus $I(n-1)$ samples before and after the processing window (I is the number of iterations and n equals the length of the pulse sequence.).

2) For the initialization stage, assume the received power is constant across all ranges and noise is negligible. Find the adaptive filter coefficients.

3) Use stage 2 estimated power to calculate the noise covariance matrix and new filter coefficients.

4) Employ the new filter coefficients for the current iteration and remaining ranges to estimate power.

5) Repeat stage 4 until the desired length (L) of processing window is achieved.

Two case studies are presented here to compare performance of the matched, mismatched, and adaptive filtering. In the first case, a low SNR target and for the second one a high SNR target is simulated. Figure 3.17 illustrates performance of each method when the low SNR point target is placed at range 10. The top plot in this Figure shows the first iteration of the adaptive filtering. Since there is no information regarding the noise, the output of the filter is the same as matched filter. In the middle plot as the iteration increments, the algorithm allows for more precise estimation and removal of the noise and side lobes. In this example, the desired response (bottom plot) is obtained in the 5th iteration where the adaptive filtering achieves its optimum response.
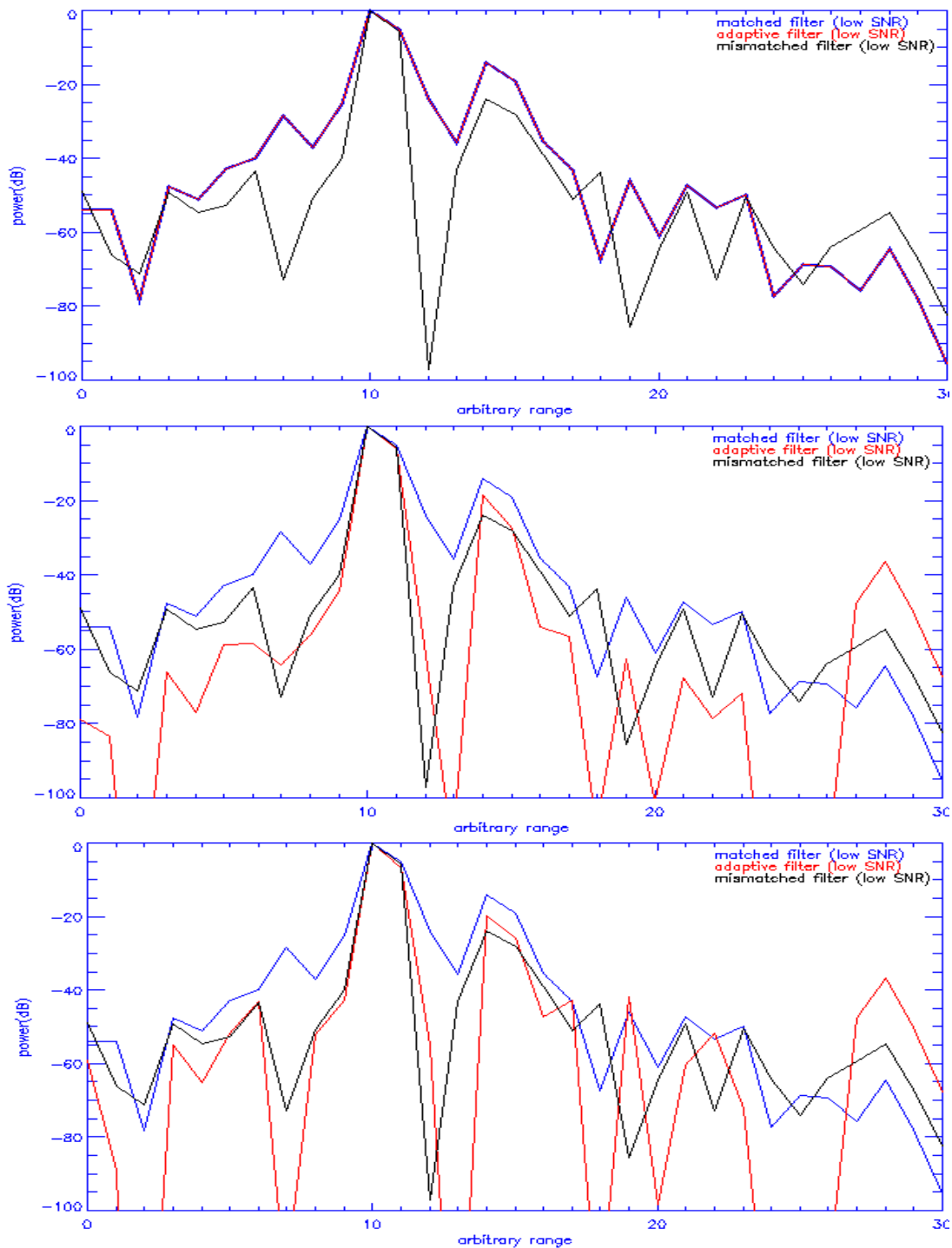
Figure 3.17: Comparison of matched, mismatched and adaptive filtering for a low SNR target. In 1st iteration (top plot) the adaptive filtering output is identical to matched filtering. As the iteration carries on, the adaptive filtering estimates and remove more noise and side lobe (3rd iteration-middle plot) and reaches optimum answer in the 5th iteration (bottom plot).

Figure 3.18 illustrates performance of each approach when the high SNR point target is placed at range 10. The top plot in the Figure shows output of the first iteration of the adaptive filtering. Since there is no information, the output of the filter is identical to matched filter. In the middle plot as the iteration increments, the algorithm allows for more precise estimation and removal of the noise and side lobes. The desired response for this example is obtained in the 3rd iteration.
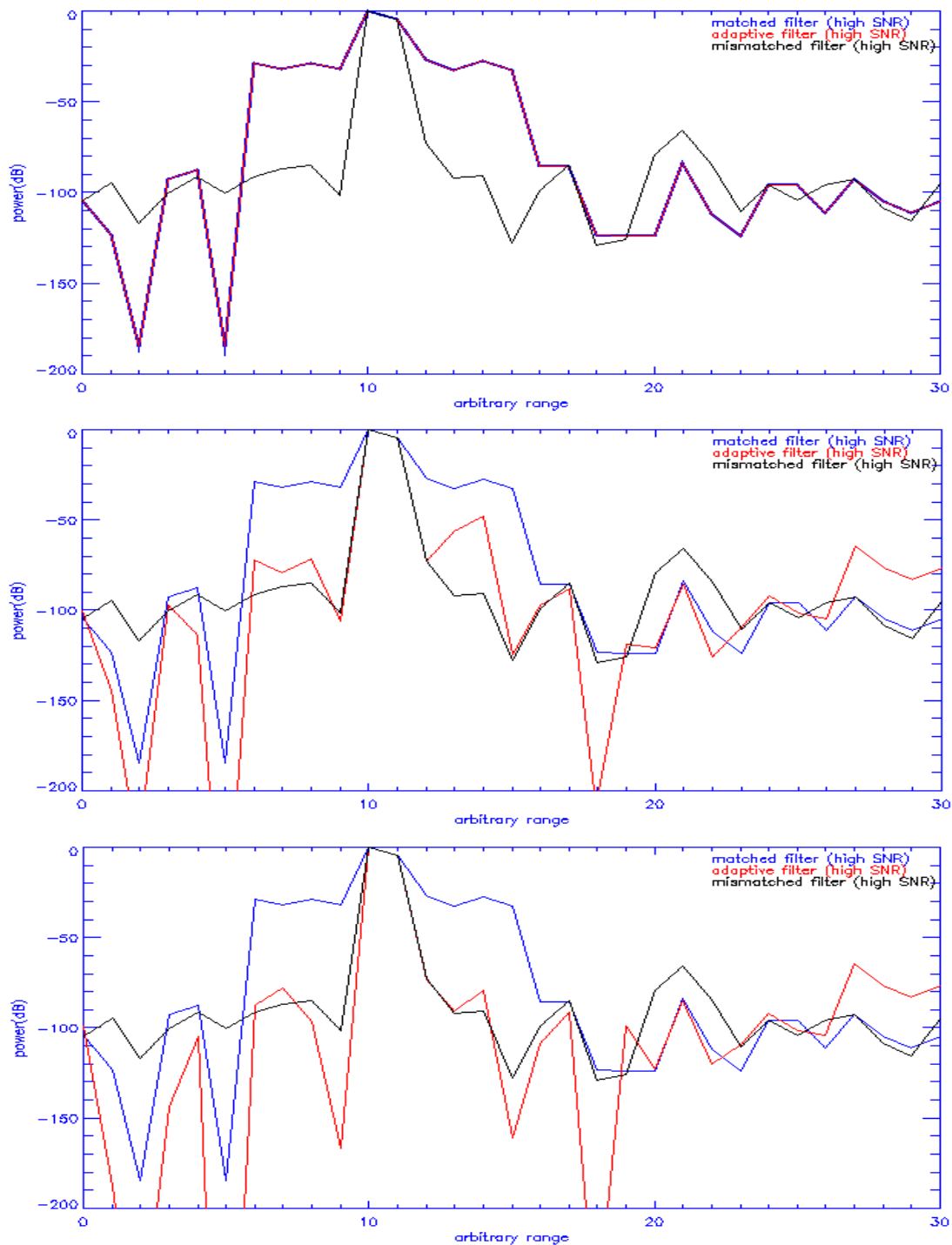
Figure 3.18: Comparison of matched, mismatched and adaptive filtering for a high SNR target. In 1st iteration (top plot) the adaptive filtering output is identical to matched filtering. As the iteration carries on, the adaptive filtering estimates and remove more noise and side lobe (2nd iteration-middle plot) and reaches optimum answer in the 3rd iteration (bottom plot).

Table 3.4 represents the MSE (Mean-Squared Error) comparison of the matched, mismatched an adaptive filtering for the first case study if the true target was a spike at range 10 with no side lobes. By the 5th iteration the adaptive filtering shows better performance over the other two methods by removing an additional 43 dB of the noise and side lobes.

Table 3.4: Comparison of side lobe suppression in terms of MMSE for matched, mismatched, and adaptive filtering.

Iteration	1	3	5
MSE-mismatch (dB)	-41.9156	-41.9156	-41.9156
MSE-match(dB)	-40.4732	-40.4732	-40.4732
MSE-adaptive (dB)	-40.0816	-50.1404	-93.2494

In this chapter, we studied two new filtering techniques in addition to the standard matched filtering. While the matched filtering technique results in optimum signal-to-noise ratio for the main lobe, it does not account for generation of side lobes. Mismatched filtering aims to remove these side lobes, however, degradation of the main lobe SNR is the cost. Adaptive filtering has superior performance compared to matched and mismatched filtering. It offers advantages of both methods by removing side lobes and optimal estimation of signal-to-noise ratio of the main lobe. However, it has more implementation complexity. Furthermore, depending on the size of the problem steps should be taken to deal with ill conditioned matrices involved in inversion. Depending on the application and the environment in which radar is operating, each method can be used in practice. For low SNR targets with sparse spatial distribution, matched filtering is practical. For high SNR targets with clutter in neighboring ranges, mismatched filtering offers more advantages in this case. If the target of interest has dense spatial distribution,

(i.e. targets are located next to each other.) and SNR is of importance, the adaptive filtering is the ideal approach to implement.

Chapter 4   SuperDARN Spectral Analysis

The FitACF algorithm employs time domain analysis on the ACF lag profile to measure Doppler velocity at each range. The Doppler velocity measurement becomes erroneous when the algorithm deals with noisy data, few number good lags and existence of multiple Doppler frequencies in the ACF lag profile. Frequency domain analysis, another approach to make the same measurements, is studied in this chapter. We examine the frequency domain analysis using Fourier-transform based methods such as, maximum entropy and Fast Fourier Transform on the ACF lag profile to obtain Doppler velocity. Power spectrum analysis is more robust and less prone to noise and missing lags. These can be listed as the main reasons of FitACF algorithm failure in measurement of the Doppler velocity in the ACF lag profile. However, the leakage and windowing effect in the spectral analysis makes the frequency components spread in the spectrum; thereby, measurement of the velocity, power and spectral width of the desired range is achievable with lower resolution. Moreover, after removing bad lags from the ACF lag profile, what we left with is the profile of the lags with non-uniformly spaced data. Since an unevenly sampled non-periodic signal is ambiguous, there is a problem of aliasing between true peaks with other peaks of different heights considering Fourier transform. The Lomb periodogram is another approach that overcomes the problem of non-uniformly sampled data. In this chapter, both time domain and the frequency domain analyses are applied to simulated and experimental cases to study the tradeoffs of each method.

4.1 Lomb Periodogram

The Lomb periodogram method provides estimates of signal parameters of a given frequency range by fitting sines and cosines to the data in a least square fashion and determining the correlation of data at each frequency [12]. Equation (4.1) represents the spectrum calculation of the signal $x(t)$ using the Lomb periodogram method, where $x(t)$ is sampled at times t_k $(k = 0,1,2, \dots, N - 1)$ and $w = 2\pi f$ [12]:

$$p(w) = \frac{\left\{\sum_{k=0}^{N-1} x(t_k)\cos\left[w(t_k-\tau)\right]\right\}^2}{\sum_{k=0}^{N-1}\cos^2\left[w(t_k-\tau)\right]} + \frac{\left\{\sum_{k=0}^{N-1} x(t_k)\sin\left[w(t_k-\tau)\right]\right\}^2}{\sum_{k=0}^{N-1}\sin^2\left[w(t_k-\tau)\right]}, \tag{4.1}$$

where:

$$\tan(2w\tau) = \frac{\sum_{k=0}^{N-1}\sin\left(2wt_k\right)}{\sum_{k=0}^{N-1}\cos\left(2wt_k\right)}. \tag{4.2}$$

Since the same value for w and $-w$ is squared, the spectrum is even. In case of a complex signal and asymmetric spectrum, equation (4.1) does not satisfy the general criteria and fails to extract Doppler frequency components for targets moving away from radar. Equation (4.3) takes into consideration the negative frequency components:

$$P(w) = \frac{\sum_{k=0}^{N-1} x(t_k)\cos\left[w(t_k-\tau)\right]}{\sqrt{\sum_{k=0}^{N-1}\cos^2\left[w(t_k-\tau)\right]}} + i\,\frac{\sum_{k=0}^{N-1} x(t_k)\sin\left[w(t_k-\tau)\right]}{\sqrt{\sum_{k=0}^{N-1}\sin^2\left[w(t_k-\tau)\right]}}. \tag{4.3}$$

4.2 Time Domain and Frequency Domain Velocity Measurements

In this section, robustness of time domain and frequency domain analysis to missing lags are evaluated. This is accomplished by comparing measurement of the Doppler velocity determined using an ACF lag profile and that determined using a power spectrum for a simulated case. The FitACF algorithm is employed to derive the Doppler velocity from ACF lag profile and we implement FFT and Lomb periodogram to make the same measurements using the power spectrum. A range profile with a moving point target of 130 Hz Doppler frequency is simulated, quadrature sampled and the auto-correlation function for 22 lags is obtained. The next step involves several stages. At each stage, a few lags are removed in a random fashion and three Doppler frequencies (using FitACF standard algorithm, FFT and Lomb periodogram) are calculated. Figure 4.1 shows measured and unwrapped phase profiles using the FITACF algorithm for each six stages. Figures 4.2 and 4.3 represent the spectral analysis results using Lomb and FFT methods.
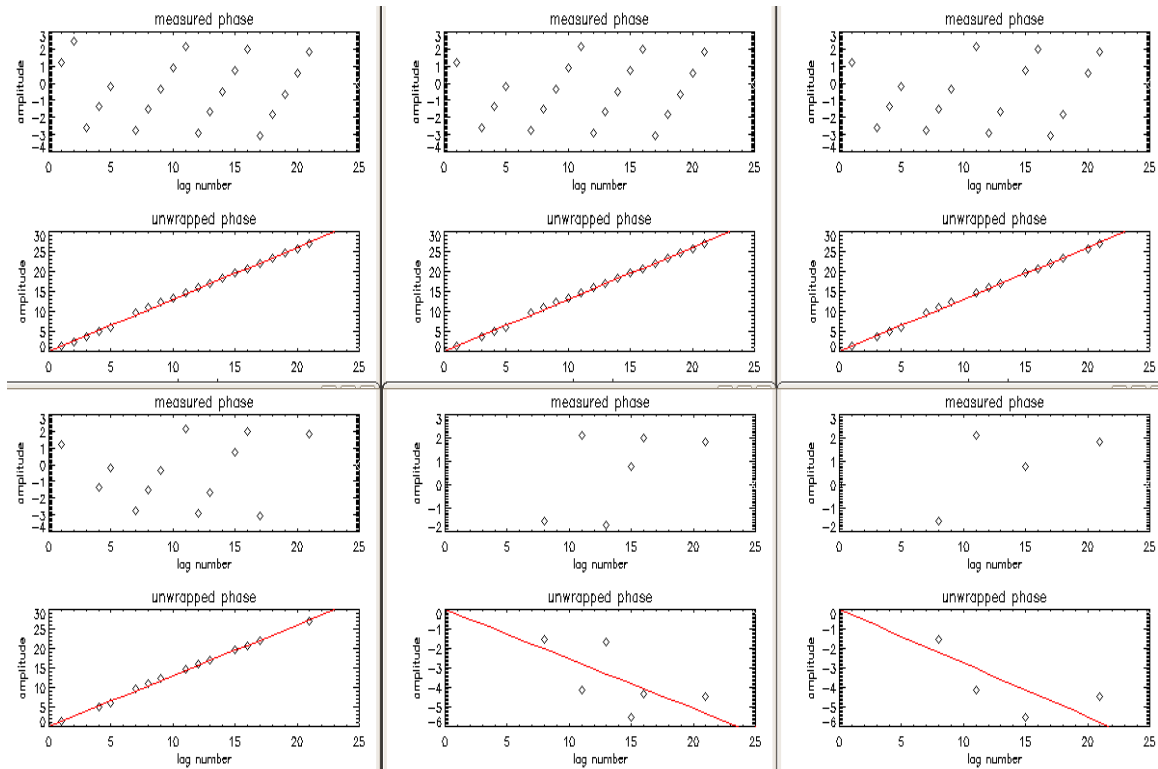
Figure 4.1: Performance of FITACF algorithm in measuring Doppler frequency at each stage. The top plot at each stage shows the number of remaining measured lags and the unwrapped phase profile is shown in the bottom plots. In the last two stages the phase unwrap algorithm fails to make correct measurement of the Doppler frequency.

In Figure 4.1 the FitACF algorithm fails to have a correct measurement of the Doppler frequency in stages five (bottom-middle) and six (bottom-right), where there are few lags left. Figures 4.2 and 4.3 represent the spectral analysis results. Even at stages five and six where the time domain analysis makes spurious measurements of Doppler velocity, Lomb periodogram and FFT still return the same value of measured velocity as in the previous stages.
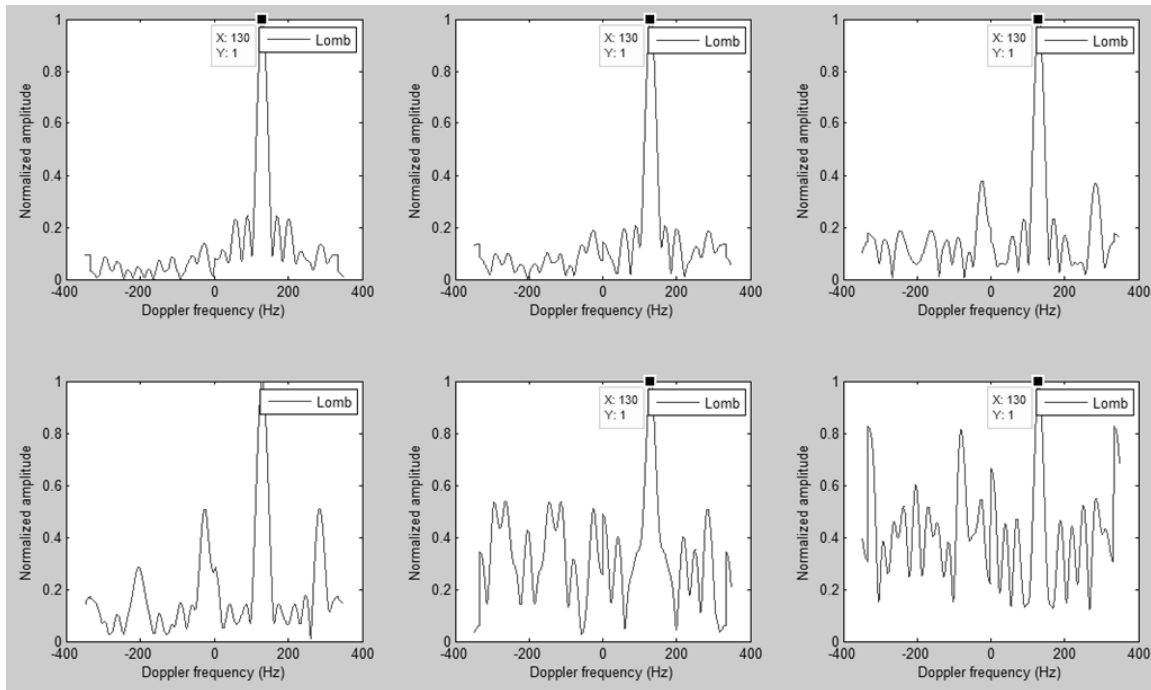
Figure 4.2: Performance of the Lomb periodogram in measuring the Doppler frequency. The peak of the normalized plot at each stage shows the Doppler frequency. The last two stages show successful measurement of the Doppler frequency.
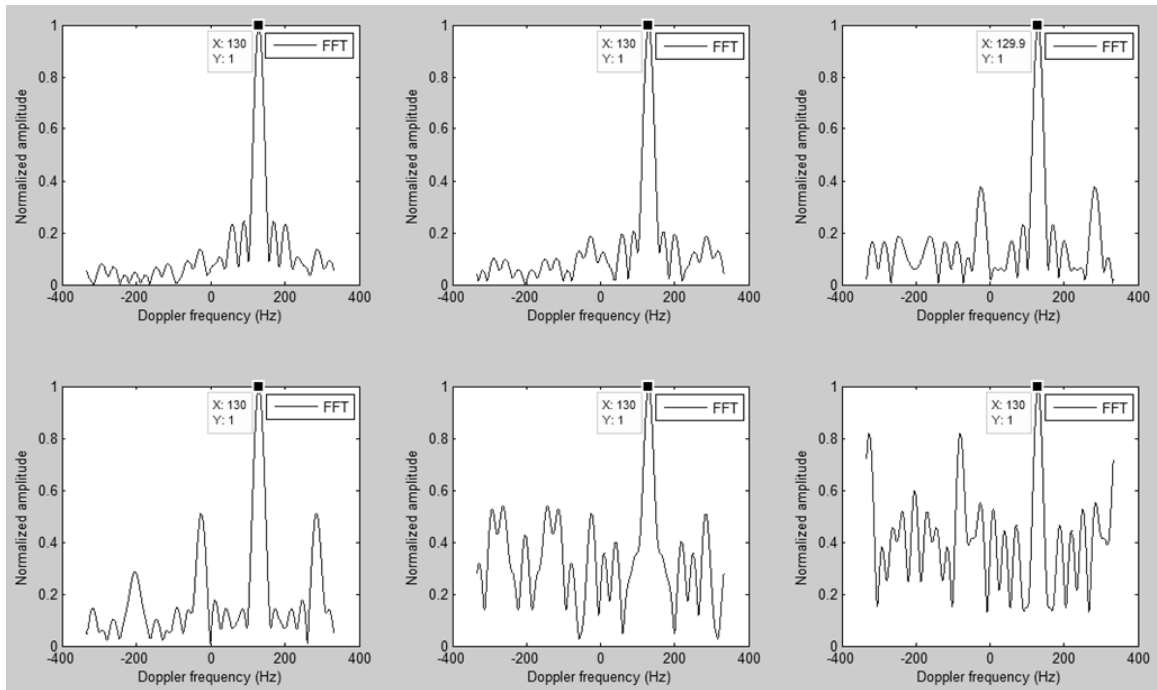
Figure 4.3: Performance of the FFT in measuring Doppler frequency at each stage. The peak of the normalized plot at each stage shows the Doppler frequency. The last two stages show successful measurement of the Doppler frequency.

The FitACF algorithm fails to measure the correct Doppler frequency of the simulated target at the last two stages, while the spectral analysis is more robust. In Figure 4.1 there are only 7 and 5 lags left in stages five and six. The FitACF phase unwrap algorithm, explained in section 2.7, estimates the preliminary Doppler frequency by measuring the slope of the consecutive good lags. There is only one pair left in stage 5 and nothing for the sixth stage. Furthermore, there are 7 missing lags between lag 0 and the next good lag in both plots. These make it impossible for the algorithm to unwrap and measure the Doppler frequency appropriately. Table 4.1 shows the measured Doppler frequency and number of remaining lags at each stage for each method.

Table 4.1: Comparison of the FitACF, Lomb, and FFT methods performance in measuring the Doppler frequency.

Number of remaining lags	FFT Doppler frequency (Hz)	Lomb Doppler frequency (Hz)	FitACF algorithm Doppler frequency (Hz)
21	130	130	130
20	130	130	130
17	130	130	130
14	130	130	130
7	130	130	-25.40
5	130	130	-27.51

4.3 Simulation and Experimental Results

In section 4.3., performance of the FitACF algorithm, Fourier transform and Lomb periodogram in measuring Doppler frequency of a moving target for different cases have been evaluated. In these examples, the target of interest has been contaminated with other moving targets, ground scatter and cross-range interference. In each case, the results are analyzed and the existing tradeoffs between each method are studied.

4.3.1 Case Study 1 (single target)

In this case, with the assumption of no cross-range noise, a Gaussian distributed target in range, centered at range 15 and width equal to 10 range gates with Doppler frequency of 100 Hz is created. The ACF and the corresponding phase profile are obtained, and the profile is analyzed using the FitACF algorithm, FFT and Lomb periodogram to calculate Doppler frequency. We compare the results for range 11 to determine how each method performs.
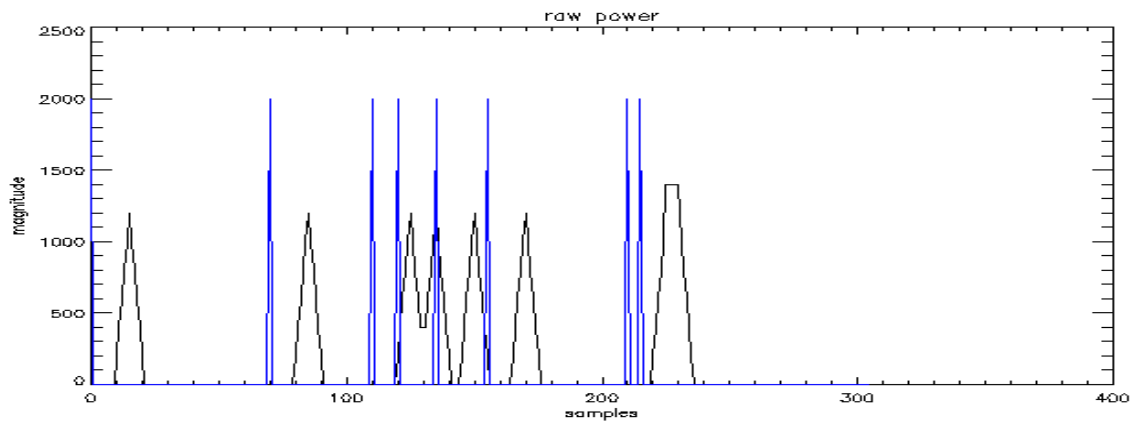
Figure 4.4: Simulated power profile for SuperDARN transmitted pulse sequence and received signal for distributed target with 100 Hz Doppler frequency.

Figure 4.4 illustrates power profile of the simulated data using the SuperDARN pulse sequence. Blue spikes show the transmitted pulse and the black plot illustrates the return power of the target. In-phase and quadrature samples are shown in Figure 4.5.
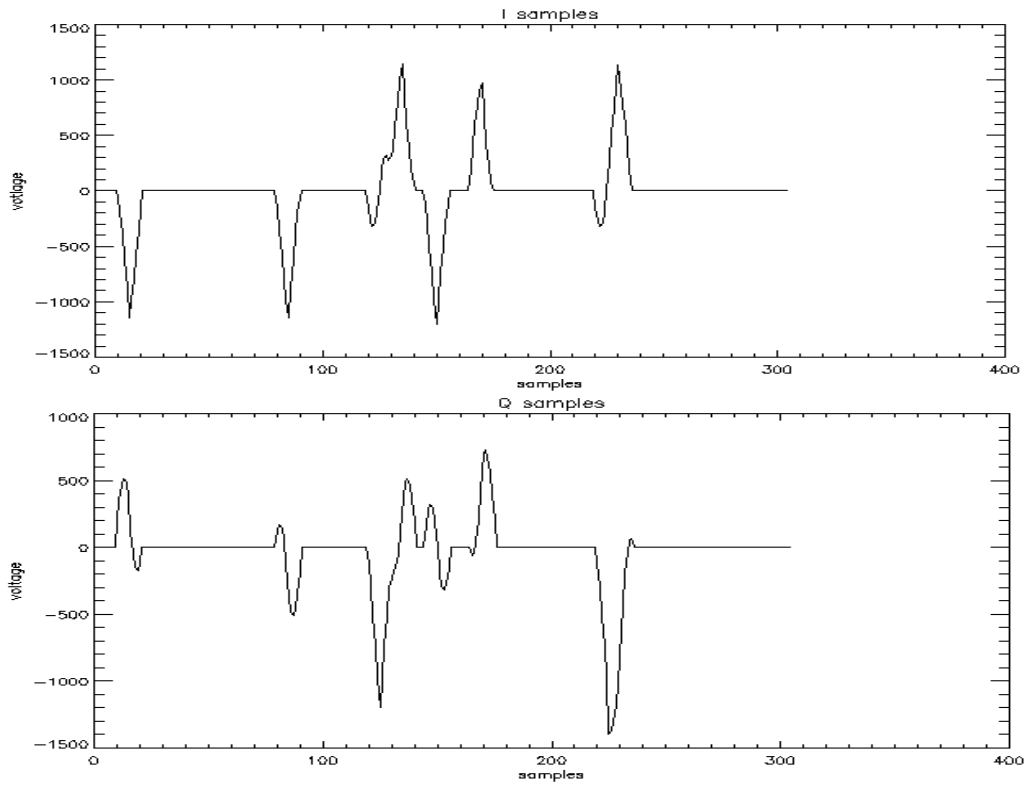
Figure 4.5: In-phase (top) and quadrature (bottom) samples for simulated power profile of a distributed target with 100 Hz Doppler frequency.

Figure 4.6 shows the measured phase profile without removing bad lags. Since there is no significant cross-range interference, the phase values in the profile follow the same slope with 2π jumps.
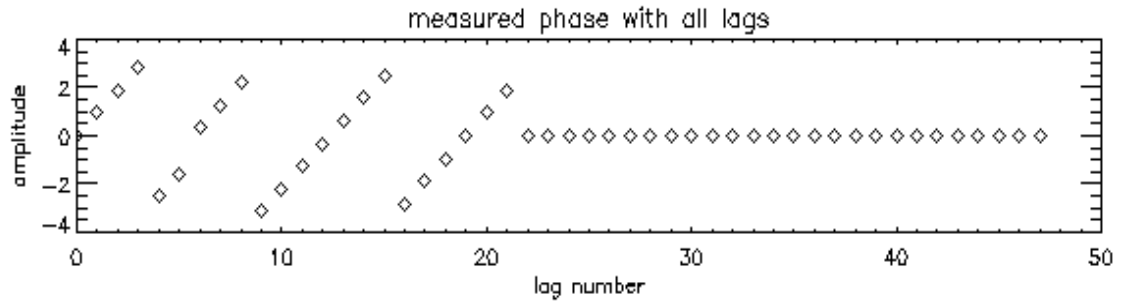
Figure 4.6: Measured phase profile for simulated target with 100 Hz Doppler frequency.

In this case, the return power of the target of interest in not contaminated with other targets. However, it is a distributed target and suffers from cross-range noise of neighboring ranges. In addition, Figure 4.4 shows that there are times that the received signal coincides with the transmitted signal, thereby the algorithm discards the samples, and the corresponding lags related to the TX-RX overlap. Figure 4.7 illustrates the measured (top plot) and the unwrapped phase (bottom plot) profiles after removing bad lags. In the bottom plot, despite removing a few lags from the lag profile, the algorithm is still successful in deriving the correct Doppler frequency of 100.0 Hz.
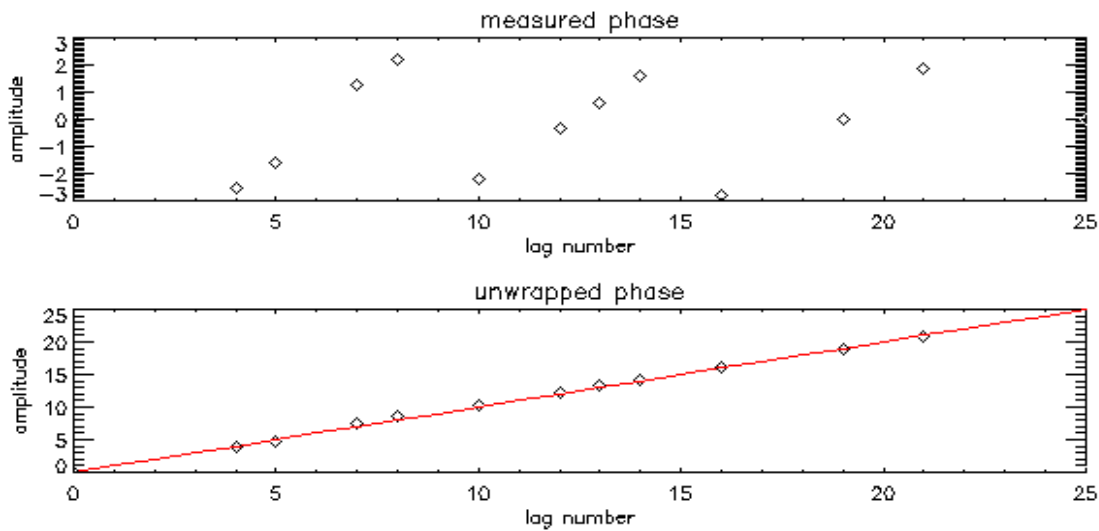
Figure 4.7: Measured and unwrapped phase profiles using FitACF algorithm for simulated distributed target with Doppler frequency of 100 Hz.

Spectral analysis results for the simulated data are shown in Figure 4.8. The top left plot shows the power spectrum using Lomb periodogram. 100.2 Hz is where the peak of the plot is located that corresponds to Doppler frequency of the simulated target. The top right plot shows the zoomed-in plot of the peak. Windowing effect results in peak width of about 0.32 Hz. This makes measurement of the Doppler frequency less accurate compared to time domain analysis. The bottom plot shows the FFT approach in measuring the Doppler frequency. The peak location (99.3 Hz) is shown on the left plot and the peak width (0.17 Hz) is illustrated in the right plot. The spectral analysis in this case does not show any advantage over the time domain and in fact, the time domain provides higher range resolution.
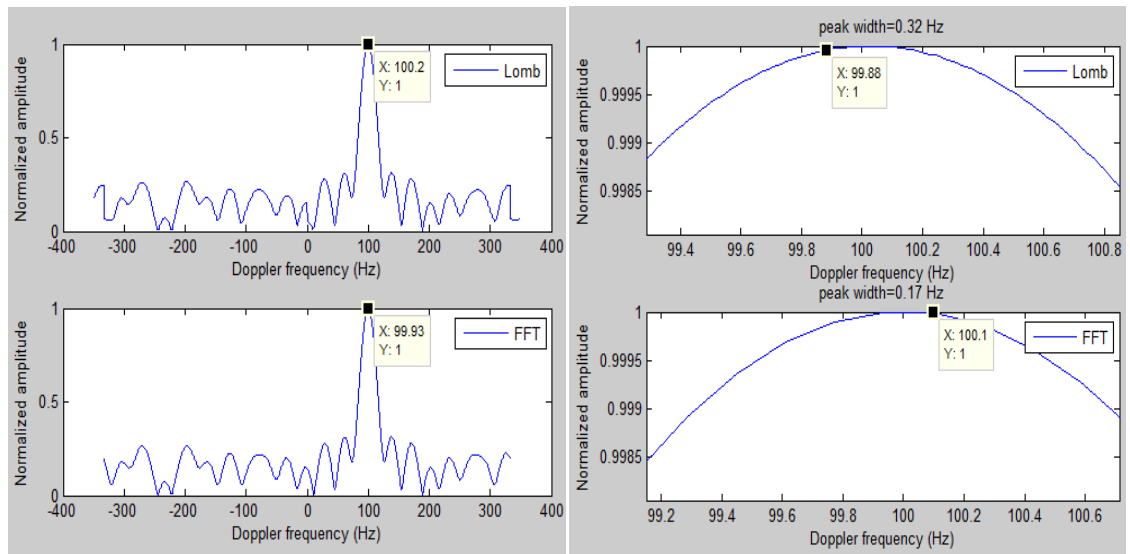
Figure 4.8: Velocity measurements of a simulated target with 100 Hz Doppler frequency using FFT (bottom-left) and LOMB (top-left) periodogram. The corresponding peak widths are shown on the right.

4.3.2 Case Study 2 (two targets with identical velocities)

In this case, two Gaussian distributed targets in range, centered at ranges 15 and 35 and widths of 10 range gates with 100 Hz Doppler frequency (ranges: 10-20 and 30-40) are created. The ACF and the corresponding phase profiles are calculated and the profiles are analyzed using the FitACF algorithm, FFT and Lomb periodogram to measure the Doppler frequency. We compare the results for range 11 to determine how each method performs.

82
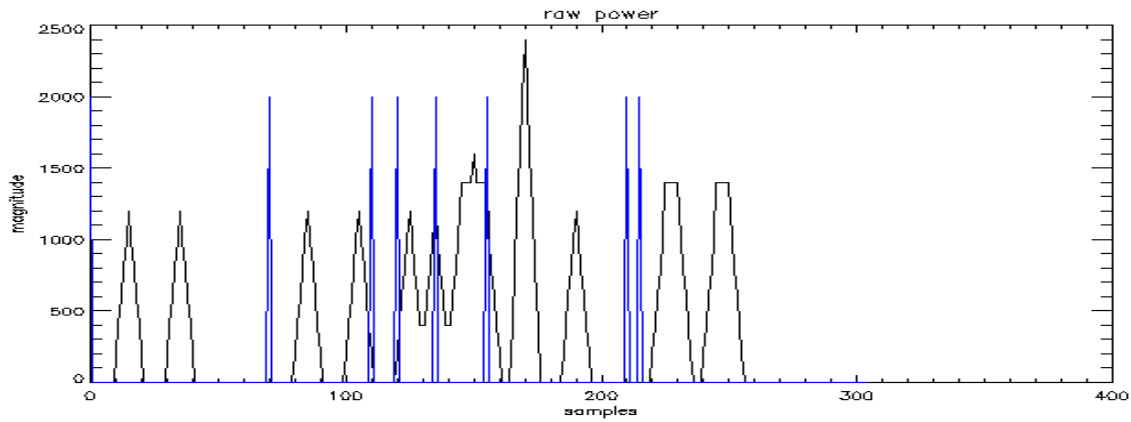
Figure 4.9: Simulated power profile for SuperDARN transmitted pulse sequence and received signal for two distributed targets with 100 Hz (range: 10-20) and 100 Hz (30-40) Doppler frequency.

Figure 4.9 shows power profile of the simulated target using the SuperDARN pulse sequence. Blue spikes show the transmitted pulse and the target return power is illustrated in black. In-phase and quadrature samples are plotted in Figure 4.10.
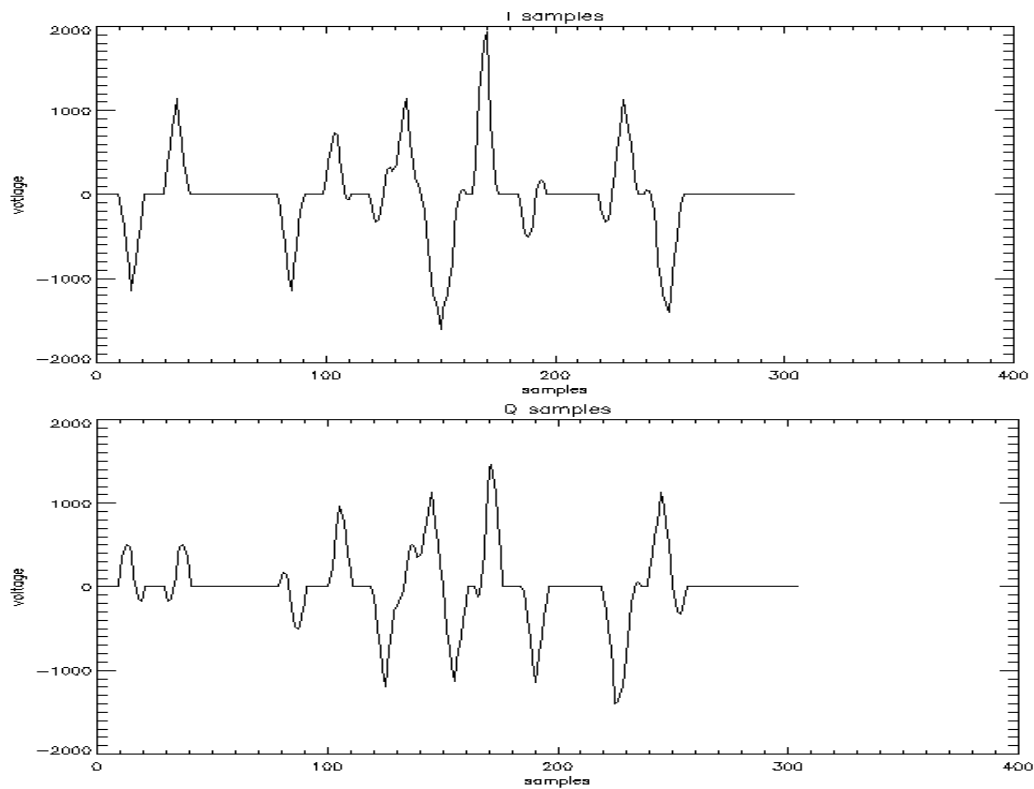
Figure 4.10: In-phase (top) and quadrature (bottom) samples for simulated power profile of two distributed targets with 100 Hz Doppler frequency.

Figure 4.11 shows the measured phase profile without removing bad lags. Since the interfering target and the target of interest have identical velocities, phase measurements does not reveal significant changes in the phase profile compared to the previous case.
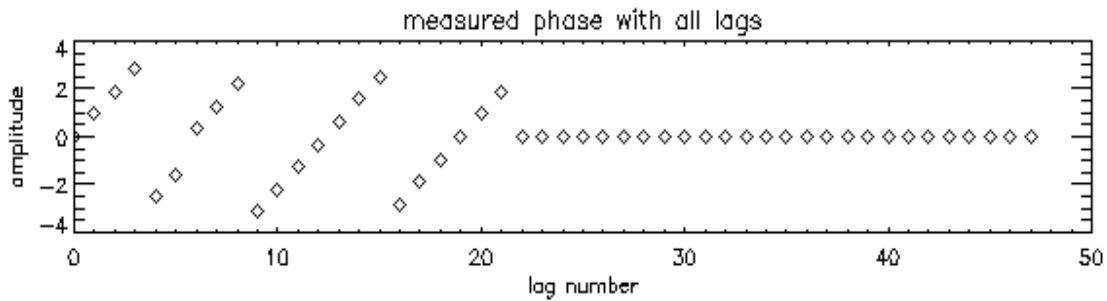
Figure 4.11: Measured phase profile with all lags for a distributed target with 100 Hz Doppler frequency contaminated with another target of same Doppler velocity.

Figure 4.12 shows the measured and unwrapped phase profiles after removal of bad lags. In this Figure, the Doppler frequency estimated using time domain analysis is -10.5 Hz for simulated targets with 100 Hz Doppler frequency. Although Figure 4.12 shows that the phase profile follows the same pattern as the first case study, several lags had to be removed because of the cross-range interference. Thereby, the insufficient number of remaining lags and their sparse distribution results in failure of the FitACF algorithm to unwrap correctly in measuring the Doppler frequency.
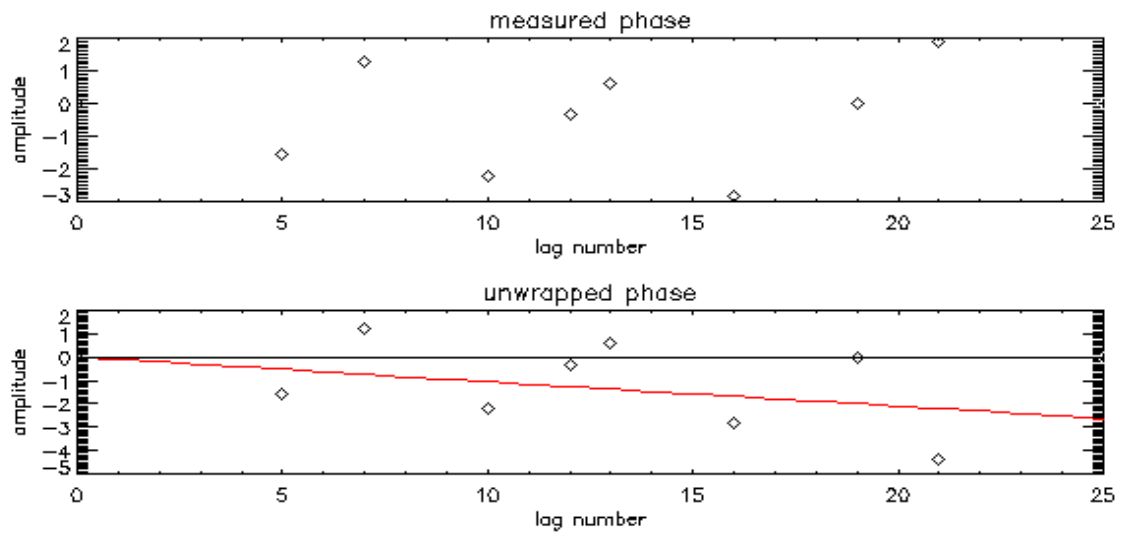
Figure 4.12: Measured and unwrapped phase profiles using FitACF algorithm for a distributed targets with 100 Hz Doppler frequency contaminated with another target of same Doppler velocity.

Spectral analysis results are shown in Figure 4.13. The top left plot shows the power spectrum using Lomb periodogram. Peak of the plot is located at 99.88 Hz that corresponds to Doppler frequency of the simulated target. In top right plot of Figure 4.13 the peak width is about 0.32 Hz. This makes the Doppler frequency measurement less accurate compared to the time domain analysis. The bottom plot shows the FFT approach in measuring the Doppler frequency. The peak location (100.1 Hz) is shown on the left plot and the peak width (0.19 Hz) on the right. The associated peak widths in the spectral analysis make the uncertainty in the Doppler frequency measurement higher, but this case study shows where the FitACF algorithm fails, the spectral analysis outperforms.
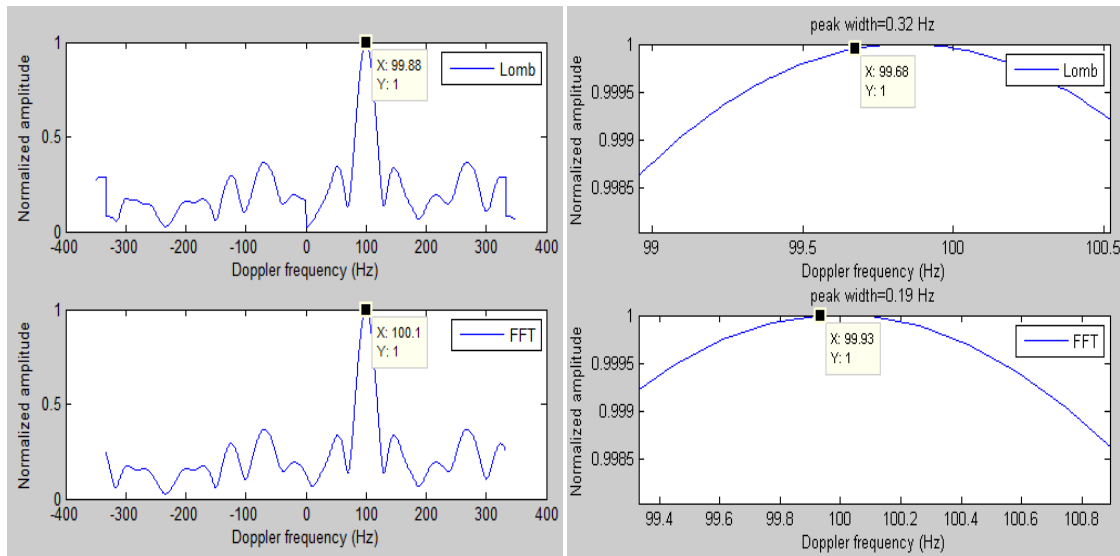
Figure 4.13: Measured Doppler frequency using LOMB priodogram (top) and FFT (bottom) for a distributed target with 100 Hz Doppler frequency contaminated with another target of same Doppler velocity. The corresponding peak widths are shown on the right plots.

4.3.3 Case Study 3 (Two targets with dissimilar velocities in different ranges)

In this case, two Gaussian distributed targets in range, centered at ranges 15 and 35, widths equal to 10 range gates with 100 Hz (ranges: 10-20) and 10 Hz (ranges: 30-40) Doppler frequencies are created. The ACF and the corresponding phase profile are calculated and the profile is analyzed using the FitACF algorithm, FFT and Lomb periodogram to calculate the Doppler frequency. We compare the results for range 10 to determine how each method performs.
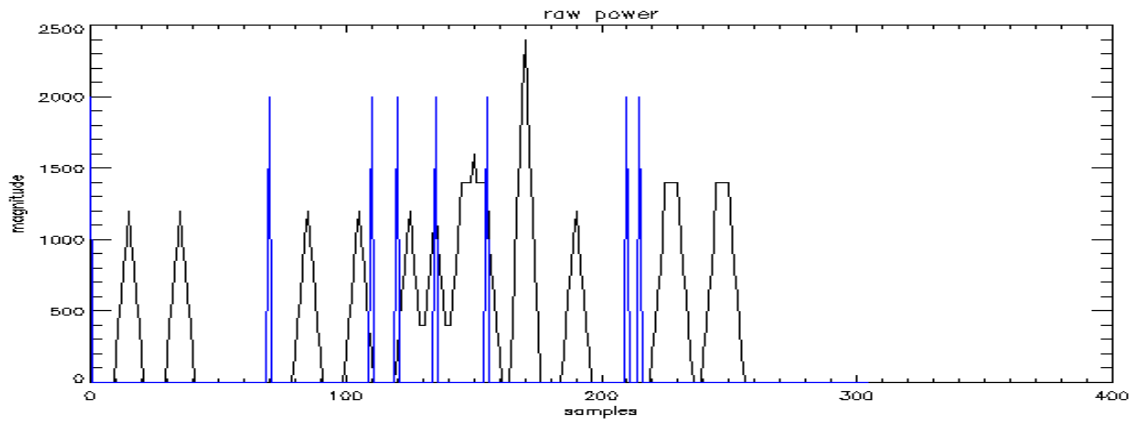
Figure 4.14: Simulated power profile for SuperDARN transmitted pulse sequence and received signal for two distributed targets with 100 Hz (range: 10-20) and 10 Hz (30-40) Doppler frequency.

Figure 4.14 illustrates the power profile for simulated targets using the SuperDARN pulse sequence. Blue spikes show the transmitted pulse and the target return power is illustrated in black. In Figure 4.15, in-phase and quadrature samples of the target located at range 10-20 have higher variations, thereby higher Doppler frequency compared to the same profile in range 30-40.
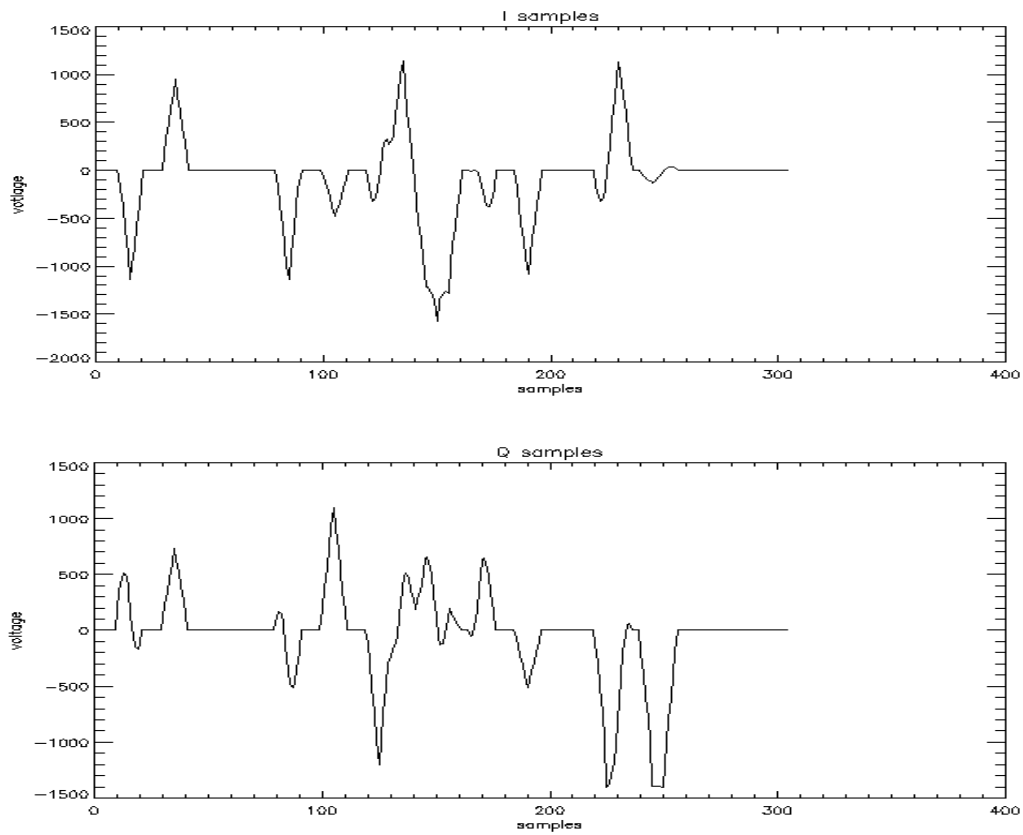
Figure 4.15: In-phase (top) and quadrature (bottom) samples for simulated power profile of two distributed targets with 100 Hz and 10 Hz Doppler frequency.

Figure 4.16 shows the measured phase before removing bad lags. Since the interfering target has different velocity from the target of interest, phase measurements reveal significant changes in the phase profile compared to the previous case.
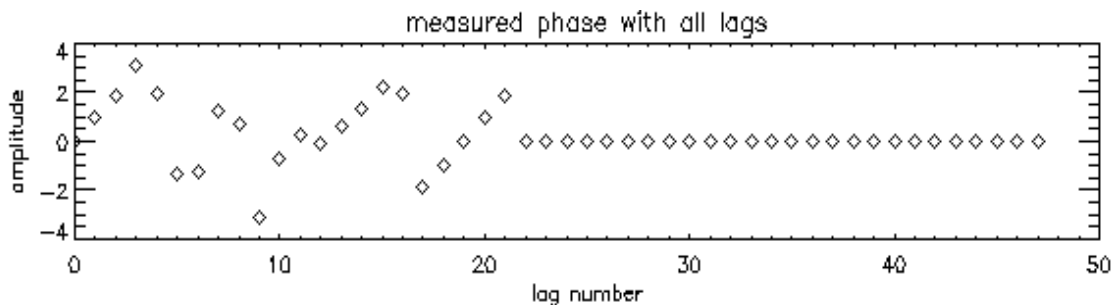
Figure 4.16: Measured phase profile with all lags for a distributed target with 100 Hz Doppler frequency contaminated with another target with 10 Hz Doppler frequency.

The distributed target of interest suffers from cross-range noise and bad samples related to the TX-RX overlap. Figure 4.17 shows the measured and unwrapped phase profiles after removing bad lags. The measured Doppler frequency using time domain analysis is 8.65 Hz for the simulated target with 100 Hz Doppler frequency. Comparing to the second case study (4.3.2), the phase profile doesn't follow the same pattern due to the cross-range interference. Furthermore, the sparse distribution of the remaining lags results in failure of the FitACF algorithm to measure the Doppler frequency correctly.
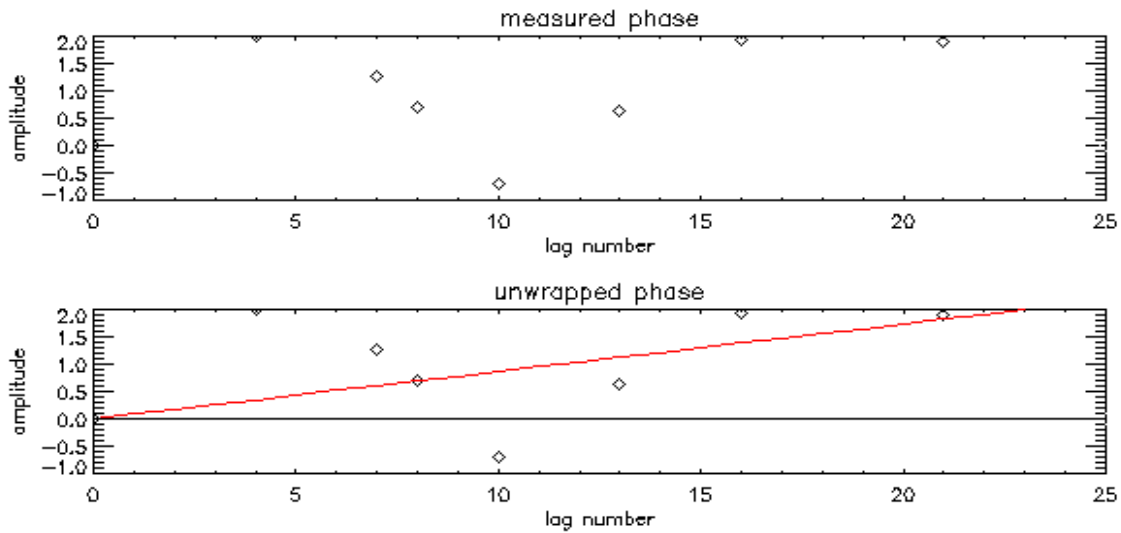
Figure 4.17: Measured and unwrapped phase profiles using FitACF algorithm for a distributed targets with 100 Hz Doppler frequency contaminated with another target with 10 Hz Doppler frequency.

Spectral analysis results for simulated targets are shown in Figure 4.18. The top left plot shows the power spectrum using Lomb periodogram. The peak of the plot is located at 98.51 Hz that corresponds to Doppler frequency of the simulated target. In top right plot of Figure 4.18 the peak width is about 0.29 Hz. This makes the Doppler frequency measurement less accurate compared to time domain analysis. In bottom plot on the left the peak of the calculated spectrum, using FFT is located at 98.8 Hz. There is a peak width of about 0.3 Hz, which makes the uncertainty in Doppler frequency calculation higher, but where the FitACF algorithm fails, the spectral analysis outperforms in measuring the Doppler frequency.
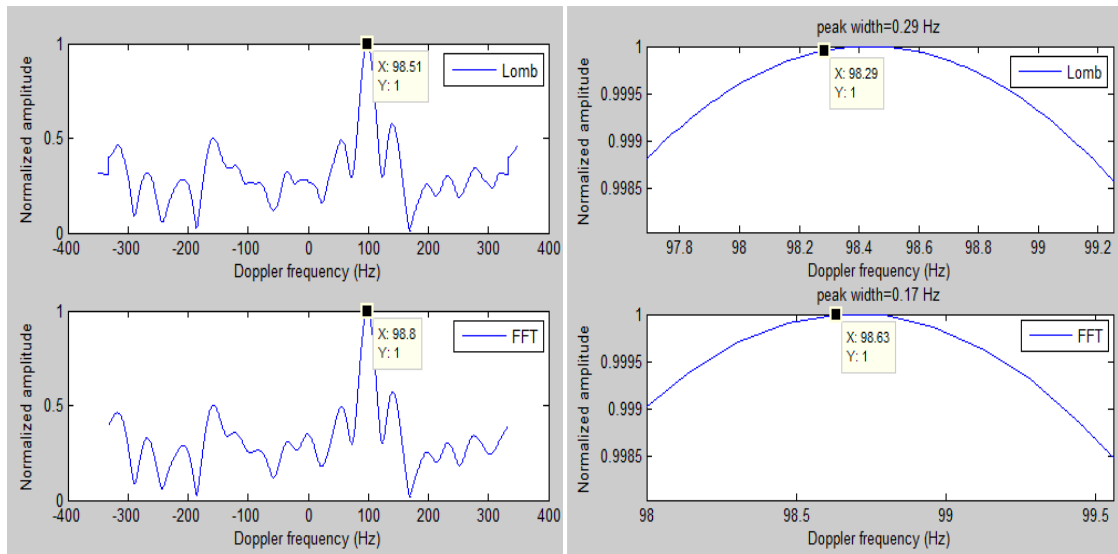
Figure 4.18: Measured Doppler frequency using LOMB priodogram (top) and FFT (bottom) for a distributed target with 100 Hz Doppler frequency contaminated with another target with 10 Hz Doppler frequency. The corresponding peak widths are shown on the right plots.

4.3.4 Case Study 4 (Two targets with unequal velocities in the same range)

In this case, two Gaussian distributed targets in range, centered at range 10 and width of 10 range gates with similar power profiles at 100 Hz (ranges: 10-20) and -150 Hz (ranges: 10-20) Doppler frequencies are created. The ACF and the corresponding phase profiles are calculated and the profiles are analyzed using the FitACF algorithm, FFT, and Lomb periodogram to calculate the Doppler frequency. The results for range 10 are shown to find out how each method performs. As expected, since the phase unwrap algorithm assumes there should be only a single Doppler frequency in each ACF profile, it fails to extract the correct Doppler frequency when there is more than one frequency component in the range profile.
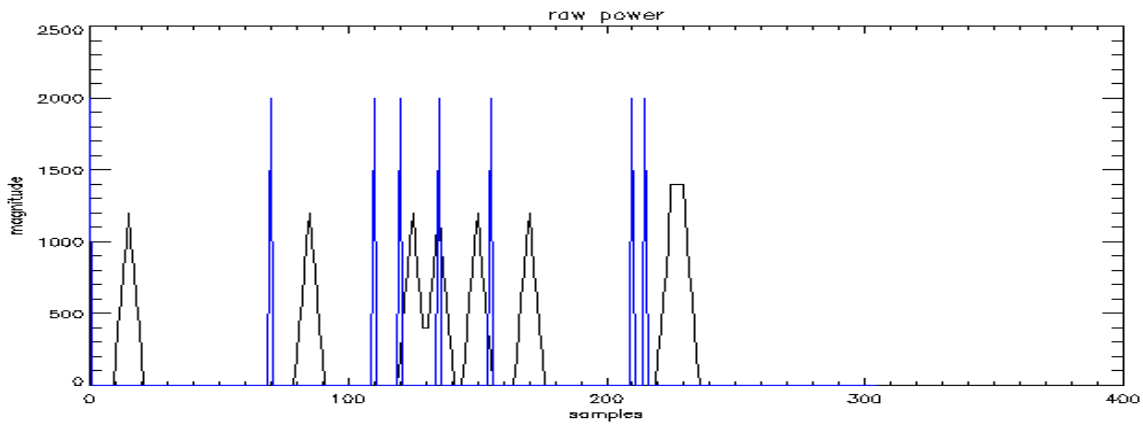
Figure 4.19: Simulated power profile for SuperDARN transmitted pulse sequence and received signal for two distributed targets with -150 Hz (range: 10-20) and 100 Hz (10-20) Doppler frequency.

Figure 4.19 illustrates power profile for the simulated target using the SuperDARN pulse sequence. Blue spikes show the transmitted pulse and the target return power is shown in black. In-phase and quadrature samples are illustrated in Figure 4.20.
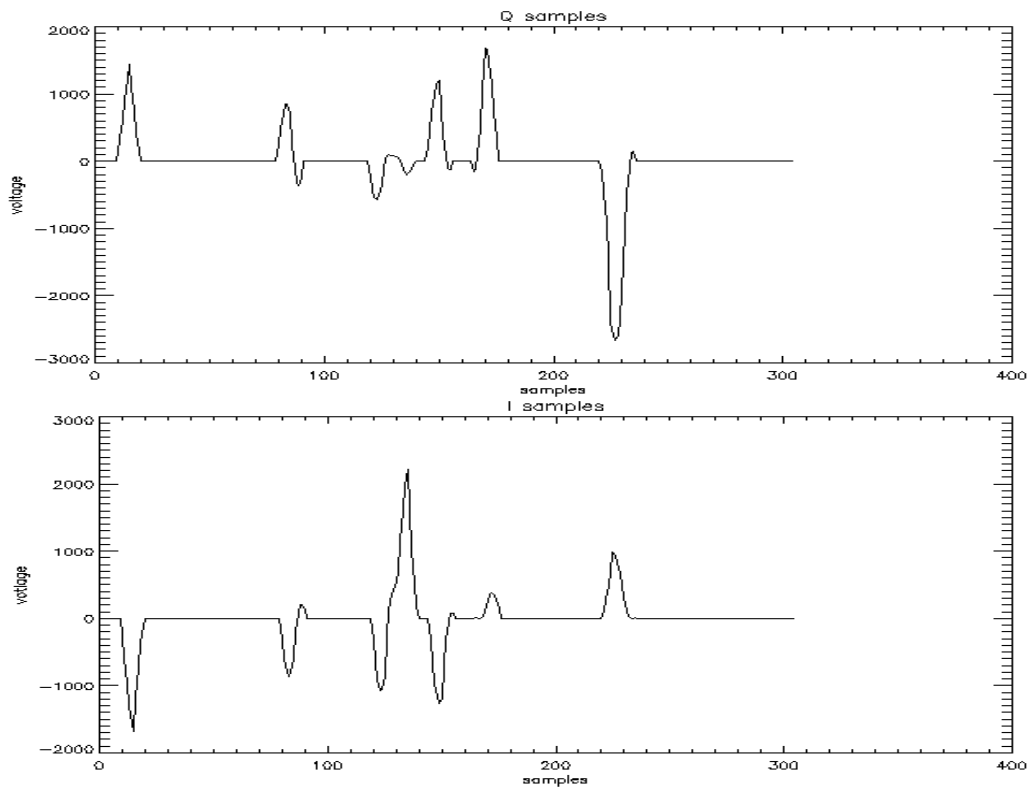
Figure 4.20: In-phase and quadrature samples of the received power profile for two
simulated targets with 100 Hz and -150 Hz Doppler frequency.

Figure 4.21 represents the measured phase profile before removing bad lags. The

negative slope of the profile suggests that -150 Hz is the dominant frequency.
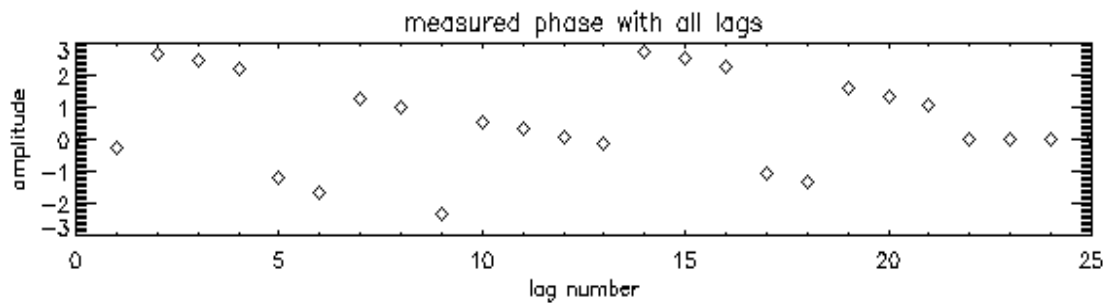
Figure 4.21: Measured phase profile with all lags for two simulated targets with 100 Hz
and -150 Hz Doppler frequency.

The distributed target of interest suffers from cross-range noise and bad samples related to the TX-RX overlap. Figure 4.22 shows the measured and unwrapped phase profiles after removing bad lags. The measured Doppler frequency using time domain analysis is 70.24 Hz for the simulated profile with 100 Hz and -150 Hz Doppler frequencies. In Figure 4.22, there are only seven lags left which makes it impossible for the FitACF algorithm to unwrap correctly and calculate the frequencies.
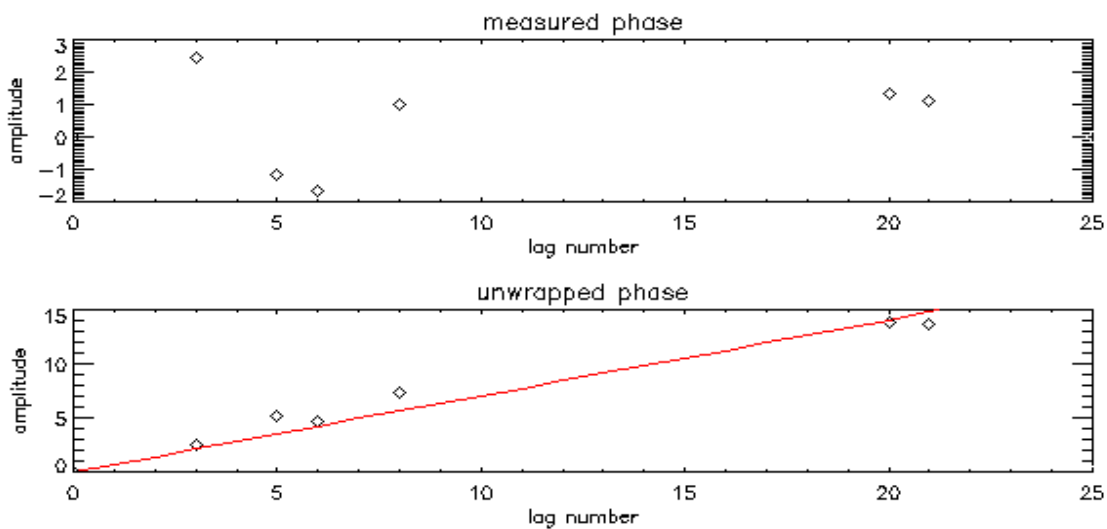
Figure 4.22: Measured and unwrapped phase profiles using the FitACF algorithm for two simulated targets with 100 Hz and -150 Hz Doppler frequency.

In Figure 4.23, spectral analysis results are shown for simulated targets. Top plot shows the power spectrum using Lomb periodogram. There are two peaks at -148.7 Hz and 97.91 Hz. In bottom plot in Figure 4.23 calculated power spectrum using FFT shows two peaks at -148.1 Hz and 97.98 Hz. Although, neither of the methods measures exact

Doppler frequency, spectral analysis extracts two Doppler frequencies close to the simulated profile velocities where the FitACF algorithm fails.
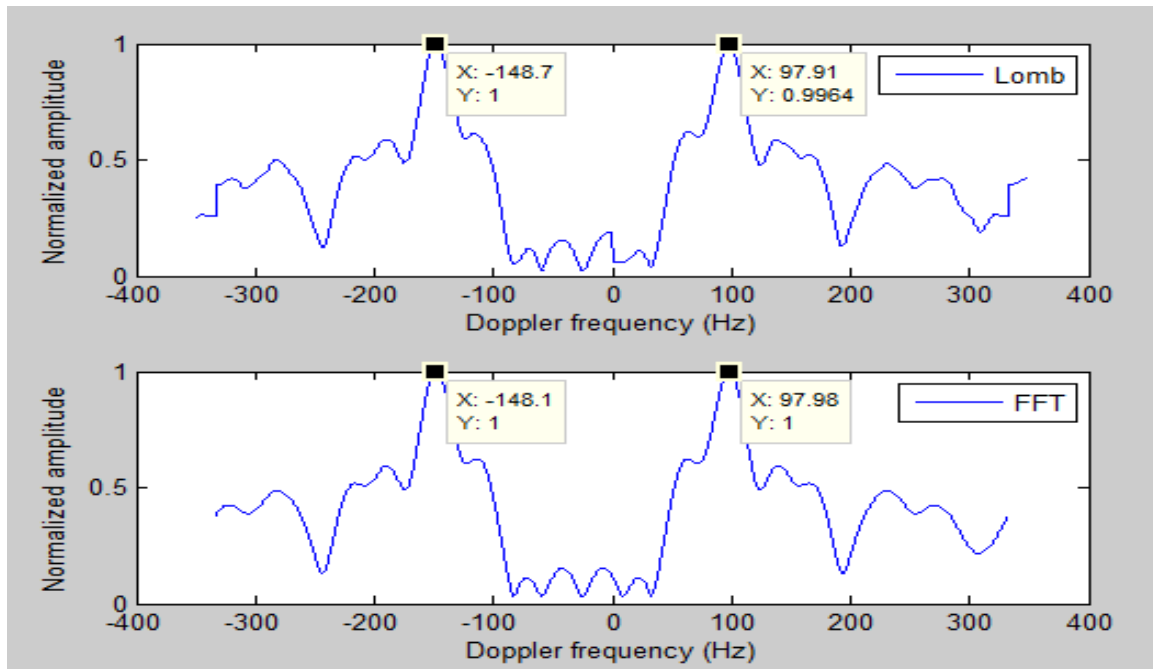
Figure 4.23: Illustration of the measured Doppler frequency using FFT and LOMB periodogram for two simulated targets with Doppler frequencies of 100 Hz and -150 Hz with all lags.

4.3.5 Case Study 5 (single target contaminated with ground scatter)

In this case, one distributed target in range centered at range 15, width of 10 range gates and 30 Hz (ranges: 10-20) Doppler frequency along with one Gaussian distributed ground scatter with the same power profile centered at range 15, width equals to 10 range gates and 0 Hz (ranges: 10-20) Doppler frequency are created. The ACF and the corresponding phase profiles are calculated and the profile is analyzed using the FitACF algorithm, FFT and Lomb periodogram to calculate Doppler frequency. We compare the results for range 15 to evaluate how each method performs.
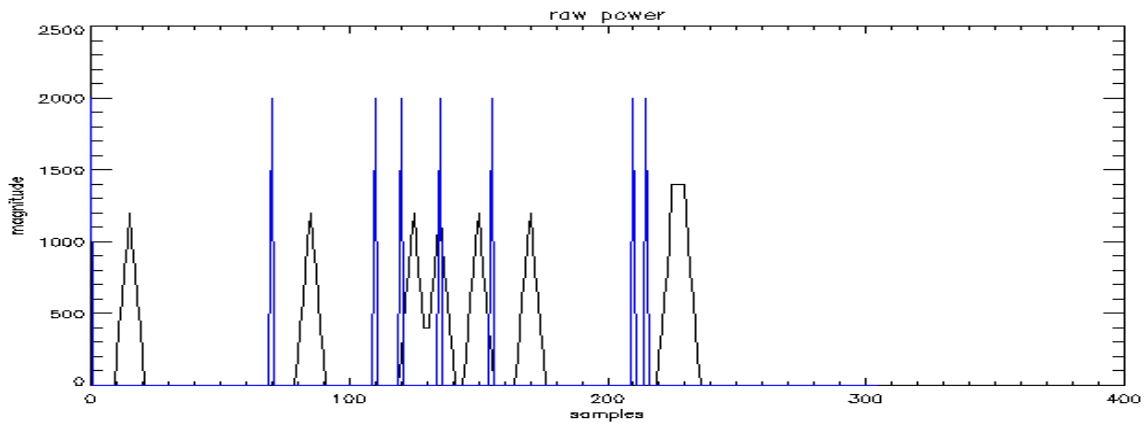
Figure 4.24: Simulated power profile for SuperDARN transmitted pulse sequence and received signal for a distributed target with 30 Hz (range: 10-20) Doppler frequency mixed with ground scatter (range: 10-20).

Figure 4.24 shows power profile for the simulated target using the SuperDARN pulse sequence. Blue spikes show the transmitted pulse and the target return power is shown in black. In-phase and quadrature samples are shown in Figure 4.25.
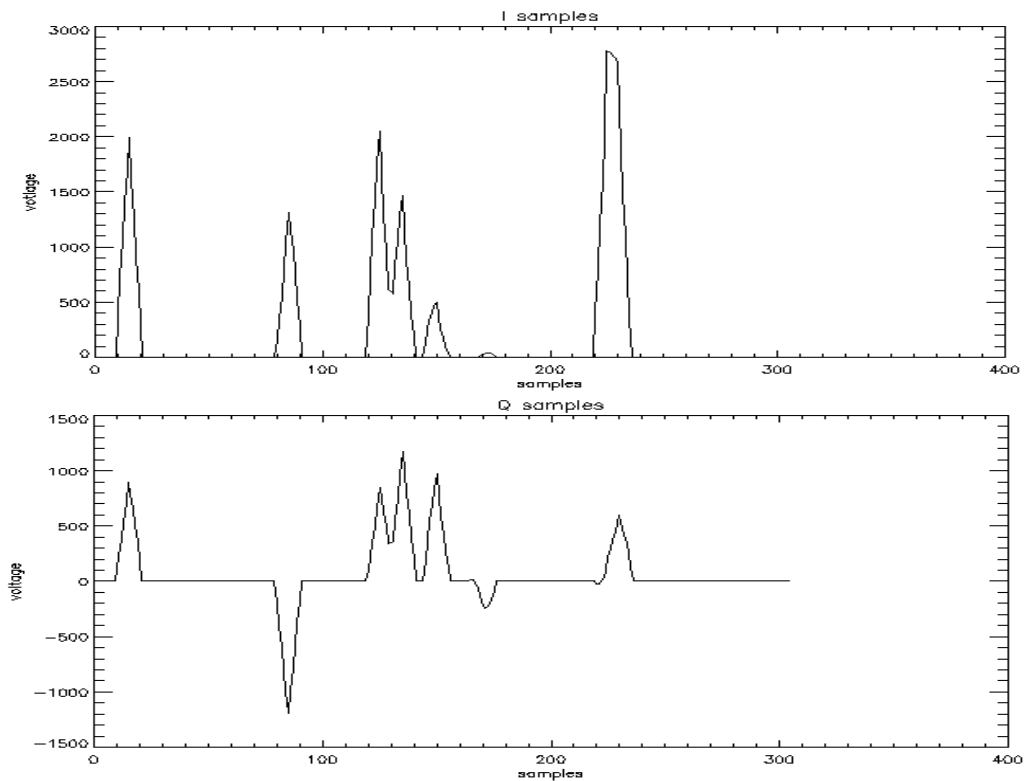
Figure 4.25: In-phase and quadrature samples of the received power profile for a simulated target with 30 Hz Doppler frequency contaminated with ground scatter.

Figure 4.26 illustrates the measured phase profile before removing bad lags. In this plot, the measured phase profile indicates only a single frequency component, however, some of the phase values fall outside of the line slope, which suggests effects of the ground scatter.
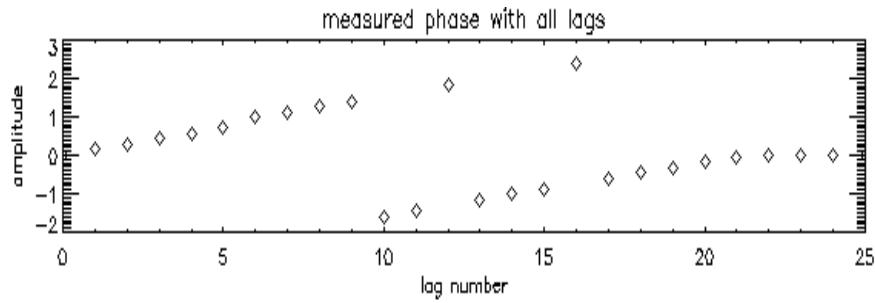
Figure 4.26: Measured phase profile with all lags for a simulated target with 30 Hz
Doppler frequency contaminated with the ground scatter.

Measured Doppler frequency using time domain analysis in Figure 4.27 is -0.689
Hz. This is in discrepancy with simulated profile with 30 Hz Doppler frequency and can
be explained by comparing Figures 4.26 and 4.27. Despite having small deviation from
line slope in Figure 4.26, sparse distribution of measurements in Figure 4.27 leads to
failure of the FitACF algorithm.
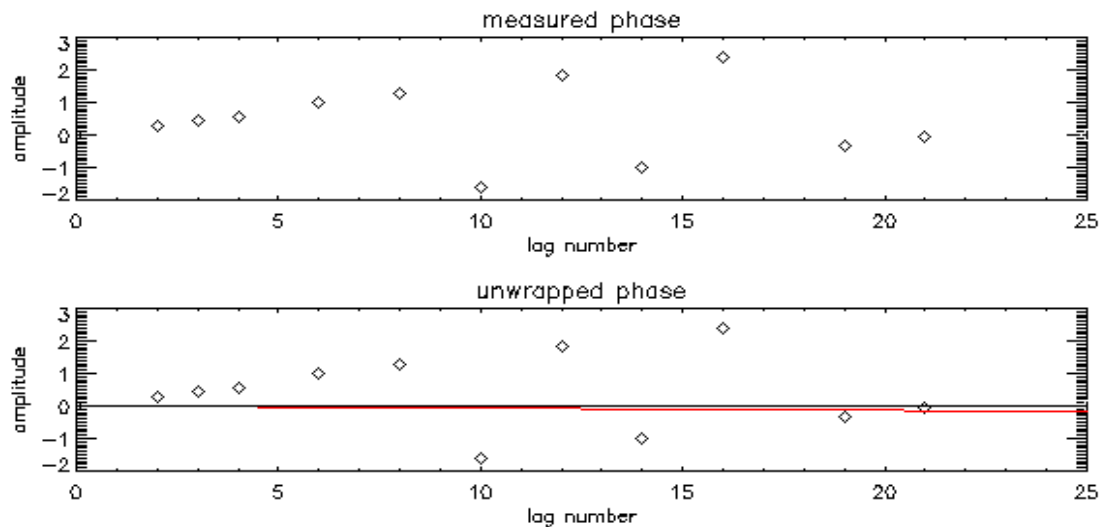
Figure 4.27: Measured and unwrapped phase profiles after bad lag removal using the
FitACF algorithm for a simulated target with 30 Hz Doppler frequency contaminated
with the ground scatter.

In Figure 4.28, normalized power spectrum using Lomb periodogram shows two peaks closest to one. The first peak at -0.0148 Hz corresponds to velocity of the ground scatter and 32.57 Hz for the moving target. The bottom plot shows FFT output, where the location of the two peaks is at -3.58 Hz for ground scatter and 33.53 Hz for moving target. The Lomb periodogram in this case outperforms over FFT approach, in measuring both the moving target and the ground scatter velocities.
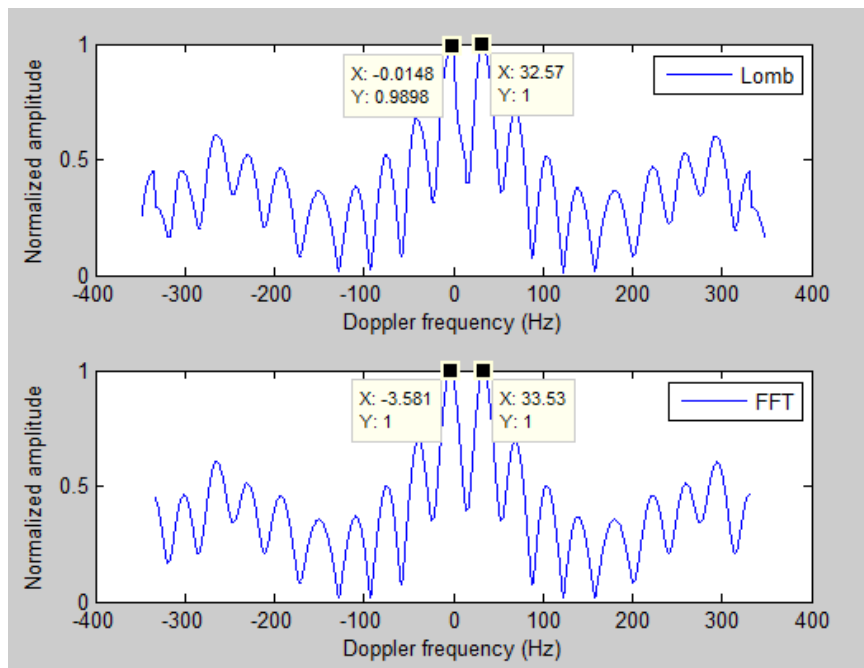
Figure 4.28: Measured Doppler frequerncy using FFT and LOMB periodogram for a simulated target with 30 Hz Doppler frequency contaminated with the ground scatter with all lags.

Figure 4.29 shows the zoomed-in plot of the peak where the moving target is located. Although there is a nominal difference in measured Doppler frequencies in Figure 4.29, if converted to Doppler velocity, it can reveal significant difference. For

example for a transmitted frequency of 10.665 MHz the converted velocity for 32.57 Hz Doppler frequency equals 458.08 m/s, while the 33.53 Hz Doppler frequency results in 471.58 m/s velocity.
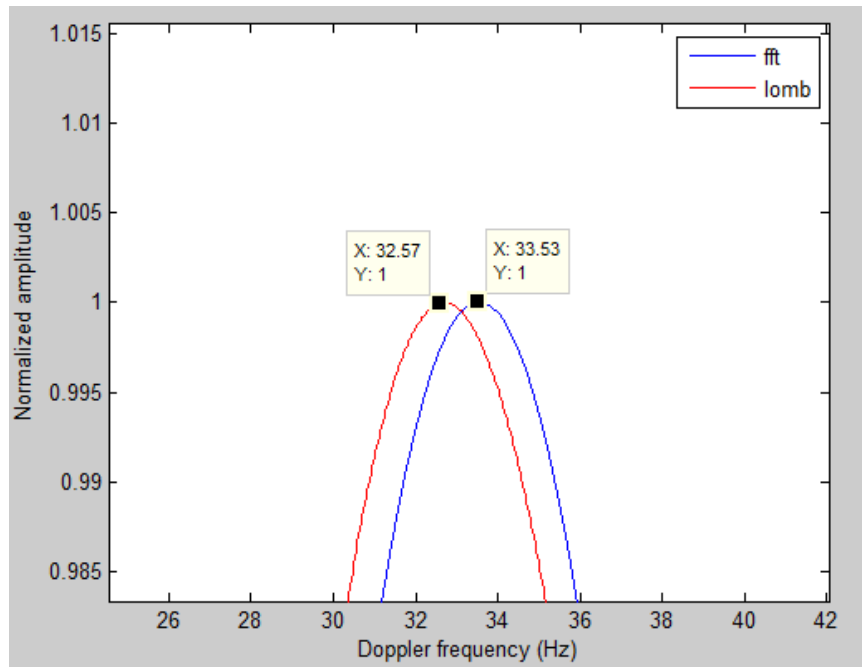
Figure 4.29: Illustration of the difference between FFT and Lomb periodogram in measuring the Doppler frequency for a simulated target with 30 Hz Doppler frequency contaminated with ground scatter.

4.3.6 Case Study 6 (Observation)

The case shows performance of the FitACF phase unwrap algorithm and spectral analysis in measuring the Doppler frequnecy for data taken from McMurdo radar at 4 UT (Universal Time) on 07/22/2010. The RTI (range-time-intensity) plot of the power, Doppler velocity, and spectral width is shown in Figure 4.30. The black arrow in this figure shows the location of the target (range: 28) for this case study.
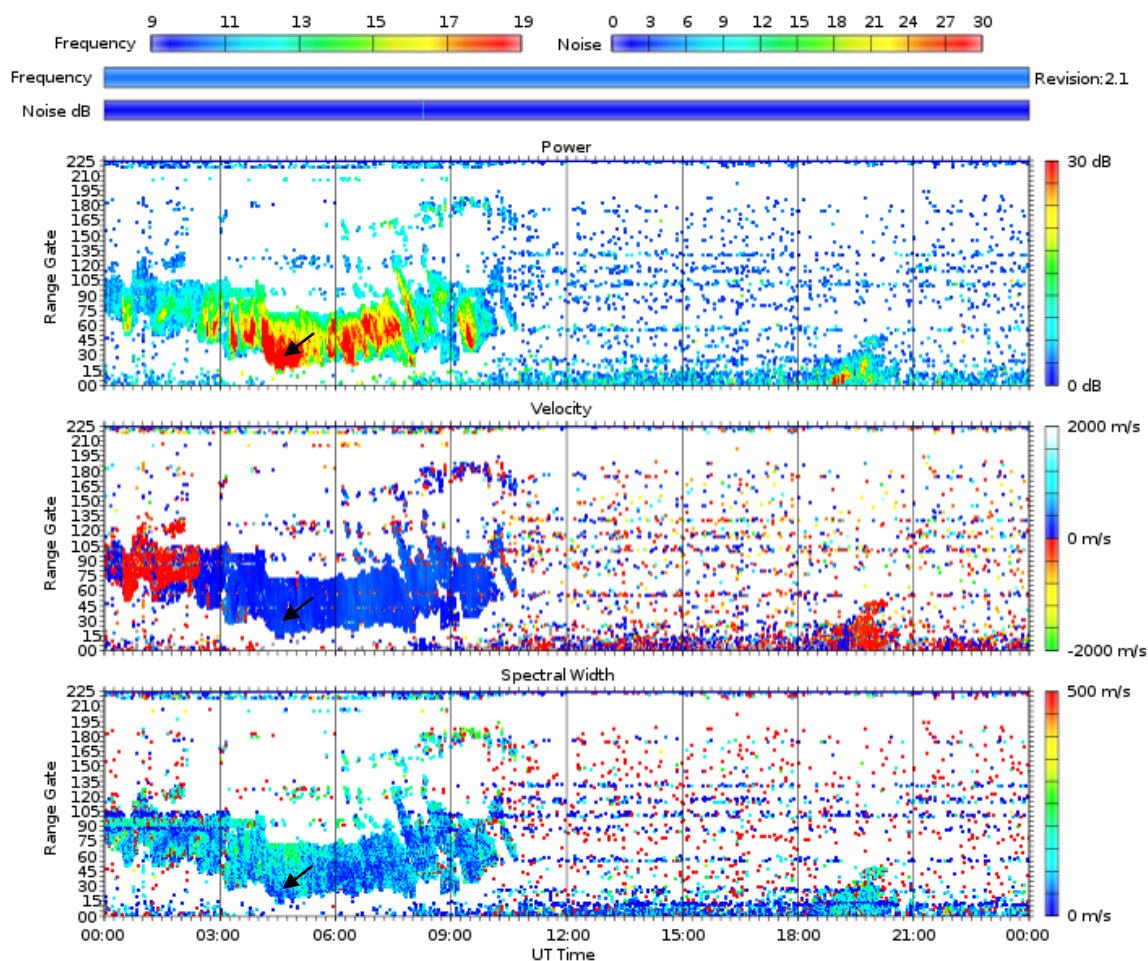
Figure 4.30: Range-time intensity plot showing power (top plot), velocity (middle plot) and spectral width (bottom plot) for beam 8, McMurodo radar on 07/22/2010. The black arrow shows the location of the target (range: 28) used for this case study.
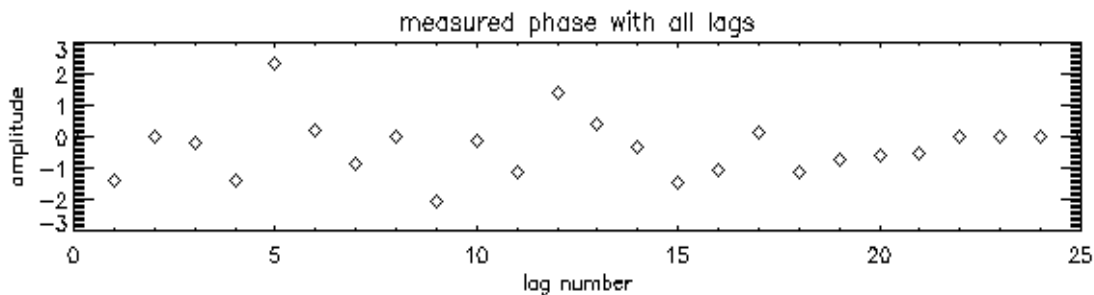
Figure 4.31: Measured phase profile with all lags for range 28, McMurdo radar, 4 UT, 07/22/2010.

Figure 4.31 shows the measured phase profile with all lags. Phase values in this figure and the power profile in RTI plot, suggests the target of interest is contaminated with cross-range interference. The proof is in the plots in Figure 4.32 where there are only five good lags left after removing bad lags. The measured slope of the line in the bottom plot of Figure 4.31 corresponds to Doppler frequency of -61.9 Hz.
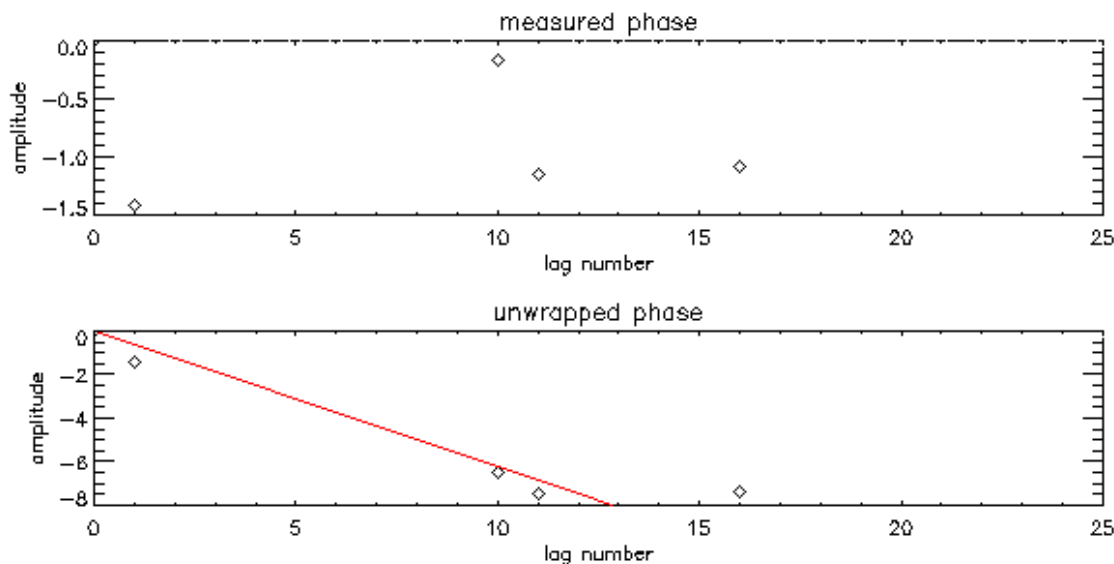
Figure 4.32: Measured and unwrapped phase profiles for range 28, McMurdo radar, 4 UT, 07/22/2010 using the FitACF algorithm.

While the calculated Doppler frequency in spectral analyses is approximately -123 Hz (Figure 4.33), the FitACF algorithm returns -61.97 Hz. In order to understand the discrepancy, 2 sets of power profiles with Doppler frequency of -123 Hz and -61.97 Hz were simulated, I-Q sampled, and phase profiles from ACFs were obtained. To quantify the difference between measured phase profile and simulated cases we obtain MSE (Mean Squared Error).
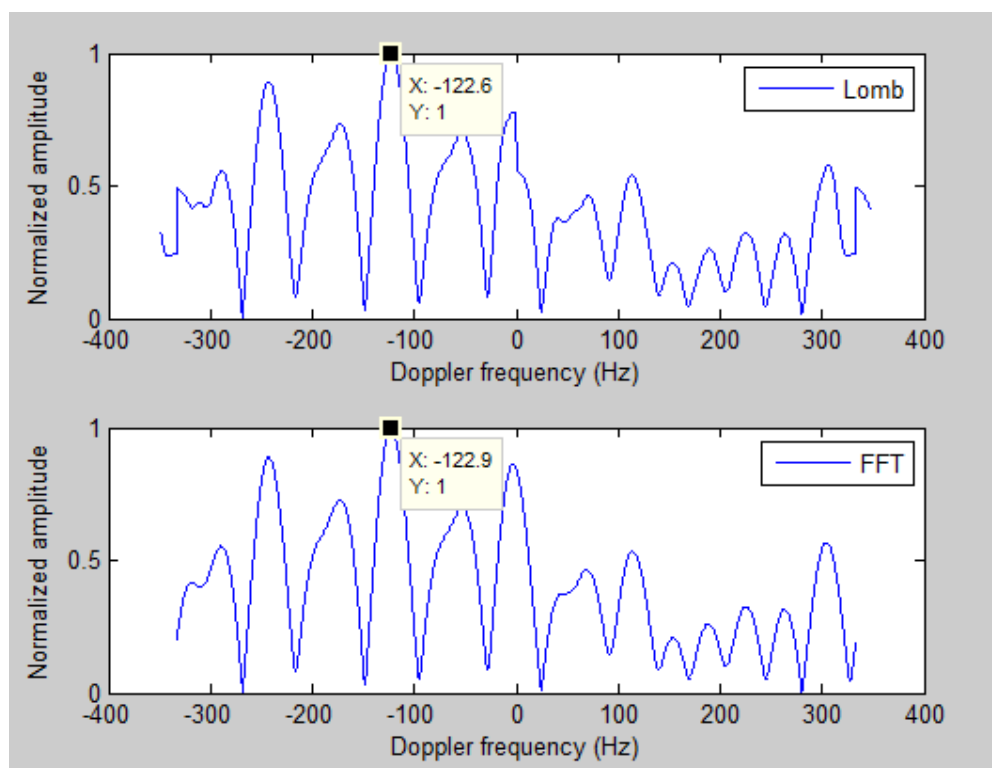
Figure 4.33: FFT and LOMB periodogram Doppler frequency measurement results for range 28,McMurdo radar, 4 UT, 07/22/2010.

Measured phase profile with all lags for observation made by McMurodo radar is shown in the first plot in Figure 4.34. The middle and bottom plots correspond to the simulated phase profile with -61.9 Hz and -122.7 Hz Doppler frequency. The MSE between the bottom and top plots with discarded bad lags is 0.032, while for the top and

middle plots equals 2.936. This shows larger bias for -61.9 Hz phase profile. In addition, Comparing the measured phase in three plots, the top and the bottom plot follow the same trend in terms of the slope and where the 2π jumps occur compared to the middle plot. Considering these factors, we prove that -122.7 Hz is the correct Doppler frequency for this profile. Thereby, the spectral analysis makes correct measurement of the Doppler frequency while the FitACF algorithm fails.
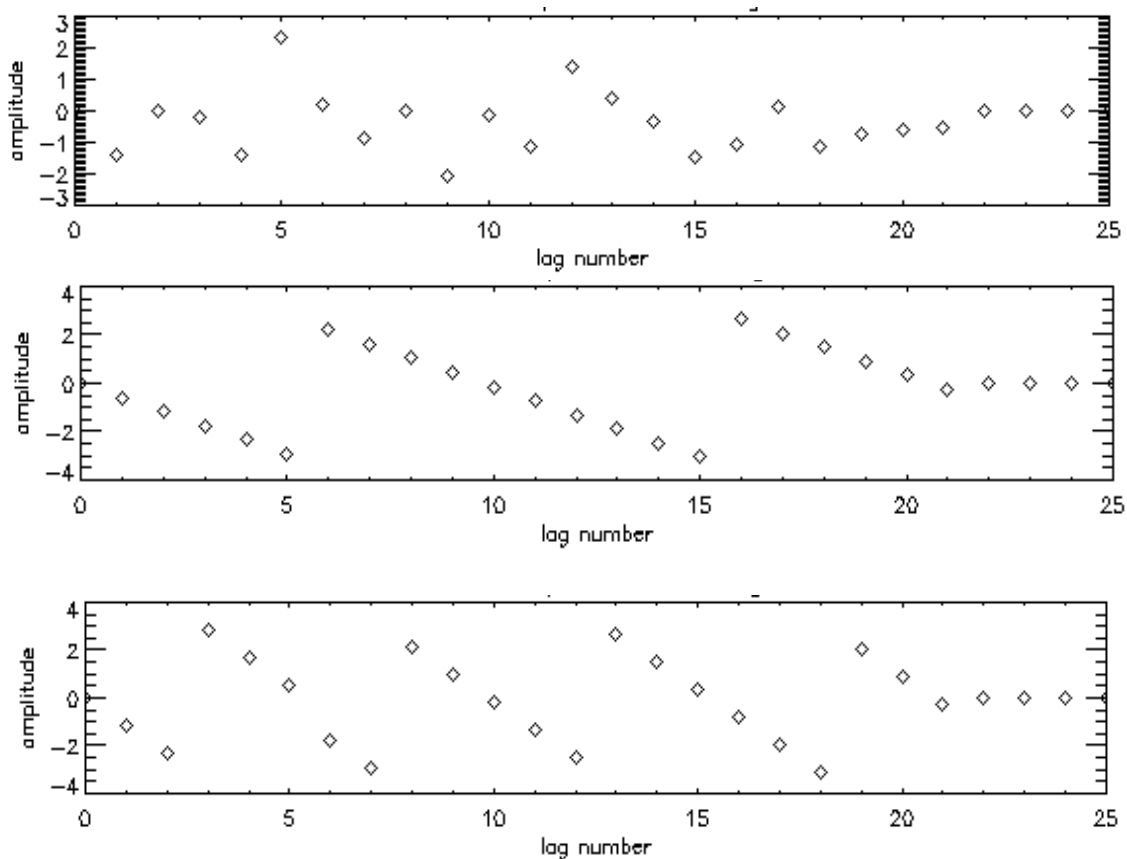
Figure 4.34: Top plot shows measured phase profile for range 28, McMurdo radar, 4 UT, 07/22/2010. The measured phase profiles for simulated moving targets with 61.97 Hz and -122.7 Hz Doppler frequency is shown in the middle and bottom plots.

The fundamental assumption behind the FitACF algorithm is that for each range gate, there is only one Doppler velocity to measure. In cases where there are two or more velocities in the range profile, the FitACF algorithm fails. Moreover, success of the phase unwrap algorithm depends on the number of remaining lags after discarding the TX-RX overlap and cross-range noise bad lags. Spectral analysis however, is less prone to cross-range noise and ensures to indicate existence of several moving targets by showing multiple peaks in the spectrum. It should be noted that the statistical confidence in the peaks deteriorates as the number of bad lags increase. There are cases where none of the methods is able to extracts the correct Doppler frequency. Nevertheless, combining spectral analysis with time domain analysis is one-step toward optimizing the algorithm. When there is a large discrepancy between the returned Doppler velocities using the two methods, the profile can be flagged and treated with more caution before using the profile to generate convection maps. For a sufficient number of lags in the lag profile, phase unwrap has superior performance with providing the desired resolution for the Doppler frequency of the profile, while for a lag profile with sparse distribution of lags, frequency domain analysis outperforms the time domain approach.

Chapter 5   SuperDARN Inverse Technique

Received signals scattered from plasma irregularities carry ambiguities due to the characteristics (overspread) of the SuperDARN target and their correlation time. This results in cross-range interference and consequently bad lags in the ACF profile. Contaminated lags are discarded in the FitACF algorithm, which can lead to a low number of data points for fitting process. As discussed in previous chapter, this returns erroneous results in extracting Doppler frequency, spectral width and fitted power. Cross-range noise is unavoidable but can be mitigated. It can be addressed by employing new pulse sequences along with pulse compression techniques on transmit side or new approaches on the receiver side. In this chapter, we study applicability of inverse methods on the SuperDARN received samples before they undergo ACF calculation.

5.1 Theory

Given model parameters and input, predicting an output is the general idea of obtaining a solution to a problem; this type of problem is called a forward problem. Inverse problem, on the other hand, attempts to have an estimation of the model parameters, when input and the approximate output (observed measurements) are available. Inverse problem techniques have applications in geophysics, seismology, image processing (tomography), life sciences, industry, etc. Here is an intuitive explanation for inverse theory (Sherlock Holmes):

> Most people, if you describe a train of events to them will tell you what the result will be. There are few people; however, if you told them a result, would be able to evolve from their own inner consciousness what the steps were that led to that result. This power is what I mean when I talk of reasoning backward.

The general form of a non-linear inverse problem is given in equation (5.1):

$$m = a(x).$$

<div align="right">(5.1)</div>

The non-linear inverse problem is defined as given the input (x) and the observed measurements (m), what the best likely model $(a(x))$ would be that maps the input to the measurements. While the nonlinear inverse problem is the generalized theory, the linear inverse problem, a simplified case of the nonlinear inverse problem, is shown in the following equation presented in terms of matrices:

$$m = Ax \qquad m \in R^{b \times 1} \qquad A \in R^{b \times n} \qquad x \in R^{n \times 1}, \qquad (5.2)$$

where b and n are dimension of the matrices. Depending on the dimensions of the matrix, the problem meets one of the following conditions:

- If $b > n$ the problem is overdetermined (more equations than unknowns) and has no exact solution. The solution can be reached only in a least-square sense.

- If $b < n$ the problem is underdetermined (more unknowns than equations) and has infinite solutions.

- If $b = n$ then the problem is well determined (equals number of equations and unknowns) and if A is not singular $(det(A) \neq 0)$ solving this equation yields a unique solution, which is given in (5.3):

$$x = A^{-1}m. \qquad (5.3)$$

The measurements in equation (5.2) are subject to errors and uncertainties that can be modeled as noise. The mathematical expression is given:

$$m = Ax + \varepsilon \qquad m \in R^{m \times 1} \quad A \in R^{m \times n} \qquad x \in R^{n \times 1} \quad \varepsilon \in R^{n \times 1}, \qquad (5.4)$$

where ε is the measurements error and is added as a matrix to equation (5.4). Solution to this equation is addressed using different approaches:

Least squares estimation: The idea is to find the best-fitted solution that minimizes the Euclidean norm ($\|\| \|$) of residuals ($arg\ min\ \|m - Ax\|^2$). The least square method does not utilize any priori information and statistical approaches to solve the problem.

The $arg\ min\ \|m - Ax\|^2$ term becomes the following equation in matrix representation (T means transpose):

$$x = (A^T A)^{-1} A^T m. \tag{5.5}$$

Maximum-likelihood estimation: In this case, the assumption for equation $m = Ax + e$ is that the given parameters (m and A) are known and fixed, while the noise is considered a random variable with known probability distribution. The likelihood function to achieve the optimal solution for x [13] is expressed in equation (5.6):

$$\pi(x\ |\ m) = C \cdot e^{\left\{\frac{-1}{2}(m-Ax)^T \Sigma^{-1}(m-AX)\right\}}, \tag{5.6}$$

where C is the normalization coefficient and Σ denotes the noise covariance matrix. The posteriori density is described as:

$$\pi(x\ |\ m) = C \cdot e^{\left\{\frac{-1}{2}(x-x_0)^T . Q.(x-x_0))+X^2\right\}}, \tag{5.7}$$

where $Q = (A^T \Sigma^{-1} A^T)$ is the fisher information matrix and x_0 and X^2 equal [13]:

$$x_0 = (A^T \Sigma^{-1} A)^{-1} A^T \Sigma^{-1} m,$$

$$X^2 = (m^T \Sigma^{-1} m - x_0{}^T Q\ x_0).$$

In this approach the exponential function gets its maximum value at $x = x_0$, thereby is considered the maximum value of the posteriori and the solution to the problem.

Maximum a Posteriori (Bayesian) estimation: Bayesian approach is based on statistical analysis and the assumption is if a priori information ($\overline{x_0}$) about x is known, equation (5.7) is modified as [13]:

$$\pi(x) = C_0 \cdot e^{\left\{\frac{-1}{2}(x-\overline{x_0})^T \Sigma_0^{-1}(x-\overline{x_0})\right\}}, \tag{5.8}$$

where Σ_0 is the prior covariance matrix of x. The solution in terms of matrices equals:

$$x_0 = (\Sigma_0^{-1} + A^T \Sigma^{-1} A)^{-1}(\Sigma_0^{-1}\overline{x_0} + A^T \Sigma^{-1} m). \tag{5.9}$$

5.2 Ill-posedness of Inverse Problems and Regularization

The measurement matrix in the inverse problem is contaminated with errors resulting from noise. This might lead to a non-invertible matrix and thereby no solution to the problem. This type of problem is considered ill conditioned and the solution is sensitive to small errors. That is, perturbations in measurements, even very small ones, result in large erroneous results for model parameters and noise (error) amplification. Steps should be taken to resolve this issue by replacing the ill-posed problem with a well-posed one. A well-posed problem has the following properties:

1) Solution for the problem exists.

2) The solution is unique.

3) The solution is stable. That is, it varies continuously with the input data of the problem.

A problem that is not well-posed is considered ill-posed. The least-square method might satisfy the first two conditions that yield a unique solution for the problem, but another step should be taken to address the third condition, which is stability. Regularization is one solution to tackle this problem by introducing additional information and remove instabilities.

5.2.1 Regularization

Since any measurement contains error, instead of the exact formulation in equation (5.2), we approximate the linear inverse problems as:

$$m \approx AX. \tag{5.10}$$

Equation (5.10) might satisfy the first two conditions of the well posedness, but errors in measurements lead to discontinuities. Regularization, the approach to remove discontinuities, is essentially passing the ill-conditioned matrix A through a filter, in which the filter coefficients are optimized to remove singular values that result in instability. This allows reaching a stable solution. Depending on the conditions of the problem, different methods of regularization such as, TSVD (Truncated Singular Value Decomposition), Kaczmarz's, Tikhonov, etc may be applicable. Smoothness of the data (mitigating singular values effects) in comparison with goodness of the fit (accuracy of the solution) is essentially the main difference between each method. Tikhonov regularization is the technique used to obtain model parameters and remove ambiguities from SuperDARN in-phase and quadrature samples in a least-squared sense.

5.2.1.1 Tikhonov Regularization

Solving equation (5.2) can be problematic, since the singular values of operator A tend to zero rapidly, leading norm of the approximation solution to go to infinity. Tikhonov regularization controls the norm of the residual and the norm of the approximate solution simultaneously [14]. This is done by introducing additional information called regularization parameter. The regularization parameter (δ) in Tikhonov regularization transforms the residual term ($arg\ min\ \|m - Ax\|^2$) to:

$$\arg \min (\|m - Ax\|^2 + \delta \|x\|^2),$$

which in terms of matrix representation equals:

$$x = (A^T A + \delta I)^{-1} A^T m. \hspace{2cm} (5.11)$$

Where I is the identity matrix. One can show the term in the parenthesis is always non-singular and has a unique solution. Although the penalty for achieving uniqueness is smoothness, in other words, overestimation or underestimation of the model parameters instead of the exact solution.

5.3 Simulation Results

In this section, use of inverse theory and Tikhonov regularization in removing cross-range interference from power profile of simulated cases are investigated. The difference between these two cases is how we formulate the problem and related matrices. We evaluate performance of each method in removing ambiguities and retrieving the cross section of the target at that particular range, as if it was not contaminated with cross-range noise.

5.3.1 Use of power profile in Estimating Target Cross Section (Case 1)

In this case, we use the SuperDARN standard pulse sequence for simulation. This information with target returns contaminated with cross-range interference is used to formulate our matrices in equation (5.10). Figure 5.1 shows the transmitted signal (blue) and the returned backscattered power (black) for simulated targets (ranges: 10-30). Two targets with Gaussian distribution in range and width of 10 ranges gates centered at ranges 15 and 25 were created. The received power for the second target is two times than that of the first target. The cross-range interference is observable in Figure 5.1, where simultaneous returns from different ranges contaminate with each other.
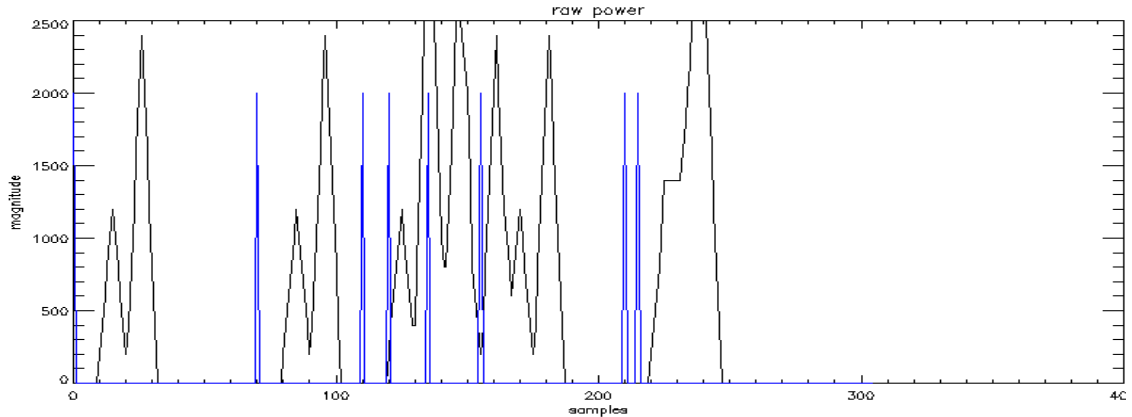
Figure 5.1: Simulated power profile for SuperDARN transmitted pulse sequence and received signal for two distributed targets with 30 Hz (range: 10-20) and 30 Hz (range:20-30) Doppler frequency.

For a general pulse sequence with the assumption of 75 range gates, up to 290 samples are recorded. These numbers are used to build the theory matrix (A). In contour plot of A in Figure 5.2, transmitted pulses in the pulse sequence define non-zero elements of the matrix and the dimensions ($A \in R^{75 \times 290}$) correspond to the total number of recorded samples and defined range gates. In Figure 5.2, 8 transmitted pulses in the pulse sequence are positioned in the first column of the matrix. As the transmitted signal travels over the defined range gates, the matrix elements move toward right. In this case, the assumption is that for each transmitted pulse in the pulse sequence the radar receives backscatter to the very last sample (290). The matrix representation of the problem is shown in equation (5.12). The elements of the measurement matrix are received power with noise; the theory matrix is composed of transmitted pulse sequence values and the model parameters matrix elements are target cross section in each range:

$$
\begin{bmatrix} m_1 \\ m_2 \\ m_3 \\ \vdots \\ m_{290} \end{bmatrix} = \begin{bmatrix} tx_1 & 0 & 0 & & 0 \\ 0 & tx_1 & 0 \cdots & & 0 \\ 0 & 0 & tx_1 & & 0 \\ \vdots & & \ddots & & \vdots \\ 0 & & \cdots & & tx_1 \end{bmatrix} \begin{bmatrix} x_1 \\ x_2 \\ x_3 \\ \vdots \\ x_{290} \end{bmatrix}. \tag{5.12}
$$
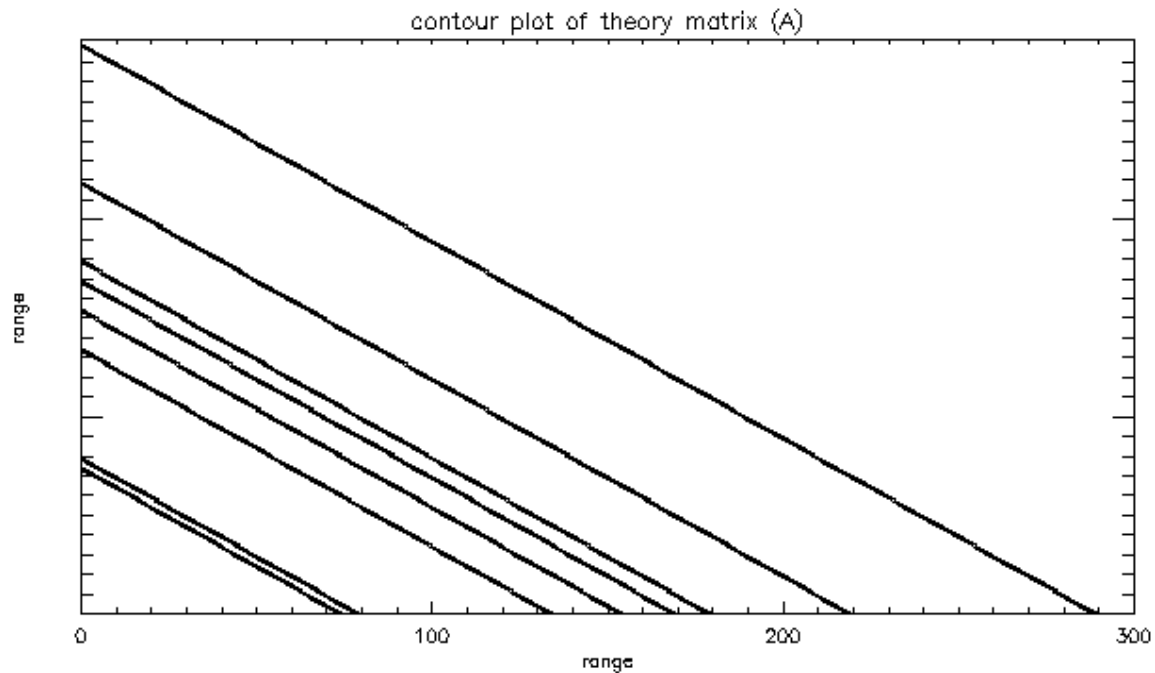
Figure 5.2: Contour plot of the theory matrix (A). The assumption is each pulse contributes to the received power from the sample number it is transmitted up to the very last sample.

5.3.1.1 Matrix Inversion:

The current inverse problem is well determined, thus the first approach is to simply obtain the inverse of the theory matrix (A) and multiply it by the measurements (m) to obtain cross section of the target at each range. Figure 5.3 shows the result of the multiplication of A^{-1} by itself. Since the result is not identity, the matrix is not inverted properly. Figure 5.4 shows the power profile calculated by multiply the theory matrix and the parameters model matrix derived by inversion. Noise has been amplified that suggests sensitivity of the problem to small perturbations. Thereby regularization is the appropriate approach to address this issue.
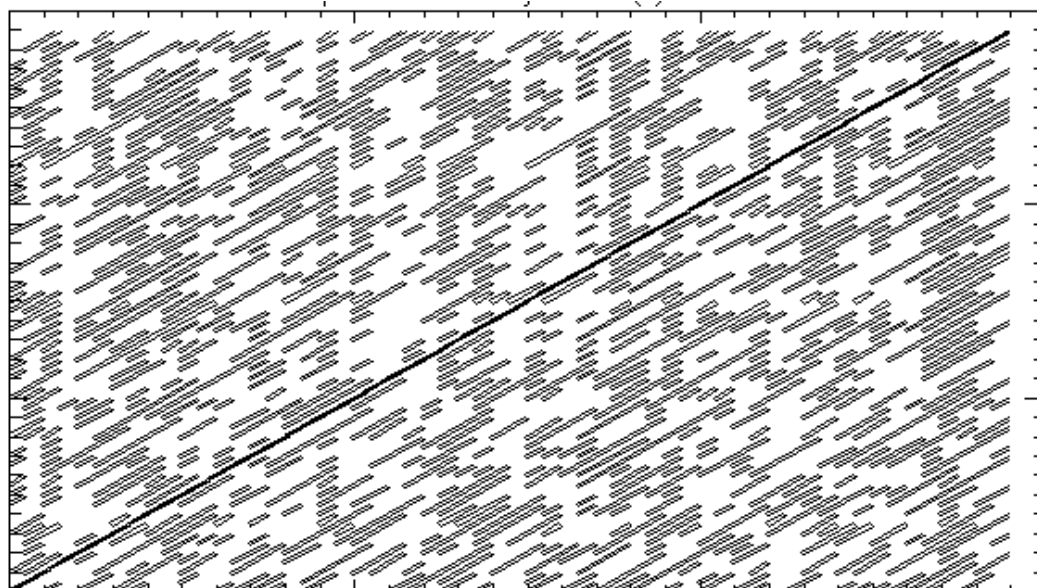
Figure 5.3: The contour plot of inverted theory matrix with itself is not identity and A is not inverted property.
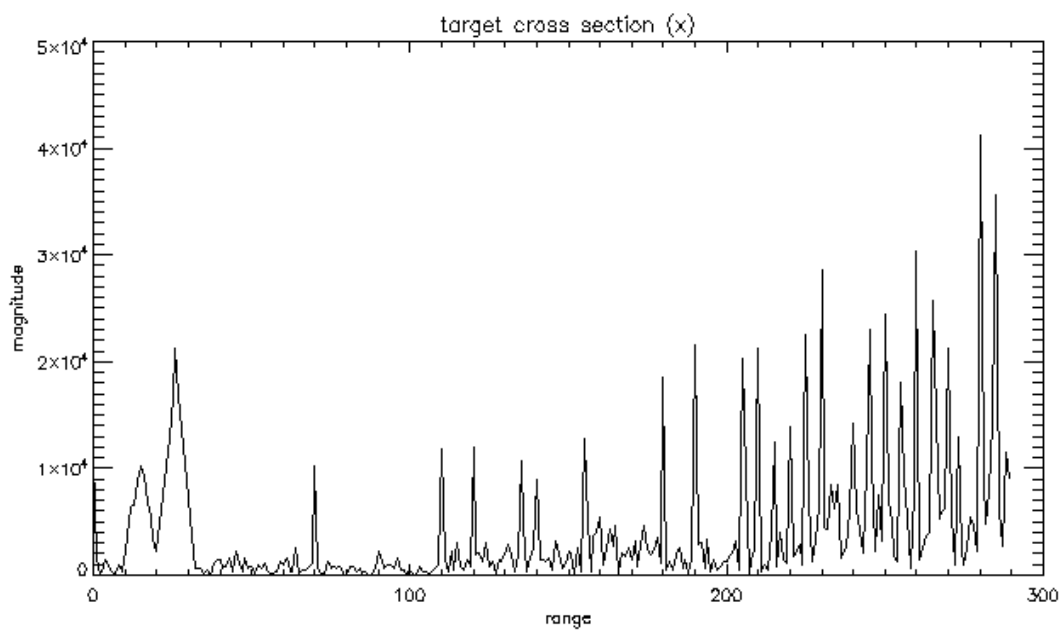
Figure 5.4: Inversion Result for simulated SuperDARN received backscatter. Sensitivity to perturbations results in noise amplification.

5.3.1.2 Tikhonov Regularization

In this case, two different values for the regularization parameter (δ) in equation (5.11) were chosen with the assumption that each pulse makes contribution to the received power from the sample number it is transmitted up to the last sample (290). In Figure 5.5 the result of multiplying $(A^T A + \delta I)^{-1}$ by itself is an identity matrix that proves proper inversion of the term inside the parenthesis in equation (5.11).
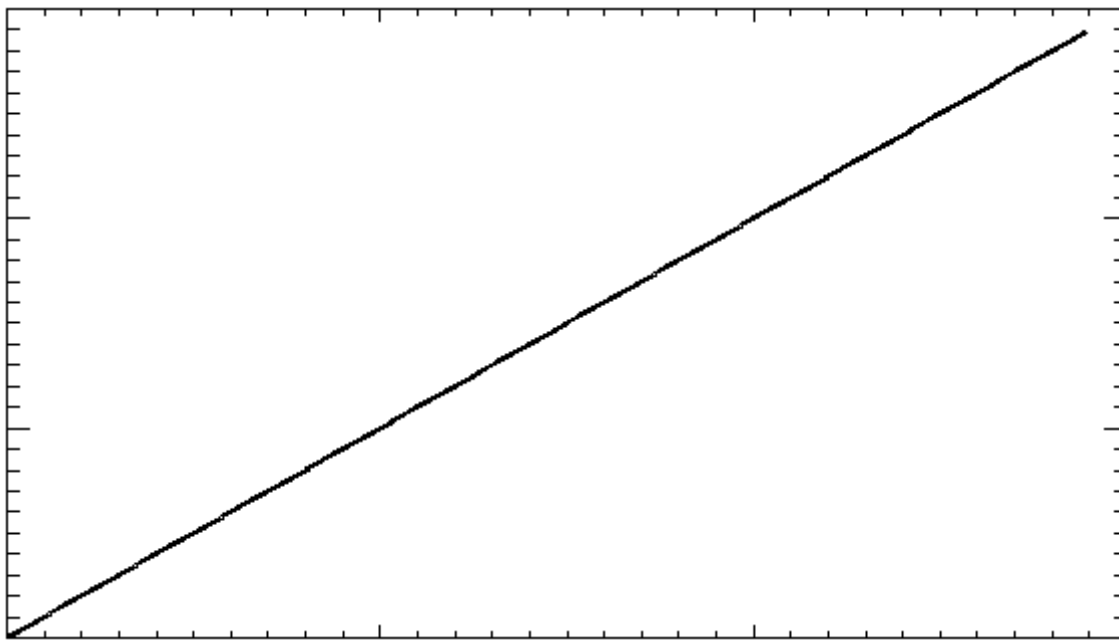
Figure 5.5: The contour plot of inversion part with itself yields identity matrix, which proves success in inverting $(A^T A + \delta I)$.

The inversion result for $\delta = 0.01$ and $\delta = 0.1$ is shown in Figures 5.6 and 5.7. Comparing the output results one can see the significance of the regularization parameter.
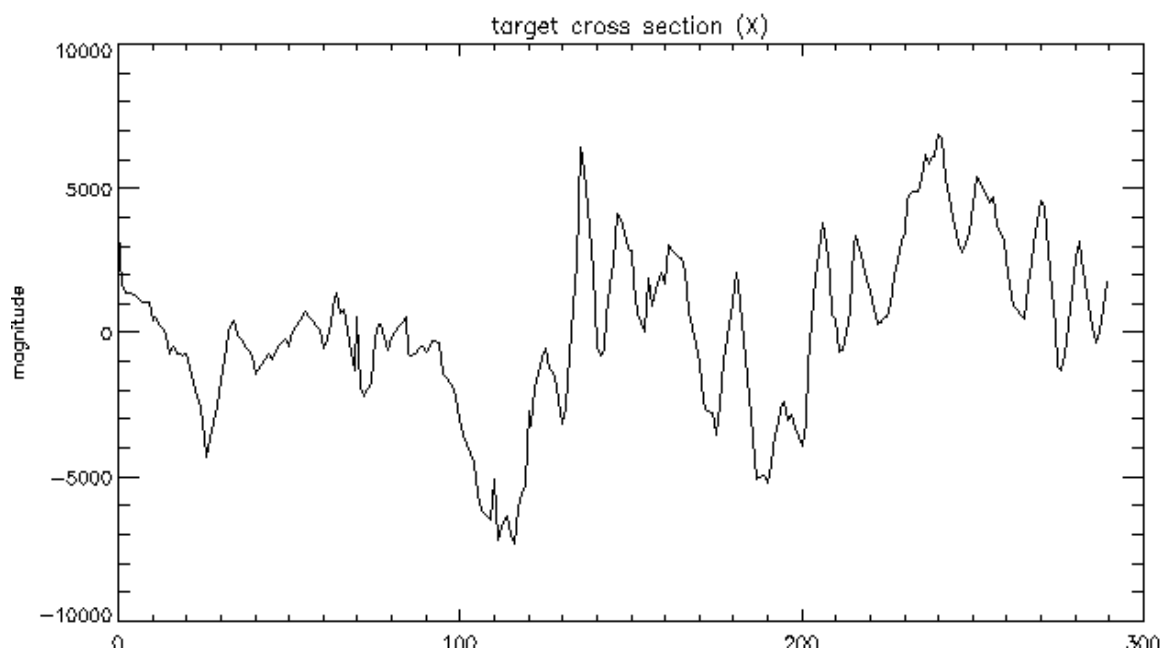
Figure 5.6: Result of the inversion using Tikhonov Regularization for simulated SuperDARN received backscatter with $\delta = 0.01$.
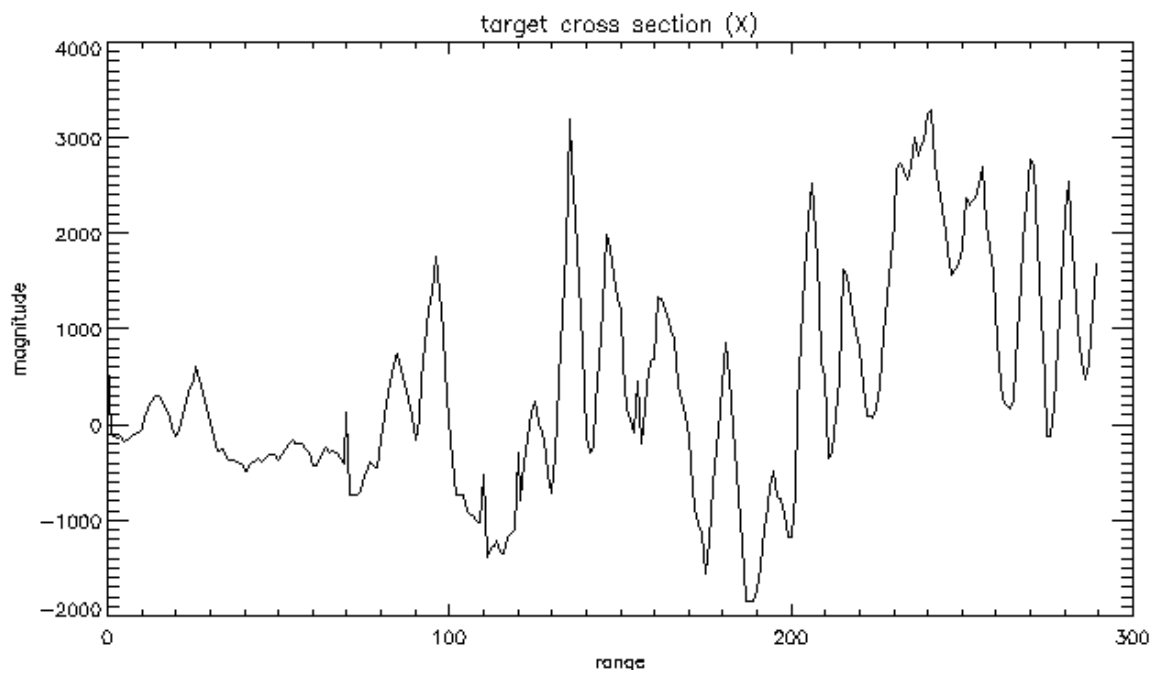
Figure 5.7: Result of the inversion using Tikhonov regularization for simulated SuperDARN received backscatter with $\delta = 0.1$.

Figures 5.6 and 5.7 show the inversion result for cross section profile of the targets. The profiles are not similar to simulated profile in Figure 5.1. Not even for the samples that are not contaminated by cross-range interference (samples: 0-75). It should be noted that the first 75 samples are free from contamination because the lag spacing (14τ) between the first and the second pulse in the pulse sequence. This gives radar enough time to sample returns for all defined range gates before transmitting the second pulse. The current approach does not show any success in retrieving the same profile for uncontaminated ranges and removing cross-range noise from the rest of the range profile as well.

5.3.2 Use of power profile in Estimating Target Cross Section (Case 2)

In this case, all the previous assumptions hold except that the radar records 75 samples for each transmitted pulse in contrast with 290 samples of previous case. This is shown in contour plot of the theory matrix in Figure 5.8. Matrix representation of the problem formulation is given in equation (5.14):

$$\begin{bmatrix} m_1 \\ m_2 \\ m_3 \\ \vdots \\ m_{290} \end{bmatrix} = \begin{bmatrix} tx_1 & 0 & 0 & & 0 \\ 0 & tx_1 & 0 \cdots & & 0 \\ 0 & 0 & tx_1 & & 0 \\ \vdots & & \ddots & & \vdots \\ 0 & & \cdots & & 0 \end{bmatrix} \begin{bmatrix} x_1 \\ x_2 \\ x_3 \\ \vdots \\ x_{290} \end{bmatrix}. \tag{5.14}$$
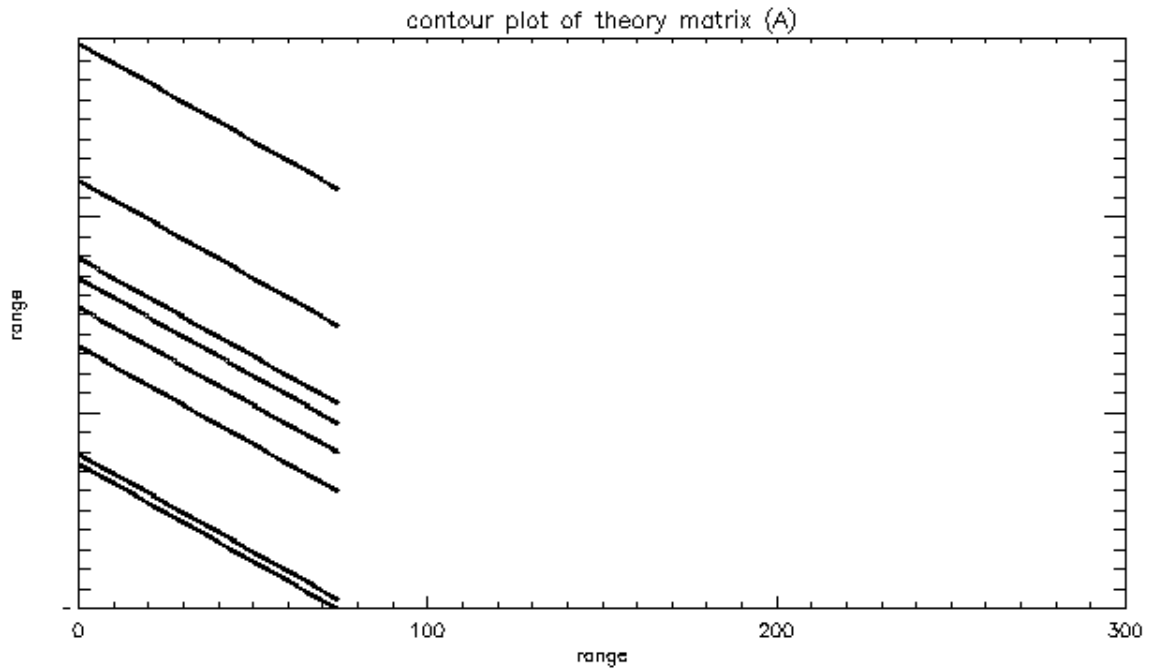
Figure 5.8: Contour plot of the theory matrix with 75 samples for each transmitted pulse in the pulse sequence.

5.3.2.1 Tikhonov Regularization

The inverse problem in this case is overdetermined and the solution is approachable only in a least square sense. We calculate power profile of the targets for this case using Tikhonov regularization given in equation (5.11). In this case, one value for the regularization parameter (δ=0.1) was chosen and the assumption is that for each transmitted pulse in the pulse sequence the radar receives 75 samples. Figure 5.9 shows the result of multiplying $(A^T A + \delta I)$ by its inverse to prove this part is inverted properly. The inversion result for $\delta = 0.1$ is shown in Figure 5.10.
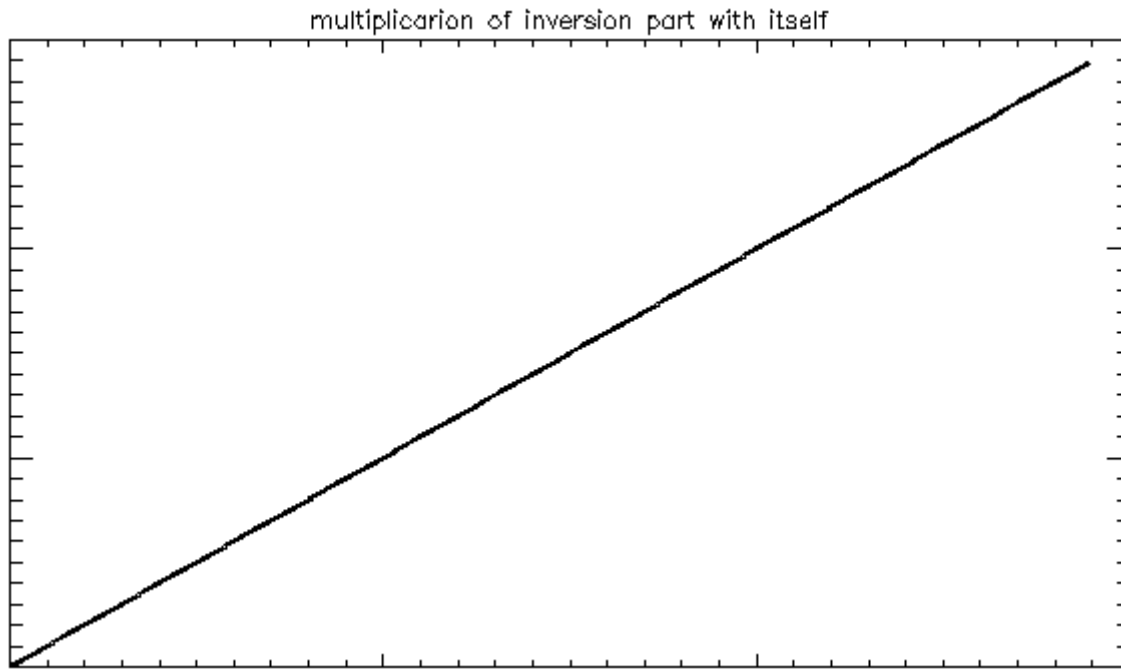
5.9: The contour plot of inversion part with itself shows success in inverting $(A^T A + \delta I)$

The result of inversion for the power profile in Figure 5.10 follows the same pattern in Figure 5.1. Figure 5.11 illustrates the normalized over plot of the inversion result on the measured power profile. This particular formulation for the problem shows success in removing cross-range interference from power profile and retrieving the same power profile for the first 75 samples.
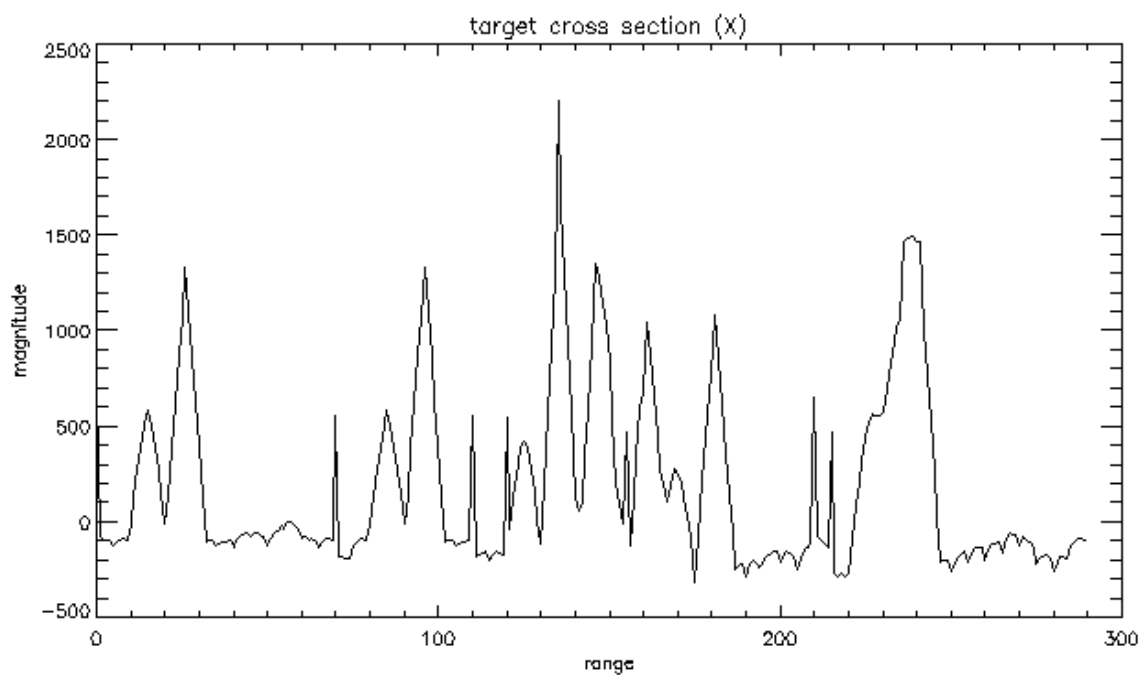
5.10: Result of the inversion using Tikhonov regularization ($\delta = 0.1$) for simulated SuperDARN received backscatter.
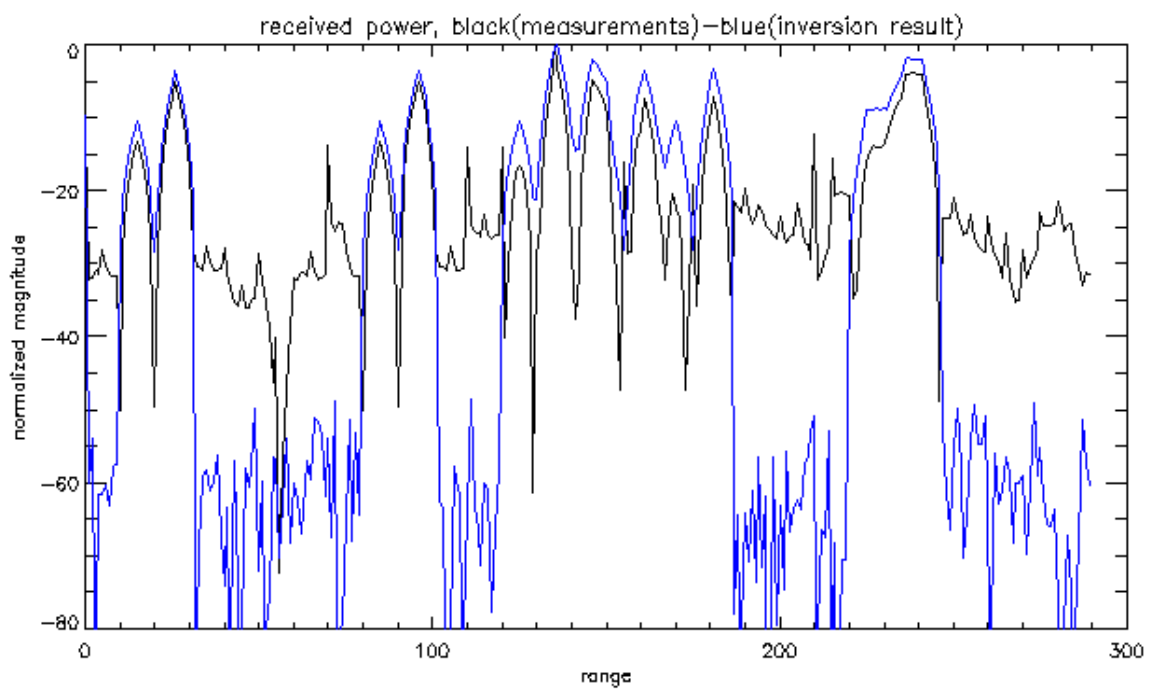
Figure 5.11: Normalized plots of the received power (black) and the inversion result (blue) with $\delta = 0.1$.

Cross-range interference affects the true values of the received power used to calculate ACF lag profile. In this chapter we tested capability of the least-squared base inversion technique in removing ambiguities from SuperDARN received power and producing the same profile for non-contaminated ones. Two different scenarios using power profile to formulate the inverse theory were studied. The inverse approach shows success in removing ambiguities from power profile of the ACF.

Chapter 6   Conclusions and Future Work

Although SuperDARN began as single radar in 1983, it has evolved to an international radar network with over 30 radars in high and mid latitude regions. The main objective of this network is to measure global-scale plasma convection maps and observe their changes over time as the geophysical conditions evolve. This thesis gave an overview of the SuperDARN algorithm that derives the Doppler velocity, spectral width, and fitted power from recorded ACF lag profiles along with new optimization techniques. These techniques include new filtering methods, spectral analysis, and use of inverse theory. The radar receives voltage samples and processes them to generate raw ACF profiles in real time. These profiles are saved and later employed by the FitACF algorithm to produce the fitted ACF parameters. Figure 6.1 shows the processing units involved in calculating these parameters from row voltages. This Figure shows to which part of the schematic each optimization method is applied. Inverse theory and filtering techniques are applied on raw samples before ACF calculation. While spectral analysis is applied in parallel with the post-processing unit to raw ACFs to calculate the fitted parameters.
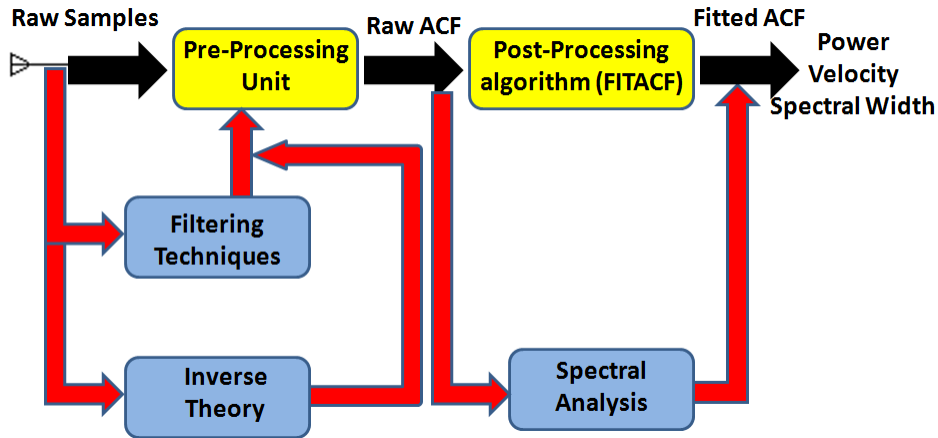
Figure 6.1: This outline shows the processing units (yellow boxes) involved in calculating the fitted ACF parameters from received raw samples. Blue boxes show the optimization approaches and to which processing unit they are applied.

The first chapter of the thesis introduced the radar principles. The ionosphere was described and the instruments involved in studying upper atmosphere were listed. Incoherent scatter radars that rely on Thompson scattering and coherent scatter radars, which are based on Bragg scattering mechanism to receive returns off the target, were discussed. SuperDARN, as coherent scatter radars, and the procedure of calculating the auto-correlation function from received voltage samples were presented. In chapter 2, we analyzed and gave the detailed descriptions of the SuperDARN FitACF algorithm; the algorithm that calculates power, spectral width, and Doppler velocity from ACF lag profiles using linear and non-linear fitting techniques. In addition, details of how the bad lags are calculated were given in this chapter.

Going through each subroutine the algorithm employs, along with use of an example, supplied the reader with enough information for the next chapters that were the focus of the research. Chapter 3 presented different methods of pulse compression techniques. Discussion of matched filtering, ambiguity function and different types of coding schemes were part of this chapter. Following this, mismatched filtering was introduced; the technique that can be replaced by matched filtering to mitigate effects of

the side lobes. Adaptive filtering, a compromise between matched and mismatched filtering, was studied in this chapter. Offering optimum SNR of the main lobe achieved in matched filtering and sidelobe suppression capability of the mismatched filtering is what makes the adaptive filtering superior. However, the computational cost of adaptive filtering, is considered the disadvantage. This can be addressed by using dimensionality reduction techniques. Moreover, depending on the range resolution, the matrices described in adaptive filtering can grow in size. Other techniques such as, iterative methods can be employed to invert these large size matrices efficiently. Although being computationally expensive is the down side, performance of this method makes it a perfect approach for a campaign where special cases are studied. Currently the Barker code is the standard pulse compression technique for normal operation in Kodiak and McMurdo radars. Other techniques such as frequency coding, pseudo random code generators are potential alternatives, however, the hardware limitations should be considered as well. Chapter 4 described the spectral analysis in comparison with currently used time domain analysis. Fourier transform as the standard approach for spectral analysis and the Lomb Periodogram for cases dealing with unequally sampled data were investigated. Albeit the spectral analysis does not provide the time domain resolution in measuring the Doppler velocity, robustness and versatility of the spectral analysis in measuring multiple Doppler frequencies in the range profile is advantageous. The next step can be investigation on the other least- square spectral methods that suffer less from windowing effect. Moreover, in time domain analysis, there are other approaches for phase unwrap such as, complex Cepstrum (Z-transform based) and Tribolet method that can be considered as other choices. Chapter 5 investigated the applicability of the inverse theory to the SuperDARN received samples. The inverse technique shows success in removing range ambiguities from power profile of the received signal. Since the full complex signal is required for calculating velocity, this approach can be applied to in-phase and qudarature samples of the received signal that provide phase information.

Despite being fast and providing good accuracy in deriving the fitted parameters, the FitACF algorithm becomes erroneous when an adequate number of good lags are not available in the range profile. As discussed in the second chapter, there are thresholds in the FitACF algorithm that decide if the lag should be passed to the next stage for further processing or not. These thresholds are set numerically and more investigation to determine the optimum threshold that would make maximum use of the information the lags carry is of importance for optimization. In addition, the current algorithm removes a range profile from further processing if there are less than five good lags in the ACF. Based on analysis of the power profile, the algorithm decides which lags due to cross-range interference should be marked as bad lags and removed. However, velocity and power are two independent variables. The lags marked as bad and discarded because of bad power profile might have some useful Doppler velocity information that can be used for phase unwrapping purposes. In addition to the number of good lags in the lag profile, the distribution of these lags is another important factor. For instance, five consecutive good lags, increase the probability of measuring the correct Doppler velocity of the phase profile, while the same number of lags with sparse distribution locating at different lag numbers might result in erroneous calculation of the Doppler velocity. In addition to techniques that mitigate the effects of cross-range interference, other approaches such as, new pulse sequences, changing the polarization of the antenna for pulses within the pulse sequence are other alternatives to avoid this type of noise to some extent.

Appendix A

Quality Flag (qflg) determination for FitACF algorithm.

Before passing the calculated parameters to the last routine (FitACFFitACF) for obtaining the fitted power and spectral width, the code marks each range profile with three numbers: 1, 2 and 4 as quality flags. The quality flags let the code determine whether there are enough good lags in ACF lag profile in each range to do the non-linear fitting techniques or not. The value of the quality flag is described as:

qflg $= 1$: This number shows that there are at least 5 lags left in the range profile after removing lags due to bad power. If qflg=1 then the algorithm carries out the fitting process otherwise the code assumes $p\_l = p\_s = pwr[0]$ and skips this step. The code assumes a good lag as bad power if:

$$w < noise\_lev, \tag{A.1}$$

where, $noise\_lev = ave\_noise\_pwr =$, and w is given in equation (A.2):

$$w = \text{abs}(ACF) - noise_{lev} - p0n, \tag{A.2}$$

where $p0n = \frac{w[0]}{\sqrt{nave}}$.

In each lag, if the lag is not a bad lag and $w < noise\_lev$ then the code marks this lag as bad power.

qflg $= 4$: This value shows that in the ACF lag profile for that range, there were not minimum number of good lags, thereby fitting cannot go further and all the non-linear fitting parameters are set to zero. The minimum number of required lags in the current FitACF algorithm is 5.

qflg $= 2$: It shows that for that range either, abs$(acf(0)) < noise\_lev\_in$ or abs$(acf[0]) - noise\_lev - p0n < noise\_lev$. In any of these cases, if number of good lags is more than 5 then the conditions for qflg $= 1$ are imposed. In case of success, the algorithm replaces the qflg of 2 with 1.
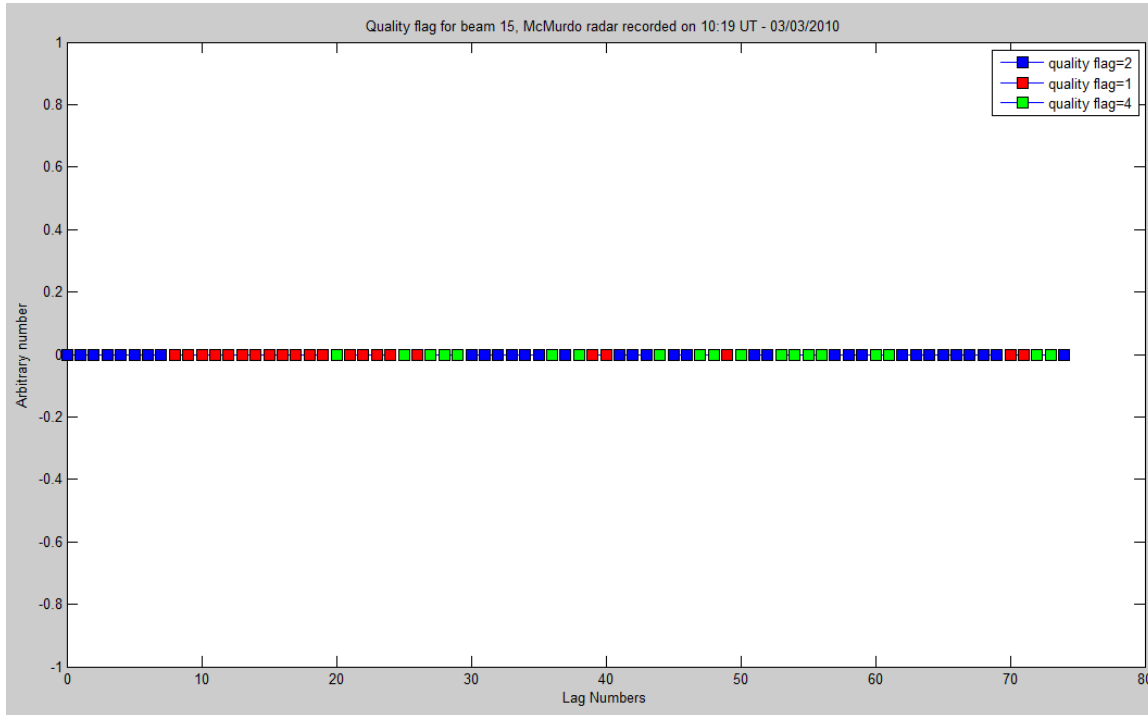

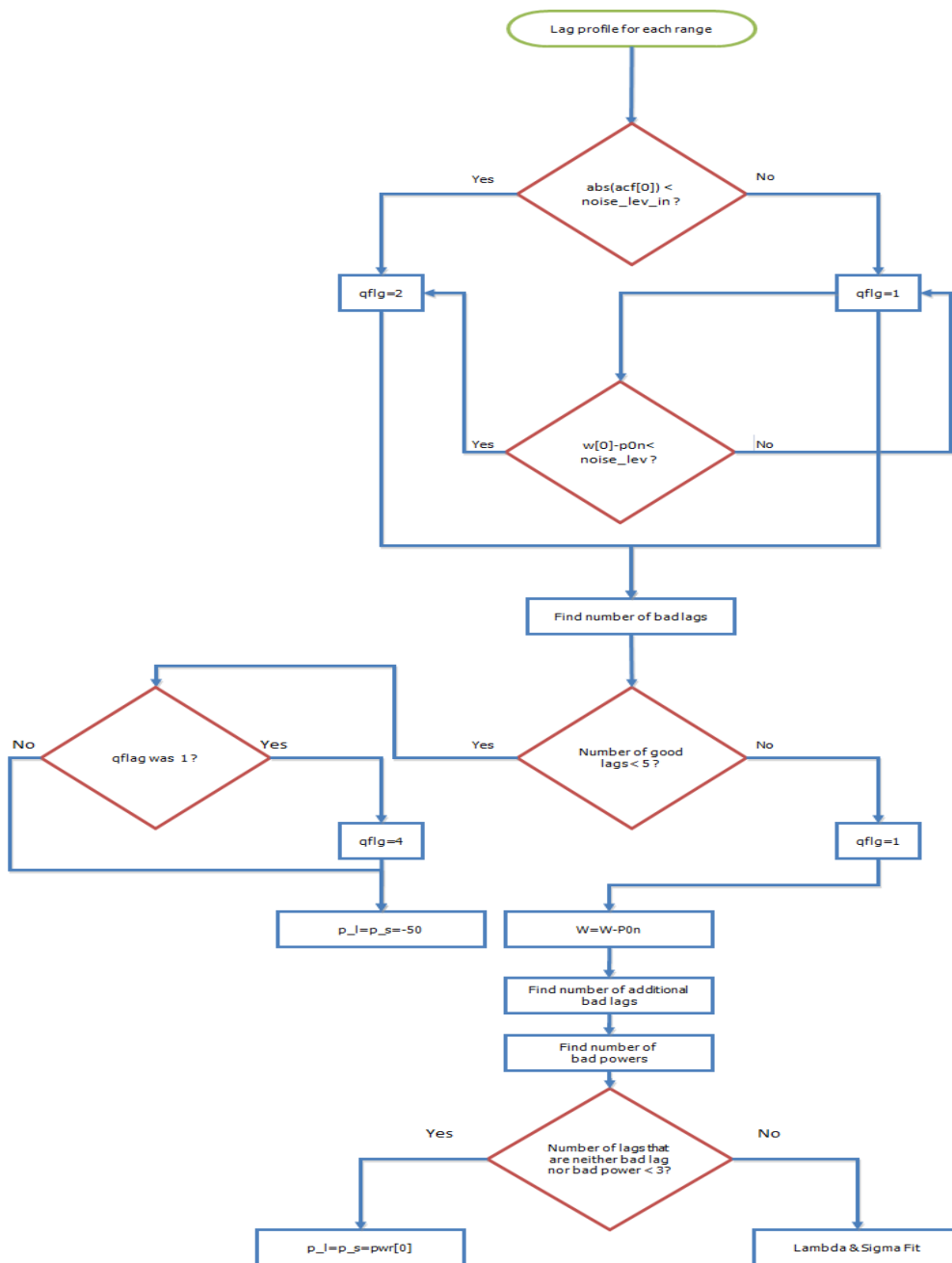Figure A.1: Quality flag illustration for beam 15, McMurdo radar

Figure A.2: Flow chart presenting quality flag allocation.

Least Squares Fitting

For n data points, (x_i, y_i) $i = 1, 2, \ldots, n$, to which we wish to fit some model *f(x)* in a least-square fashion, we calculate the minimum of residuals *(ri = yi − f(xi))* given in equation (A.3):

$$Minimum\ least\ squared\ value = \sum_{i=1}^{n} r_i^2. \tag{A.3}$$

Equation (A.3) shows where MLSV becomes minimum, the best linear parameters for fitting are chosen. By solving equations (A.4) and (A.5) for n data points, least square linear fitting parameters (a and b) can be calculated for the fitted line $(y = bx + a)$ to the data points where b represents the slope of the line and a denotes y intercept [15]:

$$\sum_{i=1}^{n} y_i = na + b \sum_{i=1}^{n} x_i, \tag{A.4}$$

$$\sum_{i=1}^{n} x_i y_i = a \sum_{i=1}^{n} x_i + b \sum_{i=1}^{n} x_i^2. \tag{A.5}$$

The matrix representation of the above equations are given as:

$$s = \sum_{i=1}^{n} \frac{1}{\sigma_i^2}, \qquad\qquad S_x = \sum_{i=1}^{n} \frac{x_i}{\sigma_i^2},$$

$$S_y = \sum_{i=1}^{n} \frac{y_i}{\sigma_i^2}, \qquad S_{xx} = \sum_{i=1}^{n} \frac{x_i^2}{\sigma_i^2}, \qquad S_{xy} = \sum_{i=1}^{n} \frac{x_i y_i}{\sigma_i^2}.$$

Here σ_i is the standard deviation for each point (x_i, y_i) and the parameters of the fitted line are shown in equations (A.6) and (A.7):

$$a = \frac{S_{xx} S_y - S_x S_{xy}}{s S_y - (S_x)^2}, \tag{A.6}$$

$$b = \frac{S S_{xy} - S_x S_y}{s S_y - (S_x)^2}. \tag{A.7}$$

For any number of points the non-linear fitting in addition to linear fitting can be applied. For exponential (Lambda) fitting technique the equation is given:

$$y = ae^{bx}. \tag{A.8}$$

There are different method to find the best values of the design parameters (a,b) of lambda fitting. The most straight forward method is to take logarithm of each side and solve equations (A.4) and (A.5) for the resultant linear term to find the best possible values of the exponential curve. The procedure is shown below:

$$y = ae^{bx},$$

$$\log(y) = \log(ae^{bx}),$$

$$\log(y) = \log(a) + bx \cdot \log(e). \tag{A.9}$$

Where, $\log(y) = y, \log(a) = A \ and \ b.\log(e) = C$, hence results in:

$$y = A + Cx. \tag{A.10}$$

Equation (A.10) is the linear form of the non-linear curve.

Bibliography

[1] Skolnik, M. I., Introduction to RADAR systems, Ed. New York: McGraw-Hill, 1962.

[2] Beynon, W. J. G., and P. J. S. Williams, Incoherent scatter of radio waves from the ionosphere, Rep. Prog. Phys, 1978.

[3] Alcaydé, D., Incoherent Scatter Theory, Practice and Science, Collection of lectures given in Cargese, Corsica, 1995.

[4] Greenwald, R. A., and et al, A Global View of the Dynamics of High-Lattitude Convection, Space Science Reviews, Volume 71, Issue 1-4, pp. 761-796, 1995.

[5] Bryson, G., W. A. Bristow, An Introduction to Radar and the Super Dual Auroral Radar Network.

[6] Chisham, G., M. Lester, S. E. Milan, M. P. Freeman and W. A. Bristow, Surveys in Geophysics, Volume 28, Number 1, Pages 33-109, 2007.

[7] Farley, D. T., Multi-pulse incoherent scatter correlation function measurements, 1972, Radio Sci., 7, 661–666.

[8] Cookm, C., The Early History of Pulse Compress ion Radar, IEEE Transactions on Aerospace and Electronic Systems Vol. 24, No. 6 November 1988.

[9] Richards, M. A., and et al, Principles of Modern RADAR, Ed: North Carolina, Scitech, 2010.

[10] Lehtinen, M. S., and et al, Optimal binary phase codes and sidelobe-free decoding filters with application to incoherent scatter radar. Annales Geophysicae (2004) 22: 1623–1632.

[11] Geralch, K., and S. D. Blunt, Adaptive pulse compression via MMSE estimation. IEEE Transactions on Aerospace and Electronic Systems, Vol. 42, No. 2 APRIL 2006.

[12] Oh, J., and T. K. Sarkar, Spectral analysis of nonuniformly sampled data using a least square method for application in multiple PRF system, Phased Array Systems and Technology, 2000 IEEE International Conference, pp.141-144, 2000.

134

[13] Virtanen, I. I., M. S. Lehtinen, and T. Nygren, Lag profile inversion method for EISCAT data analysis, Ann. Geophys., 26, 571–581, 2008.

[14] Kaipio, J., and E. Somersalo, Statistical and Computational Inverse Problems, Springer Publications, 2004.

[15] Hashemiparast, M., Probability and Statistics in Engineering and Science, KN University Publications, 1997.